

Investigations on Multifarious Shape Memory Alloy (SMA) Structures towards the Development of Bio-Inspired Soft Robots

Ph.D. Thesis

By
M. MURALIDHARAN



**DISCIPLINE OF MECHANICAL ENGINEERING
INDIAN INSTITUTE OF TECHNOLOGY
INDORE
AUGUST, 2020**

Investigations on Multifarious Shape Memory Alloy (SMA) Structures towards the Development of Bio-Inspired Soft Robots

A THESIS

Submitted in partial fulfillment of the requirements for the award of the degree

of

DOCTOR OF PHILOSOPHY

by

M. MURALIDHARAN



**DISCIPLINE OF MECHANICAL ENGINEERING
INDIAN INSTITUTE OF TECHNOLOGY**

INDORE

AUGUST, 2020



INDIAN INSTITUTE OF TECHNOLOGY INDORE

CANDIDATE'S DECLARATION

I hereby certify that the work which is being presented in the thesis entitled **Investigations on Multifarious Shape Memory Alloy (SMA) Structures towards the Development of Bio-Inspired Soft Robots** in the partial fulfillment of the requirements for the award of the degree of **DOCTOR OF PHILOSOPHY** and submitted in the **Discipline of Mechanical Engineering, Indian Institute of Technology Indore**, is an authentic record of my own work carried out during the time period from **JULY 2016** to **AUGUST 2020** under the supervision of **Dr. I. A. Palani**, Associate Professor, IIT Indore.

The matter presented in this thesis has not been submitted by me for the award of any other degree of this or any other institute.

Signature of the student with date

This is to certify that the above statement made by the candidate is correct to the best of my/our knowledge.

31-08-2020

Signature of Thesis Supervisor with date

M. Muralidharan has successfully given his/her Ph.D. Oral Examination held on 20-01-2021

Signature of Chairperson (OEB)

Date: 20/1/2021

Signature of External Examiner

Date: 20/1/2021

Signature of Thesis Supervisor

Date: 20/1/2021

Signature of PSPC Member #1

Date: 20.01.2021

Signature of PSPC Member #2

Date: 20/01/2021

Signature of Convener, DPGC

Date: 20.01.2021

Signature of Head of Discipline

Date: 20.01.2021

ACKNOWLEDGEMENTS

I am grateful to my thesis supervisor **Dr. I. A. Palani** for his eminent guidance and support throughout the Ph.D. program. He has constantly motivated and aided me with necessary facilities to successfully complete the work in stipulated tenure. His consistent discussions have yielded fruitful suggestions and ideas to carry out the thesis work in a comprehensive way.

I would like to thank **Prof. Neelesh Kumar Jain**, Director, IIT Indore, and **Dr. Santosh K. Sahu**, Head of the department, Mechanical Engineering for the opportunity and support to conduct my research. I thank the PSPC members **Dr. Trapti Jain and Dr. Shailesh Kundalwal** for their valuable suggestions. I am thankful to DPGC convener **Dr. Pavan Kumar Kankar** for the support and suggestions. I am thankful to **Dr. Devendra Deshmukh** and **Dr. M. Anbarasu** for their moral support.

I convey my sincere thanks to the **Ministry of Human Resource and Development (MHRD)**, India for the teaching assistantship from July 2016 to August 2020.

I would like to thank all the members of OMG for their affection and support. I am thankful to my research colleagues **Dr. K. Akash, Dr. S. S. Maniprabu, Mr. S Jayachandran, Mr. M Manikandan, Mr. Sarathkumar** for their constant support.

I am thankful to **Mr. Shreyash singh, Mr. A. Brolin, Mr. R. Mithun, Ms. K. Aishwarya, Mr. Vinay kumar rapaka, Mr. Parvesh saini, and Mr. Preshit ameta**

I am thankful to **Mr. Ashwin Wagh** and **Mr. Krishna Tomar** of the OMG group for their support.

I am thankful and indebted to my parents, grandparents, in-laws, brother, and his family for their love and constant support. I am thankful to my wife Sofia, my daughter Janani and my son Yuvan for their unconditional love and support throughout my Ph.D. career.

Dedicated to My Family

PREFACE

Conventional robots and machines are made of rigid materials that limit their ability to elastically deform and adapt their shape to external constraints and obstacles. Soft robotics is an emerging topic in the field of robotics which challenges the traditional engineering thinking. It utilizes soft materials and actuator technologies similar to natural creatures to mimic its functionality. Among smart materials, shape memory alloy (SMA) based actuators are able to generate large displacements with simple mechanisms. SMAs are available in various geometrical forms such as spring, wire, and bimorph which can be suitably coupled or employed with soft materials to develop bioinspired robots. The thesis work aims to employ the different forms of SMA structures like spring, wire embedded soft composite and bimorph towards the development of soft robots. The feasibility of SMA-based structure in the development of bio-inspired soft robots has been investigated.

Using SMA based actuator technology, SMA spring actuated soft meshworm, SMA spring based propulsion for robotic fish, SMA bimorph based soft robot for micro positioning applications, SMA wire embedded composite based soft robotic gripper and SMA wire/polyimide based soft jellyfish robot has been developed. A detailed investigation to evaluate the bending characteristics of meshworm has been carried out. The subcarangiform fish has been mimicked with the proposed SMA spring based design and its locomotion has been investigated in water channels. SMA bimorph based soft robot has been developed and its actuation and control behavior has been investigated. A SMA wire embedded polydimethylsiloxane (PDMS) soft actuator has been developed. The actuation and life cycle behavior of the soft actuator has been studied. A soft robotic gripper was developed using soft composites and its functionality has been demonstrated. A SMA wire/polyimide based soft robotic jellyfish has been developed and its locomotion has been investigated.

LIST OF PUBLICATIONS

International Journals

1. **Muralidharan M**, Aishwarya K, Mithun R, Palani I A, *Thermo-mechanical behaviour of SMA wire embedded PDMS actuator towards soft robotics applications*, **International Journal of Robotics and Automation**, Vol. 35, 2020. (IF-0.854)
2. **Muralidharan M**, Brodin A, Mithun R, Rohit Patil, I.A.Palani, *Investigations on Bending Characteristics of Soft Mesh Structure using Shape Memory Alloy Spring Towards Bio-Inspired Robotic Applications*, **Iran J Sci Technol Trans Mech Eng**, 2020. (IF-1.029)
3. **Muralidharan M**, Jayachandran S, Yogeshwaran M, Shivaani A S, Palani I A, *Investigations on the Thermo Mechanical and Control Behavior of Copper Based SMA Bimorph Actuator towards the Development of 3 DOF Micro Positioning System*, **Defence Science Journal**, Vol.70, No 6, 664-671, 2020. (IF-0.730)
4. S. S. Mani Prabu, Mithun R, **M. Muralidharan**, Tameshwer Nath, Brodin A, K. Akash, I.A.Palani, “Thermo-mechanical behavior of shape memory alloy spring actuated using novel scanning technique powered by ytterbium doped continuous fiber laser”, **Smart Materials and Structures** 28, 047001, 2019. (IF-3.613)
5. **Muralidharan M**, Palani I A, *Development of Subcarangiform Bionic Robotic Fish Propelled by Shape Memory Alloy Actuators*, **Defence Science Journal**, **Vol 71 No 1**, 2020. (IF-0.730)
6. **Muralidharan M**, Palani I A, *Bio-inspired Soft Jellyfish Robot: a novel polyimide based structure actuated by Shape Memory Alloy*, **Advanced Robotics**, 2020 (Under Review). (IF-1.249)

Conferences

1. **Muralidharan M**, Maniprabu S.S and Palani I A, *Design and Development of SMA based bio-inspired jellyfish*, **Institute of Smart Structures and Systems (ISSS), ISSS – IISc (ECE) Researchers’ Forum**, Bangalore, India, 26th -27th April 2019.
2. **Muralidharan M**, Brolin A, Mithun R, Rajagopalan P, Sachin Bhirodkar and Palani I A, *Actuation Study on Shape Memory Alloy Wire Embedded Polydimethylsiloxane for Soft Robotic Applications*, Institute of Smart Structures and Systems (ISSS), **National Conference on SMART MEMS, Smart Materials, Structures & Systems (ISSS, IISc Bangalore)**, TCE Madurai, 2018.
3. **M. Muralidharan**, A. Brolin, B. Mayank, P. G. Naveen, S. Jayachandran, B. Sachin, I. A. Palani, *Design and Development of Polydimethylsiloxane (PDMS)/ Shape memory alloy (SMA) Integrated Bimorph for Soft Robotic Applications*, **Recent Innovation In Advanced Materials (RIAM) , Advanced Materials and Processes Research Institute(AMPRI), Council of Scientific & Industrial Research(CSIR) Bhopal**, India, 2018.
4. **Muralidharan M**, Brolin A, Mayank B, Naveen P, Mithun R, Suhel K, Rajagopalan P and Palani I A, *Design and Development of Polydimethylsiloxane (PDMS) Based Smart Flexible Soft Robotic Actuator Driven by Shape Memory Alloy Wire*, **International Conference on Advancements in Automation, Robotics and Sensing (ICAARS) 2018**, PSG College of Technology, Coimbatore, India.
5. **Muralidharan M**, Aishwarya K, Mithun R, Palani I A, *Thermo-mechanical behaviour and life cycle analysis of SMA wire embedded PDMS actuator towards soft robotics applications*, **International Conference on Robotics Automation and Non Destructive Evaluation (RANE 2019)**, Hindustan Institute of Technology and Science, Chennai.

TABLE OF CONTENTS

	Page No
LIST OF FIGURES	XVI
LIST OF TABLES	XXIII
NOMENCLATURE	XXIV
ACRONYMS	XXV
1 Introduction to Bio-inspired soft robotics and shape memory alloys	
1.1 Bio-inspired Soft Robotics	1
1.2 Shape memory alloy	3
1.3 Applicability of different geometrical forms of SMA in soft robotics	8
1.4 Application of SMA in bioinspired robotics	13
1.5 Motivation of the study	14
1.6 Overall objectives of the thesis	15
1.7 Outline of the thesis	16
2 Overview on the smart material based bio-inspired soft robotics	
2.1 Smart materials based inchworm robots	17
2.1.1 SMA wire based composite structures	17
2.1.2 SMA spring based structures	20
2.2 Smart materials based jellyfish robots	21
2.3 Smart materials based fish robots	28
2.4 Smart materials based thin film robots	34
2.5 Inference and research gap from the literature-Summary	38
2.6 Detailed objectives and methodology	39
3 Investigations on SMA spring based actuators towards bio-inspired soft meshworm	
3.1 Introduction	42
3.2 Bio-inspired softworm robot	42
3.3 Modeling of SMA spring	43
3.4 Inchworm Mechanism	46
3.5 Fabrication of softworm skeletal structure	48

3.6 Experimental Setup	50
3.7 Performance Evaluation	51
3.7.1 Peristaltic crawling	51
3.7.2 Two anchor crawling	53
3.8 Non-Contact actuation of Soft Meshworm	64
3.9 Summary	73
4 Investigations on SMA spring based actuators towards bio-inspired robotic fish	
4.1 Introduction	74
4.2 Fish Bio Mechanics	75
4.3 Modeling of SMA robotic fish	77
4.4 Fabrication of the proposed fish	82
4.5 Performance Evaluation	84
4.6 Summary	93
5 Investigations on SMA bimorph towards bio-inspired soft robot	
5.1 Introduction	94
5.2 Design of SMA Bimorph based soft Robot	94
5.3 Modeling of SMA bimorph	95
5.4 Fabrication of SMA bimorph	96
5.5 Performance Evaluation	99
5.5.1 Experimental setup for actuation and motion control	99
5.5.2 Actuation capability of SMA bimorph actuator	99
5.5.3 Shape Recovery Analysis	102
5.5.4 Controller Design	102
5.5.5 Investigation on control of the bimorph	104
5.5.6 SMA bimorph based soft robot prototype	108
5.6 Summary	110
6 Investigations on SMA wire integrated polymer composite actuator towards soft robotic gripper	
6.1 Introduction	111
6.2 SMA/PDMS soft composite actuator	111
6.3 Modeling of SMA/PDMS soft actuator	112

6.4 Fabrication of the SMA soft actuator	114
6.5 Description of the experimental setup	116
6.6 Performance Evaluation	118
6.6.1 Actuation Characteristics of the proposed soft structure	118
6.6.2 Effect of pre straining of SMA wire	120
6.6.3 Life cycle Analysis	121
6.7 Development of SMA/PDMS based soft robotic gripper	122
6.8 Summary	124
7 Investigations on SMA wire integrated polyimide composite actuator towards soft robotic jellyfish	
7.1 Introduction	125
7.2 Modeling of the Polyimide/SMA tentacle	125
7.2.1 Kinematic modelling	125
7.2.2 Modeling of SMA wire temperature in tentacle	127
7.2.3 Beam Bending Theory	130
7.2.4 Hydrodynamic Analysis	133
7.3 Fabrication of the robot skeletal structure	135
7.4 Performance Evaluation	136
7.4.1 SMA effect on the proposed jellyfish	136
7.4.2 Investigations on displacement and bending	137
7.4.3 Thrust Measurement	139
7.4.4 Movement of Robotic jellyfish	139
7.5 Summary	144
8 Conclusions and scope for future work	
8.1 SMA spring based Bio-inspired soft meshworm	145
8.2 SMA spring based bio-inspired robotic fish	146
8.3 SMA bimorph based bio-inspired soft robot	147
8.4 SMA wire based soft robotic gripper	148
8.5 SMA wire based soft robotic jellyfish	149
References	151

LIST OF FIGURES

Fig. No	Title	Page No.
Fig. 1.1	(a) A soft gripper composed of a flexible sac filled with granular materials that can grasp a wide range of objects by vacuum pressure control. (b) A soft manipulator modeled on the characteristic muscle structure of the octopus. (c) The GoQBot, capable of the ballistic rolling motion observed in caterpillars. (d) A multigait soft walker powered by compressed air.	2
Fig. 1.2	Soft robot actuator technologies	3
Fig. 1.3	SMA crystal structures and the resultant behaviour due to transformation	4
Fig. 1.4	a) Shape memory effect b) Superelasticity	5
Fig. 1.5	SMA Spring	9
Fig. 1.6	DSC curve of SMA spring	9
Fig. 1.7	SMA wire embedded composite as robotic tongue	10
Fig. 1.8	a) SMA/Polyimide based bimorph b) SMA thin film based wings in dragonfly	11
Fig. 1.9	Different types of SMA coupled structures	12
Fig. 1.10	Different design incarnations of mechanical joint-coupled actuator with (a) A SMA wire, and (b) A SMA spring.	12
Fig. 1.11	SMA element attached at both ends of the actuator and located outside versus inside a polymer	13
Fig. 1.12	a) SMA based micro manta ray fish b) SMA based Jellyfish robot	14
Fig. 1.13	a) SMA spring b) SMA wire embedded composite c) SMA bimorph	15
Fig. 2.1	SMA wire embedded SSC based inchworm robot	18
Fig. 2.2	SMA wire /GFRP composite based inchworm robot	19
Fig. 2.3	a) SMA wire embedded soft morphing structure based inchworm robot b)crawling motion	19
Fig. 2.4	SMA spring based meshworm robot	20
Fig. 2.5	SMA coil based inchworm robot	21
Fig. 2.6	BISMAC based Robojelly	22
Fig. 2.7	Jellyfish like mini robot	23

Fig. 2.8	IPMC actuated robotic jellyfish	24
Fig. 2.9	Self-propelled jellyfish robot based on six-bar linkage mechanisms	24
Fig. 2.10	Jellyfish robot based on barycenter adjustment mechanism	25
Fig. 2.11	Dielectric elastomer based jellyfish	26
Fig. 2.12	Hydraulic based soft robotic jellyfish	27
Fig. 2.13	hydrogen fuel powered jellyfish robot	27
Fig. 2.14	SMA spring based flexural caudal fin propulsion	28
Fig. 2.15	SMA wire based micro manta ray fish robot	29
Fig. 2.16	Robotic fish based on chemical sensors	30
Fig. 2.17	SMA wire actuated biomimetic fin	31
Fig. 2.18	ICPF actuated underwater microrobot	31
Fig. 2.19	Polypyrrole actuator based robot fish	32
Fig. 2.20	SMA based bendable structured robotic fish	33
Fig. 2.21	DEA based soft robotic fish	33
Fig. 2.22	Flexible SMA pectoral fin	34
Fig. 2.23	SMA thin film based dragonfly	36
Fig. 2.24	SMA based micro manipulator	37
Fig. 2.25	NiTi thin sheet based micro gripper	37
Fig. 2.26	TiNi/DLC based microgauge	38
Fig.2.27	Methodology	41
Fig. 3.1	a) Temperature distribution of nitinol SMA spring in COMSOL at the end of heating cycle b) Temperature distribution of nitinol SMA spring in COMSOL at the end of cooling cycle	44
Fig. 3.2	Heating and Cooling curve of nitinol SMA spring	46
Fig. 3.3	a) Peristaltic crawling b) Two anchor crawling	47
Fig. 3.4	Soft meshworm structure at different SMA phases	48
Fig. 3.5	Fabrication process of softworm skeletal structure	49
Fig. 3.6	Behaviour of PET under loading condition	50
Fig. 3.7	a) Block diagram of Softworm setup b) Softworm experimentation	51
Fig. 3.8	SMA spring a) in line with Soft worm for bending analysis b)wound around c) Radial muscle	52

	configuration	
Fig. 3.9	Schematic of proposed two anchor crawling structure and bending	53
Fig. 3.10	Schematic of load Analysis	54
Fig. 3.11	Behavior of SMA spring with bias loads a) 1.5 N, b) 2.5 N and c) 3.5 N	56
Fig. 3.12	Bending angle during actuation of SMA spring	57
Fig. 3.13	Comparison of various bending angles and their recovery	58
Fig. 3.14	Percentage recovery for various bending angles	59
Fig. 3.15	Variation of bending angles with change in duty cycle	59
Fig. 3.16	Thermographic images for Duty cycle a) 4 % b) 6% c) 8 %	60
Fig. 3.17	Variation in bending angles for different current	61
Fig. 3.18	Bending curve for peristaltic crawling	61
Fig. 3.19	Bending curve for two anchor crawling	62
Fig. 3.20	a-c) Peristaltic locomotion to maneuver a single stair arrangement d-f) Bending action of Two anchor locomotion	63
Fig. 3.21	Flex sensor arrangement	63
Fig. 3.22	Experimental setup for the laser actuation of SMA spring	65
Fig. 3.23	Number of passes required to initiate the actuation in the spring for various powers	67
Fig. 3.24	schematic of the typical heating and cooling curve during ON and OFF of laser irradiation	68
Fig. 3.25	a) Heating time vs. Power Graph b) Cooling time vs. Power Graph	68
Fig. 3.26	Required number of passes with respect to increase in laser power for complete strain recovery	69
Fig. 3.27	Influence of laser power on the displacement for the loads 1.5 N, 2.5 N and 3.5 N	70
Fig. 3.28	Laser actuation of soft mesh structure	71
Fig. 3.29	Soft mesh structure bending during laser actuation	72

Fig. 3.30	Bending time with varying power	72
Fig. 4.1	a) Configuration of the proposed bio-inspired robotic fish in mm and b) Skeletal structure of the proposed bio-inspired robotic fish	77
Fig. 4.2	Mesh structure of fish	77
Fig. 4.3	Mesh structure of fish planar view	78
Fig. 4.4	a) Solid works model b) Adams model	78
Fig. 4.5	a) Adams simulation stills of the proposed SMA based robotic fish and b) Tail position at 0.1Hz and 0.5Hz	79
Fig. 4.6	Planar configuration for the proposed bio-inspired robotic fish	80
Fig. 4.7	Kinematic configuration of the proposed robotic fish	81
Fig. 4.8	Simulation of caudal fin angle	82
Fig. 4.9	Fabrication and validation of proposed bio-inspired robotic fish design	83
Fig. 4.10	Final robotic fish prototype	84
Fig. 4.11	Experimentation of robotic fish without head	84
Fig. 4.12	Control circuit of the SMA spring based robotic fish	85
Fig. 4.13	a) Experimentation in water and b) Robotic fish experimentation in tank	86
Fig. 4.14	Experimentation with inbuilt electronics	86
Fig. 4.15	a) Displacement curve plotted using Laser Displacement Sensor and b) Experimental setup for displacement measurement	88
Fig. 4.16	4.16 a) Maximum Angle (Amplitude) measurement in air, b) Schematic of the angle measurement and c) Maximum Angle (Amplitude) measurement in water	89
Fig. 4.17	Robotic Fish demonstration at various time instances	89
Fig. 4.18	Force produced by the proposed SMA mechanism	90
Fig. 5.1	Design of the SMA bimorph based soft robot	95
Fig. 5.2	Temperature distribution of SMA bimorph	96
Fig. 5.3	Schematic of thermal evaporation technique	97
Fig. 5.4	Developed bimorph with different substrate thickness	97
Fig. 5.5	DSC plot of CuAlNiMn SMA Bimorph	98

Fig. 5.6	a)Schematic of Experimental Setup b) Actual image of experimental setup	99
Fig. 5.7	Voltage vs. displacement curve with different substrate thickness	100
Fig. 5.8	Time vs. displacement curve for 2 V and 3 V	101
Fig. 5.9	Maximum displacement with different loads	101
Fig. 5.10	Shape recovery analysis of SMA bimorph	102
Fig. 5.11	Block diagram of PID control of SMA bimorph actuator	103
Fig. 5.12	Displacement Stability for gain $K_p = 9.5$ (set point of 0.5 mm)	105
Fig. 5.13	Time vs. Displacement for set point of 0.5 mm using standard parameter Z-N method	106
Fig. 5.14	Set point control for 0.6 mm	107
Fig. 5.15	Set point control for 0.7 mm	107
Fig. 5.16	Set point control for 1 mm	108
Fig. 5.17	SMA bimorph based soft robot	108
Fig. 5.18	Preliminary prototype of the proposed SMA bimorph actuator based soft robot for MEMS applications	109
Fig. 5.19	Experimental Setup	109
Fig. 6.1	Temperature distribution in the structure at a) 2 A b) 4 A c) 6 A d) 8 A	113
Fig. 6.2	Current vs. Temperature	113
Fig. 6.3	Thermography image for Surface temperature at a) 4A b) 6A c) 8A	114
Fig. 6.4	Fabrication process of SMA based soft actuator	116
Fig. 6.5	Fabricated SMA/PDMS based soft actuator	116
Fig. 6.6	Schematic of the experimental setup	117
Fig. 6.7	Real time Experimental setup	117
Fig. 6.8	Tip displacement of the soft actuator	119
Fig. 6.9	Permanent deformation at higher current	119
Fig. 6.10	SMA wire pre-straining effect on the soft structure	120
Fig. 6.11	Prestraining effect on displacement	120
Fig. 6.12	Life cycle analysis of the proposed actuator	121

Fig. 6.13	SMA/PDMS based soft robotic gripper	122
Fig. 6.14	Object falls down before the actuation of SMA/PDMS soft actuator	123
Fig. 6.15	Soft gripper demonstration with varying payload and different geometries	123
Fig. 7.1	Kinematic configuration of tentacle	126
Fig. 7.2	Tentacle dynamic simulation as 3 link manipulator	127
Fig. 7.3	Tentacle dynamic simulation using ADAMS	127
Fig. 7.4	Variation of SMA wire temperature with current	130
Fig. 7.5	Schematic of the model that extracts the bending moment (inset showing the actual image of the tentacle)	130
Fig. 7.6	Tentacle deflection	133
Fig. 7.7	a) Pressure contours during bell contraction, b) Pressure contours during bell expansion and c) vortex formation visualized via streamlines	134
Fig. 7.8	Thrust force	135
Fig. 7.9	Fabrication process of the proposed soft robotic jellyfish a) Kapton polyimide sheet, b) carved out jelly fish shape with holes punched in it, c) SMA wires are inserted into the holes, d) Kapton tape is pasted over the SMA wires (inset showing the cross section of the composite structure), e) and f) schematic and actual image of the bell structure with attached rubber strings	136
Fig. 7.10	Tentacle displacement with varying SMA wire diameter	137
Fig. 7.11	Thermal images of FLIR Camera	137
Fig. 7.12	Frequency of tentacle a) 0.5 Hz b) 1 Hz c) 2 Hz	138
Fig. 7.13	Proposed Jellyfish with camera, sensors and electronic Control System Tentacle bending angle	138
Fig. 7.14	Thrust force measurement setup	139
Fig. 7.15	Position of jellyfish at different time instances	140
Fig. 7.16	Position of jellyfish at different time instances in vertical orientation	141
Fig. 7.17	Experimentation of jellyfish robot with bias load	142
Fig. 7.18	Experimentation of jellyfish robot with bias load and	142

	onboard electronics	
Fig. 7.19	Experimentation of jellyfish robot with bias load with on onboard electronics covered with 3D printed bell structure	142
Fig. 7.20	SMA/polyimide based jellyfish prototype for underwater object detection	143
Fig. 8.1	Prototype of SMA spring based soft meshworm	146
Fig. 8.2	Prototype of SMA spring based robotic fish	147
Fig. 8.3	Prototype of SMA bimorph based soft robot	148
Fig. 8.4	Prototype of SMA wire based soft robotic gripper	149
Fig. 8.4	Prototype of SMA wire based soft robotic jellyfish	150

LIST OF TABLES

Table. No	Title	Page No.
Table 1.1	Commercial NiTi SMA physical properties	7
Table 1.2	CuAlNi SMA properties	7
Table 1.3	Comparison of properties of NiTi, Cu-Zn-Al and Cu-Al-Ni	7
Table 3.1	Spring simulation properties	45
Table 3.2	Validation of SMA spring with thermography	46
Table 3.3	Tensile test parameters	49
Table 3.4	Spring recovery under various loading conditions.	57
Table 4.1	DH parameter table	81
Table 4.2	Critical design parameters for robotic fish	91
Table 5.1	Composition of CuAlNiMn Bimorph	98
Table 5.2	Cumulative error for various proportional gain	104
Table 6.1	Validation of simulation with thermography image	114
Table 6.2	Properties of PDMS	115
Table 6.3	Properties of SMA wire	115
Table 7.1	DH parameter table	126
Table 7.2	Parameters used for simulation	129

NOMENCLATURE

Symbol	Unit	Description
σ_s	MPa	Detwinning start stress
σ_f	MPa	Detwinning finish stress
P	Kg/m ³	Density
C _p	J/Kg K	Specific heat
U	m ³ /s	velocity of flow
K	W/m K	thermal conductivity
H _c	W/m ² K	convective coefficient
J	A m ⁻²	Current Density
E	V/m	Electric Field
V	Volt	Electric potential
I	A	Current passed through the wire
R	Ω	Resistance of the wire
M	g	Mass of the wire

ACRONYMS

S. No	Acronym	Expansion
1	SMA	Shape memory alloys
2	OWSME	One way shape memory effect
3	TWSME	Two way shape memory effect
4	SME	Shape memory effect
5	A_s	Austenite start temperature
6	A_f	Austenite finish temperature
7	M_s	Martensite start temperature
8	M_f	Martensite finish temperature
9	PDMS	Polydimethylsiloxane
10	PET	polyethylene terephthalate
11	LDS	Laser displacement sensor
12	DAQ	Data acquisition system
13	MEMS	Micro electro mechanical system
14	DH	Denavit-Hartenberg
15	BCF	Body caudal fin
16	MCF	Median/Paired fin
17	UV	Ultraviolet
18	ABS	Acrylonitrile Butadiene Styrene
19	PID	Proportional Integral Derivative
20	DSC	Differential scanning calorimetry
21	LIFA	LabVIEW through Interface for Arduino

22	IAE	Integral absolute error
23	Z-N	Zeigler Nichol's

Chapter 1

Introduction to Bio-inspired soft robotics and shape memory alloys

1.1 Bio-inspired Soft Robotics

Conventional robots and machines are made of rigid materials that limit their ability to elastically deform and adapt their shape to external constraints and obstacles. Although they have the potential to be incredibly powerful and precise, these rigid robots tend to be highly specialized and rarely exhibit the rich multifunctionality of natural organisms [1-5]. The natural creatures are made of soft materials. Soft robotics is an emerging topic in the field of robotics which challenges the traditional engineering thinking. Using this technology, it can be possible to create robotic systems with flexible structures completely made of soft materials.

Living creatures made of soft structures to move effectively in complex natural environments. These capabilities have inspired robotic engineers to incorporate soft material technologies into their designs. The goal is to endow robots with new, bioinspired capabilities that permit adaptive, flexible interactions with unpredictable environments. Incorporating soft technologies can potentially reduce the mechanical and algorithmic complexity involved in robot design. Incorporating soft material technologies will also expedite the evolution of robots that can safely interact with humans and natural environments.

Soft robots contain little or no rigid material and are instead primarily composed of fluids, gels, soft polymers, and other easily deformable matter (Fig.1.1). Soft robots have the potential to change the way we

construct intelligent systems. By using highly deformable and stretchable materials, we can build robots that safely interact with human operators and function in unstructured environments. Soft robots are composites of flexible materials that together give rise to entirely new modes of function and behavior, in many ways not unlike natural biology [6-10].

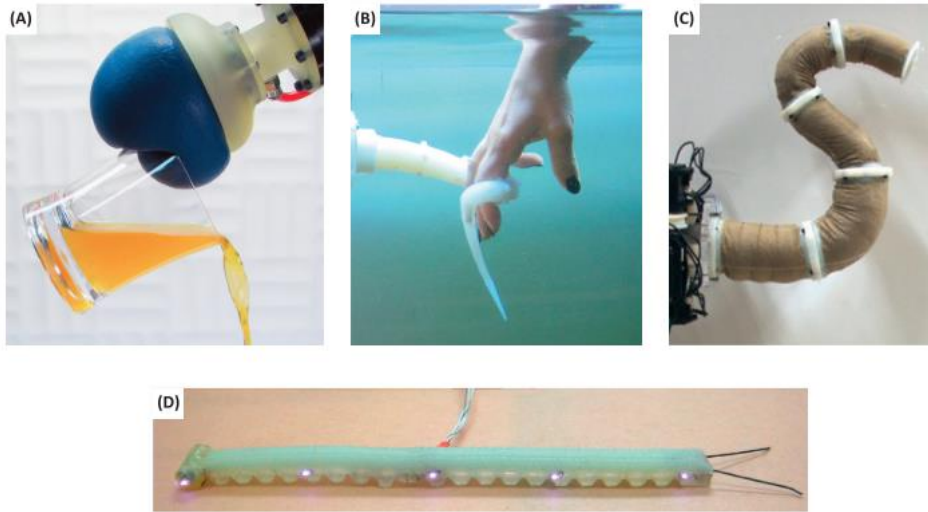


Fig.1.1: (a) A soft gripper composed of a flexible sac filled with granular materials that can grasp a wide range of objects by vacuum pressure control [11]. (b) A soft manipulator modeled on the characteristic muscle structure of the octopus [12]. (c) The GoQBot, capable of the ballistic rolling motion observed in caterpillars [13]. (d) A multigait soft walker powered by compressed air [14].

Conventional bio-inspired robots are made of complicated rigid materials and mechanisms actuated by motors, that limit their performance due to lack of flexibility. Conventional motor based bio inspired robot creates more noise and rigid. These issues limit its applicability for marine life monitoring as it may strike or disturb the marine species. There is a lot of scope to explore the alternative actuators to produce flexible and complex movements which is not possible with motor based actuators. The soft actuator technologies are shown in Fig. 1.2. Dielectric elastomer (silicon), SMA, pneumatic muscle, Ionic Polymer–Metal Composite (IPMC),

ferromagnetic polymers and piezoelectric polymers are the established soft robotic actuator technologies [3]. SMA actuators are able to generate large displacements with simple mechanisms.

In bioinspired soft robotics, soft materials such as polydimethylsiloxane (PDMS), polyethylene terephthalate (PET), silicone etc. is used along with smart materials such as SMA etc. The combination of soft and smart materials provides more flexibility/capabilities to the robots and ensures safety of the humans as well as natural species.

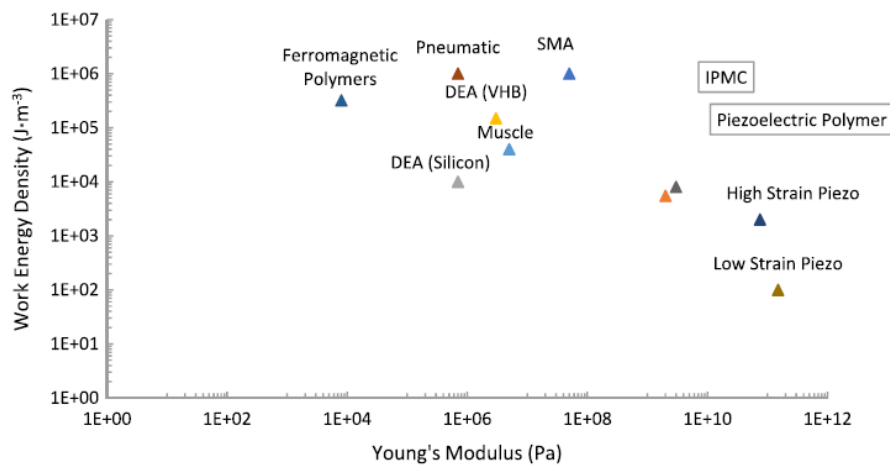


Fig. 1.2: Soft robot actuator technologies

1.2 Shape Memory Alloy

Shape memory alloys (SMA) are smart materials having distinctive behaviour such as shape memory effect and pseudoelasticity. A reversible solid state displacive phase transformation from austenite to martensite is the reason behind the smart behaviour. SMAs are metallic alloys and categorised as NiTi based alloys (NiTi, NiTiCu), copper based alloys (CuZnAl, CuAlNi) and iron based alloys (FeNiCoTi, FeMnSi). The SMAs exhibit high actuation energy densities and have capabilities to recover their shape under large applied loads.

SMA can exist in two phases having three different crystal structures viz. twinned martensite, detwinned martensite and austenite. The martensite is a low temperature phase while the austenite is stable at high temperatures. The phase transformations have characteristic start and finish temperatures and gives information about the operating range of an alloy. M_s , M_f , A_s and A_f are the characteristic temperatures of the martensite and austenite transformations. Fig. 1.3 shows the stress-strain-temperature diagram of a SMA, crystal structures and the possible phase transformations. Moreover, it shows all the functional behaviour of a shape memory alloy viz. One way shape memory effect (OWSME), two way shape memory effect (TWSME) and pseudoelasticity. OWSME is widely explored and has been applied to variety of applications. However, the TWSME is less utilized for applications due to the intense training requirements and less strain recovery than OWSME.

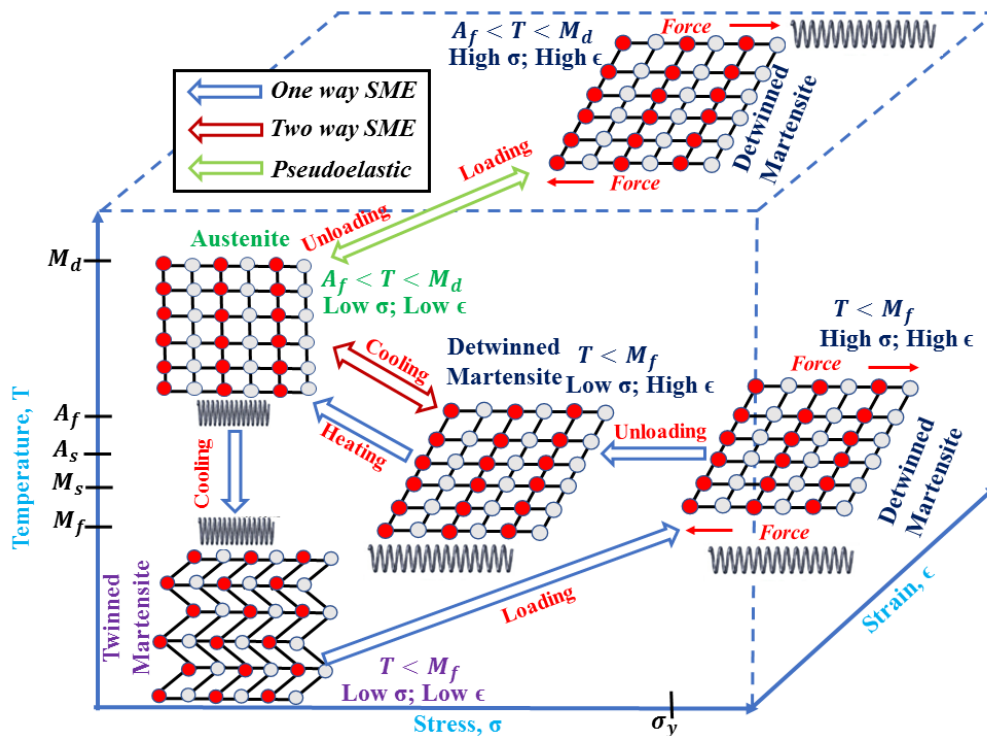


Fig. 1.3: SMA crystal structures and the resultant behaviour due to transformation

The shape memory alloys exhibits shape memory effect (SME)

which is the property of remembering and recuperating their original shape upon thermal stimuli [15-16]. When a SMA is deformed at low temperature (below A_s), it can be switched to de-twinned martensite state through the application of load. The de-twinning process can be reversed by providing heat energy to the SMA. On supplying heat, the crystal arrangement of the SMA material absorbs energy and reorients itself from de-twinned martensite crystal structure to austenite crystal structure at a temperature above A_s . This change in the crystallographic plane is echoed on a macroscopic level, thus observing the shape recovery [17-18].

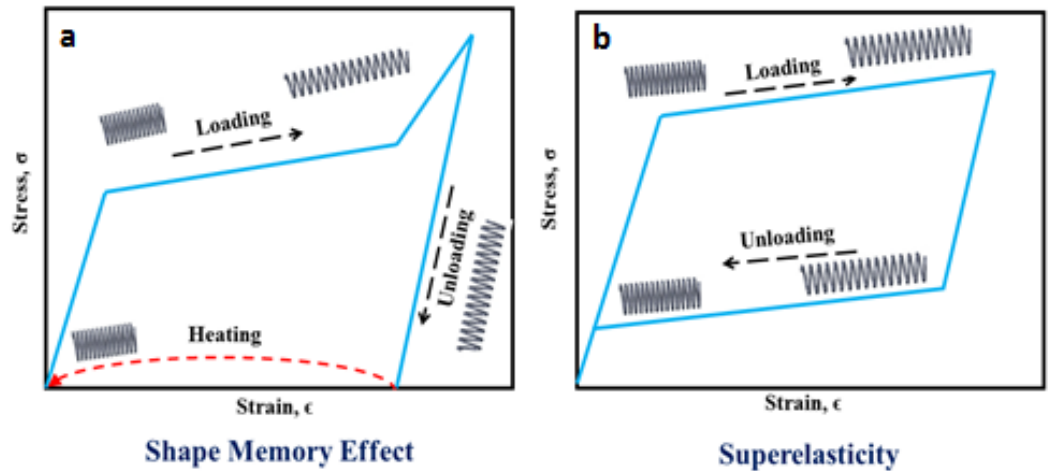


Fig. 1.4: a) Shape memory effect b) Superelasticity

The pseudoelasticity effect or superelasticity is the strain recovery driven by stress induced martensite transformation (SIM) i.e. the SMA at temperatures above the austenite finish temperature (A_f) can recover the strain completely upon unloading [19]. At temperatures above A_f (stable austenite exists), the pseudoelastic path can initiate and develop under the application of external load which leads to formation of detwinned martensite state. On removal of load, the path reverses and stable austenite forms at no load condition or stress free state. The typical pseudoelastic behaviour of SMA is shown in Fig.1.4.

Nickel-Titanium or Nitinol alloys are widely used SMA due to their exhibition of excellent mechanical properties, thermomechanical behaviour, pseudoelasticity and biocompatibility. They have highest work density and large deformation recovery among other SMA compositions [20]. It is the most studied SMA alloy system and has been applied in variety of commercial applications. In addition to mechanical properties, the transformation temperatures are one of the most important characteristics which decide the applicability of the SMA. The commercial application of NiTi alloys has developed in many areas due to the greater demands for lighter and more compact actuators, especially in the biomedical sector. Some of the SMAs physical and mechanical properties also vary between the two phases (martensite and austenite) such as Young's modulus, electrical resistivity, thermal conductivity and thermal expansion coefficient. The austenite structure is relatively hard and has a much higher Young's modulus; whereas the martensite structure is softer and more malleable; i.e. can be readily deformed by application of an external force. When an external stress is applied below the martensite yield strength (approximately 8.5% strain for NiTi alloys and 4–5% for copper-based alloys), the SMA deforms elastically with recoverable strain. However, a large non-elastic deformation (permanent plastic deformation) will result beyond this point.

Equiatomic composition of NiTi can exhibit a maximum austenite finish temperature (A_f) of 120°C. By changing the Ni composition, the transformation temperatures can be tailored based on the application. At the Ni composition of 51 %, it can exhibit a lowest A_f of -40°C. Based on the composition and the manufacturing conditions, the NiTi alloy can exhibit either shape memory effect or pseudoelasticity at room temperature. The transformation temperature of copper based SMA is higher than NiTi and it is non-biocompatible. Table 1.1 and 1.2 shows the

properties of NiTi and CuAlNi SMA. Table 1.3 show the comparison of different SMAs.

Table 1.1: Commercial NiTi SMA physical properties.

Property	Units	Value Martensite	Value Austenite
Density	kg/m ³	6450–6500	
Electrical Resistivity	$\mu\Omega$ cm	76-80	82-100
Specific Heat Capacity	J/kg K	836.8	836.8
Thermal Conductivity	W/m K	8.6-10	18
Thermal Expansion Coefficient	m/m K ⁻¹	$6.6 * 10^{-6}$	$11.0 * 10^{-6}$
Ultimate Tensile Strength	MPa	895 (fully annealed) 1900 (Hardened)	
Young's Modulus	GPa	28-41	75-83
Yield Strength	MPa	70-140	195-690
Poisson's Ratio	-	0.33	
Magnetic Susceptibility	μemu g	2.5	3.8

Table 1.2: CuAlNi SMA properties

Alloy composition	Transformation temperature range (°C)	Thermal Hysteresis(°C)	Strain (%)	Recovery (%)
Cu-Al-Ni	100-400	21.5	3-5PE	80-90PE

Table 1.3 Comparison of properties of NiTi, Cu-Zn-Al and Cu-Al-Ni

Properties	NiTi	Cu-Zn-Al	Cu-Al-Ni
Melting temperature (°C)	1300	950-1020	1000-1050
Transformation range (°C)	-200~110	<120	<200

Hysteresis (°C)	30-50	15-25	15-20
Recovery Strain (%)	8.5	4	4
Recovery stress	500 Mpa	200 Mpa	150 Mpa
Number of cycles	105	102	102
Corrosion resistance	Excellent	Problematic	Better
Machinability	Poor	Fair	Fair

1.3 Applicability of different geometrical forms of SMA in soft robotics

For their own characteristics, SMAs are very well known in soft robotics and often taken into consideration when facing the actuation strategy to be chosen. The major advantage of this technology is its very high work density: the lighter the actuators, the bigger is the resulting power/weight ratio, therefore making SMAs a valid alternative to conventional actuators. Moreover, they are silent during operation and clean; they present high remotability and can be easily distributed to obtain local deformations with low driving voltages; they resist excellently to chemical corrosion and are generally biocompatible for their use in the medical field. On the other hand, some drawbacks limit the use of SMAs for specific applications: even if low driving voltage can be maintained, a relative high current is often required and it does not come with high energy efficiency (1–10%). From having a very high energy density and being usable in a variety of shapes, including rods, plates, ribbons, springs, and wires, SMAs have been used in a wide variety of applications. Among the different forms, spring and wire has been used widely in robotic applications [4].

SMA wires and springs have a large recovery strain that makes them ideal to produce large forces. However, their limited recoverable

strain in the range of 4–8% requires them to have lengths up to 25 times longer than their intended stroke length. An alternative has been to turn the SMA wires into SMA springs through thermal training or even double-coil SMA springs. By turning the SMA wires into springs, the actuation stroke can be greatly increased up to 200–1000% of their original actuation stroke, but the maximum force generated by the SMA is greatly decreased. Although both wires and springs are capable sources of one-dimensional actuation, their deformation has to be coupled to another element to transform their linear deformation into an out-of-plane deformation [4]. Fig.1.5 shows the schematic of SMA spring.

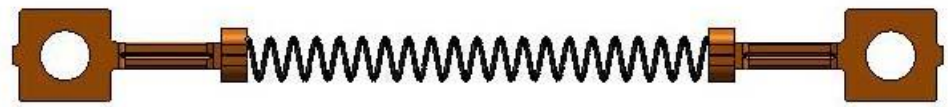


Fig. 1.5: SMA Spring [21]

The phase transformation temperature of SMA was identified using differential scanning calorimetry (DSC). Fig.1 shows the DSC curve of the NiTi SMA spring. The martensite and austenite temperatures are $M_s=31^\circ\text{C}$, $M_f = -23^\circ\text{C}$, $A_s = -25^\circ\text{C}$ and $A_f = 35^\circ\text{C}$ respectively.

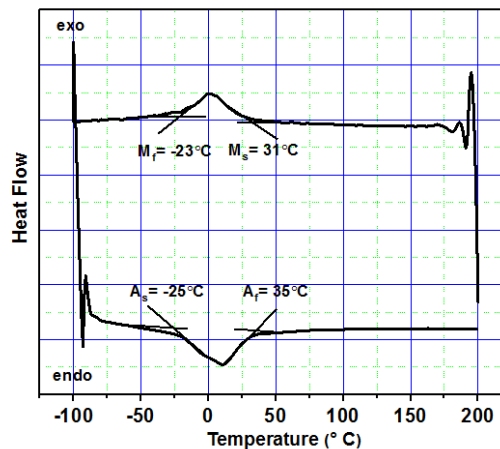


Fig.1.6: DSC curve of SMA spring

Embedding SMA wires in a soft polymeric matrix, it is possible to couple the limited deformation of the wires with that of the matrix and to produce large continuous deformations of the matrix. This type of composite actuator, called Smart Soft Composite (SSC) actuator, is typically used to produce bending motions and has been used in diverse applications. Fig.1.6 shows the SMA wire embedded SSC as robotic tongue.

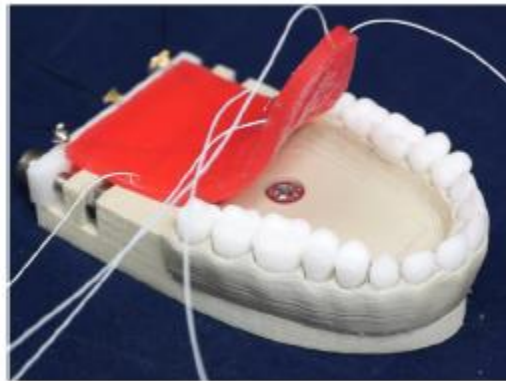


Fig. 1.7: SMA wire embedded composite as robotic tongue [22]

However, the actuation frequencies are comparably low for SMA bulk structures like spring, wire and plate etc., due to the associated thermal inertia or slow dissipation of heat from the material during cooling. SMA thin films can exhibit better actuation frequencies compared to bulk materials due to the increased surface area to volume ratio. The thin film provides only one way shape memory effect. In order to achieve two way shape memory effect in thin films, the SMA has been deposited on a flexible substrate which named as SMA bimorph. Here the SMA thin film acts as active layer and flexible substrate acts a passive layer. SMA bimorph (Fig.1.7a) can be used in robotic applications as shown in Fig.1.7b.

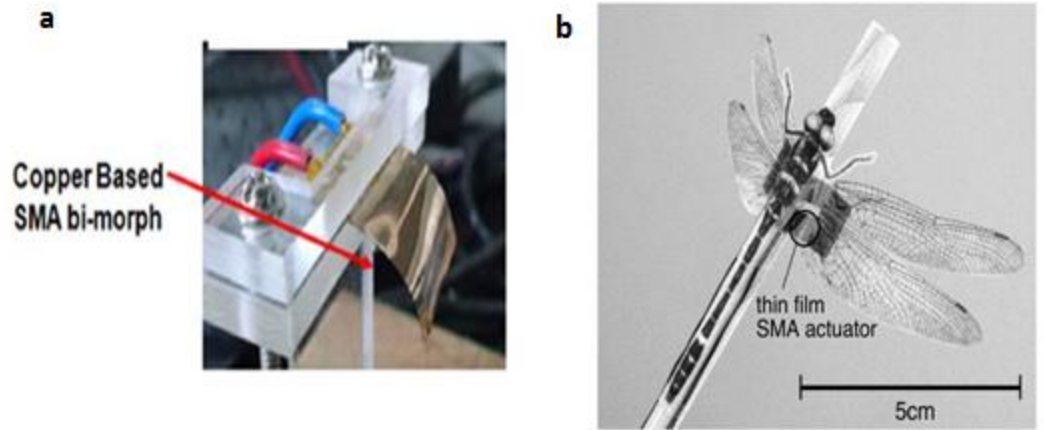


Fig. 1.8: a) SMA/Polyimide based bimorph [23] b) SMA thin film based wings in dragonfly [24]

It is possible to produce rigid out-of-plane deformations by using rigid elements with mechanical joints or flexural hinges that are deformed in three dimensions by the one-dimensional deformation of the wire or spring. An alternative to these rigid motions is to use a soft structure to produce a soft motion that is characterized by continuous, smooth, and biomimetic deformations that are useful for a range of applications. This can be achieved by coupling the deformation of the SMA element with a mesh or a polymeric matrix where the SMA element is fixed externally at multiple points on the structure or where the SMA element is bonded to the structure. The characterization of the different types of SMA wire or spring-coupled structures is shown in Fig.1.8.

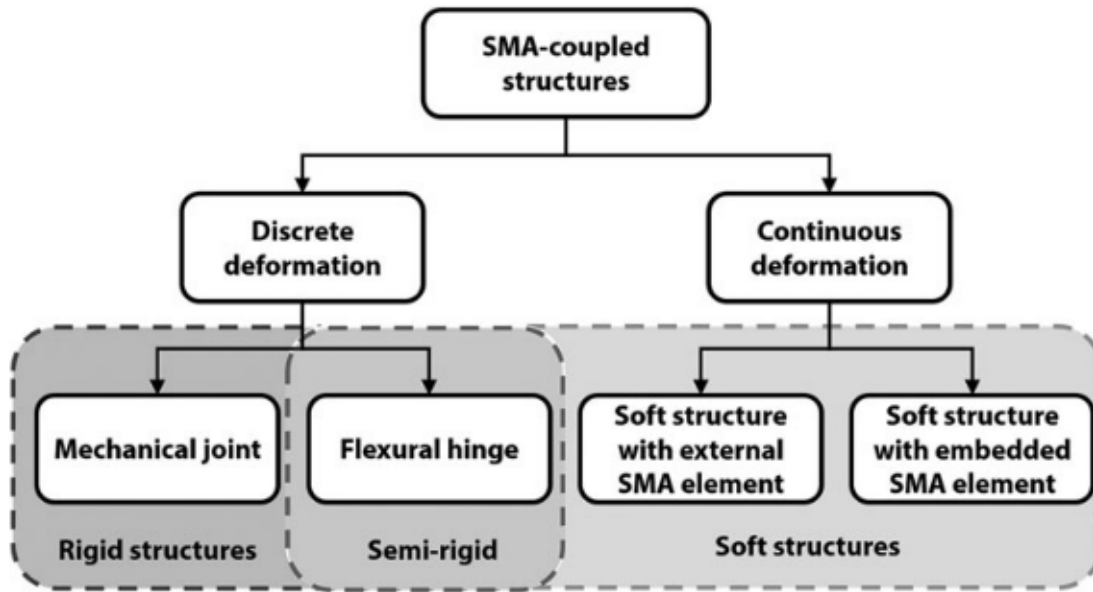


Fig.1.9: Different types of SMA coupled structures [4]

The most basic method for transforming the one-dimensional deformation of SMA wires and spring into an out-of-plane deformation is to couple its deformation with that of a rotating element, such that the linear contraction of the SMA element rotates the mechanical joint.

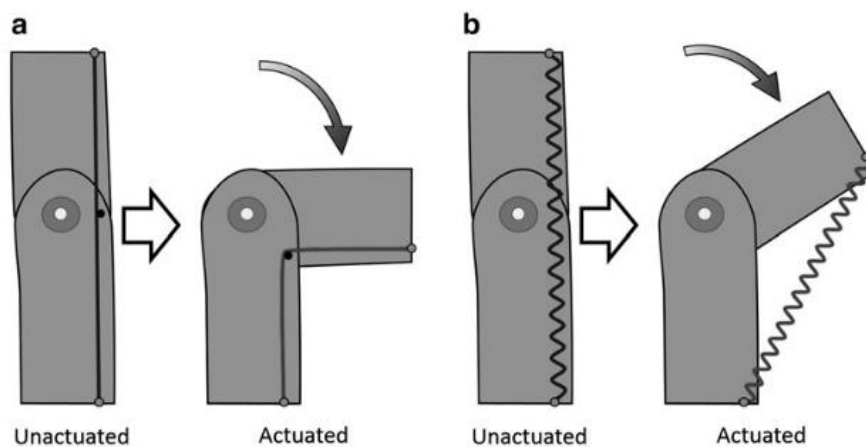


Fig.1.10: Different design incarnations of mechanical joint-coupled actuator with (a) a SMA wire, and (b) a SMA spring. [4]

The SMA wire can be placed externally with a polymeric matrix. It can be embedded into the polymeric matrix as shown in Fig. 1.10.

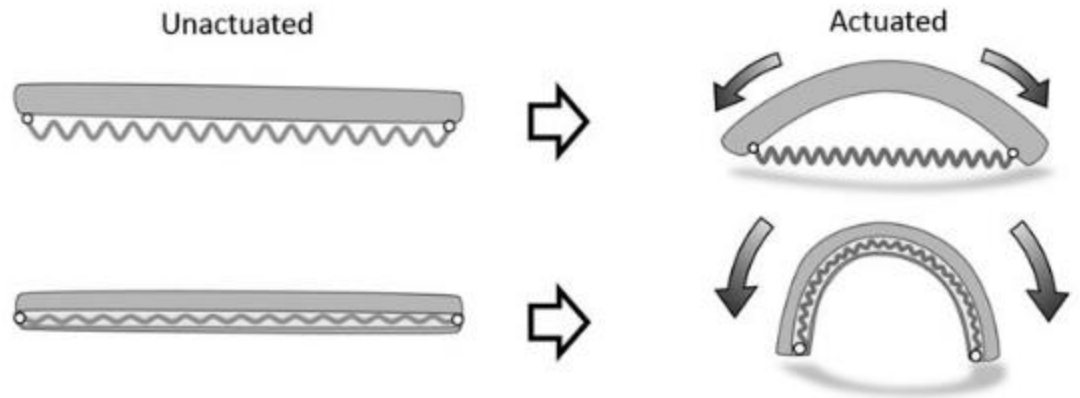


Fig.1.11 Comparison of SMA element attached at both ends of the actuator and located outside versus inside a polymer [4]

1.4. Application of SMA in bioinspired robotics

NiTi SMAs has been applied to various applications. Some of the interesting applications of SMA in bio-inspired robot development have been discussed in this section. The shape memory effect can be triggered thermally i.e. the increase in temperature will induce the shape recovery. This phenomenon of shape recovery favours the SMA to be used as actuators in various robotic applications. Various SMA actuated bio-inspired robots like robotic gripper, robotic fish, robotic jellyfish, robotic inchworm, turtle etc., has been developed. Fig.1.11a and b shows the robotic fish and jellyfish actuated through SMA as fins and tentacles respectively.

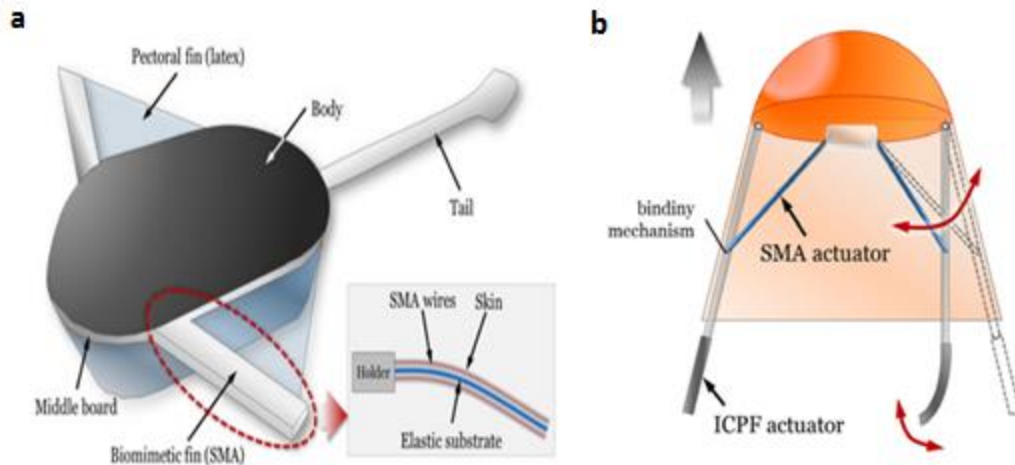


Fig.1.12: a) SMA based micro manta ray fish b) SMA based Jellyfish robot [25]

1.5 Motivation of the study

Conventional bio-inspired robots are made of complicated rigid materials and mechanisms actuated by motors, that limit their performance due to lack of flexibility. Conventional motor based bio inspired robot creates more noise and rigid. These issues limit its applicability for monitoring of natural species as it may strike or disturb it. Using soft robotics it is possible to create robotic systems with flexible structures completely made of soft materials. There is a lot of scope to explore the alternative actuators to produce flexible and complex movements which is not possible with motor based actuators. The use of soft materials and smart actuators can improve the flexibility like real creatures and results in high maneuverability.

The smart material based actuators are one of the possible alternative solution. SMA will be a suitable candidate for the flexible actuators technology to mimic the gestures of living organisms. Though various bio inspired robots have been developed right from its inception, they are not capable of exactly mimicking the motion pattern of real creatures. SMA

based actuator produce no noise and enables the possibility to develop noiseless bio inspired robots. SMAs are available in various geometrical forms such as spring (Fig.1.12a), wire embedded soft composite (Fig.1.12b), and bimorph (Fig.1.12c) which can be suitably coupled or employed with soft materials to develop bioinspired robots.

Each of these structures presents good and diverse capabilities such that they have all been used in a wide range of robotic applications. So far various bio inspired robots have been developed right from its inception. But still, they are not capable of exactly mimicking the motion pattern of real creatures. The reason behind this is the use of rigid bodies in the existing methods which cannot provide flexible motion as like real living organism. The use of soft materials and smart actuators can improve the flexibility like real creatures which results in high maneuverability.

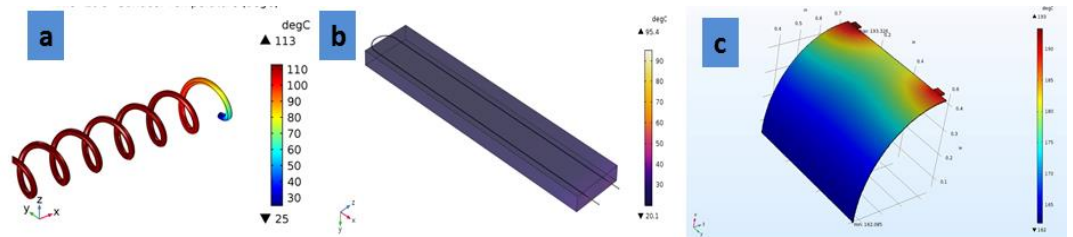


Fig.1.13: a) SMA spring b) SMA wire embedded composite c) SMA bimorph

1.6 Overall Objectives of the thesis

The thesis work aims to employ the different forms of SMA structures like spring, wire and bimorph towards the development of soft robots. The feasibility of SMA based structure in the development of bio-inspired soft robots has been investigated. The first primary objective is to explore the SMA spring based structures towards the development of bio-inspired soft robot. Under the first primary objective, the sub objectives are to Design and develop of SMA spring based soft meshworm robot and SMA spring based robotic fish. The second primary objective is to investigate the SMA

Bimorph towards the development of bio-inspired soft robots. The third primary objective is to investigate the SMA wire based structures towards the development of bio-inspired soft robot. Under the third primary objective, the sub objectives are to Design and develop of SMA wire/PDMS based soft gripper and SMA wire/Polyimide based soft jellyfish robot. Under each objective, modeling, fabrication and performance evaluation of the SMA based actuator have been carried out. The final prototype for each objective have been developed.

1.7 Outline of the thesis

Chapter 1: Introduction to Bio-inspired soft robotics and shape memory alloys

Chapter 2: Overview on the smart material based bio-inspired soft robotics

Chapter 3: Investigations on SMA spring based actuators towards bio-inspired soft meshworm

Chapter 4: Investigations on SMA spring based actuators towards bio-inspired robotic fish

Chapter 5: Investigations on SMA bimorph towards bio-inspired soft robot

Chapter 6: Investigations on SMA wire integrated polymer composite actuator towards soft robotic gripper

Chapter 7: Investigations on SMA wire integrated polyimide composite actuator towards soft robotic jellyfish

Chapter 8: Conclusions and scope for future work

Chapter 2

Overview on the smart material based bio-inspired soft robotics

2.1 Smart materials based inchworm robots

2.2.1 SMA wire based composite structures

Wang et al., [26] developed an inchworm-inspired biomimetic robot (Fig.2.1) using an SMA-based smart soft composite structure capable of mimicking the looping gait of an inchworm for both linear and turning locomotion. SMA wires are selected to implement the function of the longitudinal fibers of the inchworm, and PDMS is used to create the body of the inchworm robot since it is soft, isotropic, and bonds well with the SMA wires. Based on the different functions of the inchworm, the robot is comprised of three segments, referred to as the body and the feet. The robot achieved a stride length of 54 mm, which is nearly a third of its body length, with a linear speed of 3.6 mms⁻¹. This robot could be useful in rescue and reconnaissance missions where humans or larger robots are not capable of access. Furthermore, since this structure is simple, lightweight, and quiet, its principles could also be applied to other applications where flexibility and large deformation are required, such as wearable devices or other types of smart structures.

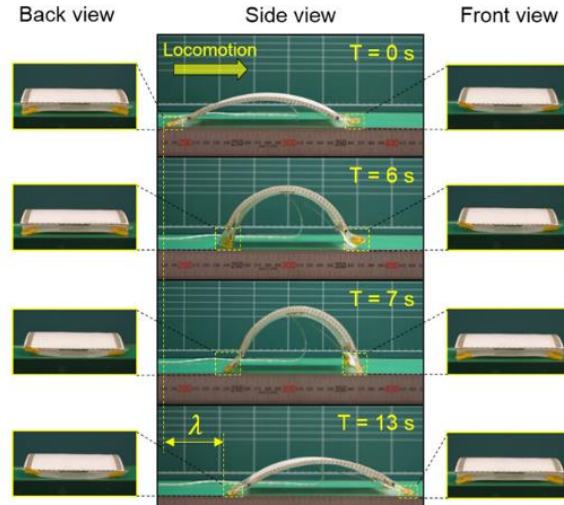


Fig. 2.1: SMA wire embedded SSC based inchworm robot [26]

Kim et al., [27] developed an inchworm robot (Fig.2.2). A wire SMA was embedded into an glass fiber reinforced polymer (GFRP) strip. The SMA composite inchworm robot was actuated by varying the radius of curvature in accordance with the applied power. This technique is possible to give repeated movement by applying power. Ni-Ti SMA wire was used as an actuation module for unidirectional motion. The GFRP composite and SMA wire were mechanically fastened to prevent delamination. The robot body was inserted to the groove of legs which have two different friction coefficients. The robot achieved 4.0 mm of movement over a 90 second interval.

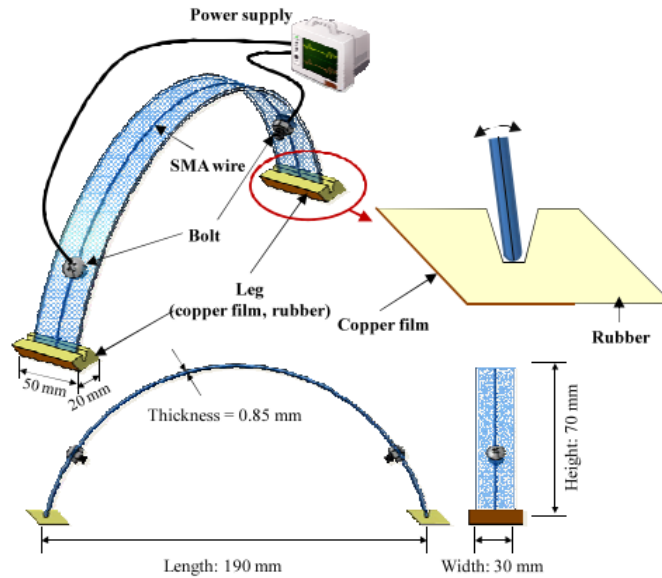


Fig. 2.2: SMA wire /GFRP composite based inchworm robot [27]

Kim et al., [28] developed an SMA-embedded soft morphing structure with large thickness and deformation. The smart structure consisted of two parts: the SMA wire actuator and the actual structure. The smart structure design was fabricated via a rapid prototyping and casting process. The material used for the skeleton was ABS, which is a stiff, thermoplastic polymer that is often used in structures. The performance of the prototype was evaluated, and visible actuation and a large actuation force were measured. The cell phone robot was suggested as an application, and the fabricated prototype (Fig.2.3a) of the device exhibited a perceptible crawling motion (Fig.2.3b).

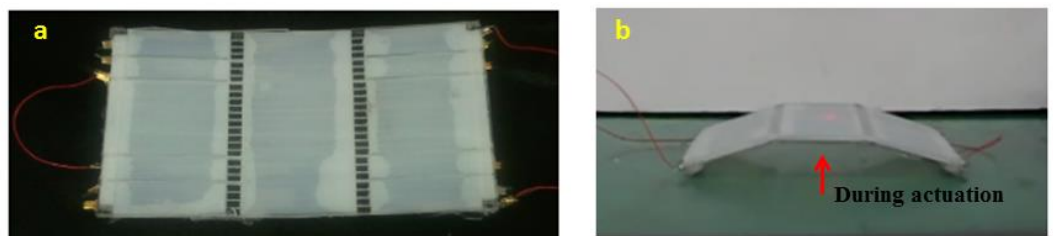


Fig. 2.3: a) SMA wire embedded soft morphing structure based inchworm robot b)crawling motion [28]

2.1.2 SMA spring based structures

Seok et al., [29] demonstrated a multisegmented soft robotic platform called the Meshworm (Fig.2.4), which can undergo peristaltic locomotion using NiTi coil spring actuators. The mesh-tube structure comprises multiple fibrillar spirals. Kinematically, each spiral is a stretched coil spring. With the addition of multiple longitudinal muscles distributed along the circumference, the robot can operate in three dimensions to overcome large obstacles and traverse rough terrain. Generating antagonistic actuation in a tubular soft structure, the robot can locomote using a peristaltic traveling wave along the length of its body from head to tail.



Fig. 2.4: SMA spring based meshworm robot [29]

Umedachi et al., [30] developed Softworms (Fig.2.5) uses SMA coils and motor tendons. Softworms use SMA coils running along the ventral surface. The SMA coil is pre-tensioned by stretching and installed. The upper surface is either flat or slightly curved to produce a semicircular cross-section. The lower surface has transverse ribs that act as supporting feet along the length of the body. Each rib is fabricated with one or more holes to create continuous channels through which the SMA coils or tendons can be threaded. These channels can be lined (during the printing process) with a thin layer of VeroClear™ to ensure that the SMA or tendon slides freely when the body bends and also to protect the soft

elastomer from abrasion and heating. These robots can be quickly fabricated by 3D printing and are capable of crawling and steering. They have used these simple machines to explore two different approaches to controlling highly deformable robots.

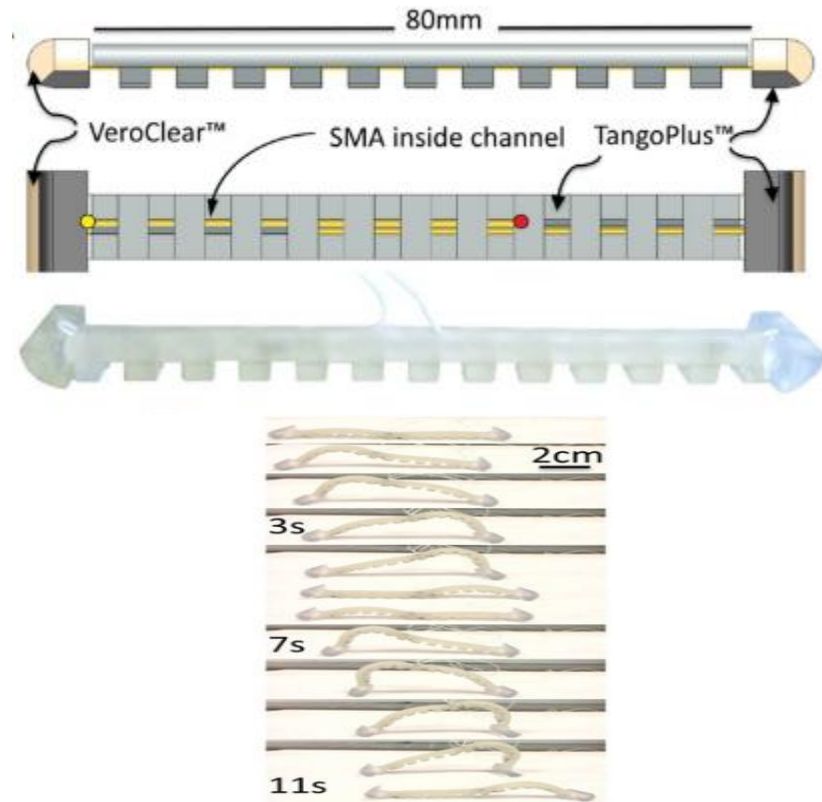


Fig. 2.5: SMA coil based inchworm robot [30]

2.2. Smart materials based jellyfish robots

Villanueva et al., [31] developed robotic jellyfish called Robojelly (Fig.2.6) with SMA-based BISMALC actuators. Bio- inspired shape memory alloy composite (BISMALC) actuators are made of silicone, SMA wires and spring steel. These actuators can convert the standard SMA deformation of 4% into a large deflection which can be further tailored by varying design parameters. Robojelly consists of a silicone matrix bell. It has eight BISMALC actuators embedded inside the silicone which are radially distributed around the bell. The Robojelly was able to produce

enough thrust to propel itself and achieve a proficiency of 0.19 s^{-1} which is comparable to the natural medusa at 0.25 s^{-1} . A folding effect was observed in the silicone bell which was found to decrease performance. The vehicle consumed an average of 16.74 W over its 14th cycle of actuation. The concept of BISMAC actuators was implemented but was not fully optimized for this vehicle.

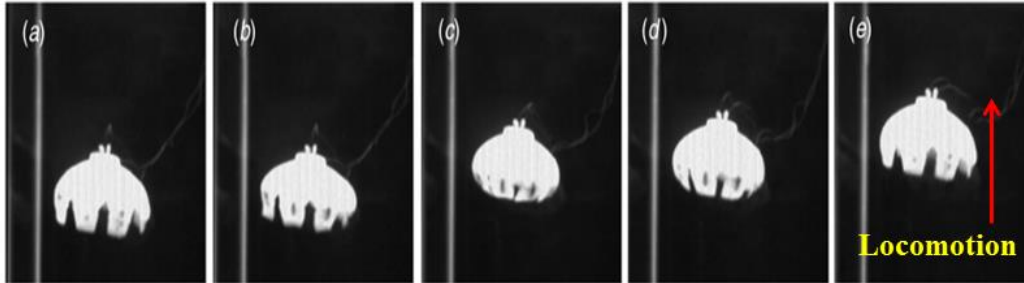


Fig. 2.6: BISMAC based Robojelly [31]

Ko et al., [32] proposed a jellyfish-like mini-robot (Fig.2.7) for a 3D space controlled by an external magnetic field, generated by three pairs of Helmholtz coils. The robot was designed and fabricated to mimic the motion of a real jellyfish. The robot consists of a main body with four fins, four neodymium permanent magnets, and a buoyant head in the center of the body. The robot body is 17 mm long and 0.5 mm thick. The cylindrical magnets with 1 mm diameter and 2 mm length are attached to the ends of the fins. In order to reduce the robot size to a microscale, the PDMS molding technique could be used. Through various basic tests of the robot, the 10 Hz square-type waveform was found to be appropriate for the actuating input current of the EMA system. Finally, 3D locomotion of the jellyfish-like mini-robot, using a 3 Hz square input current, was demonstrated.

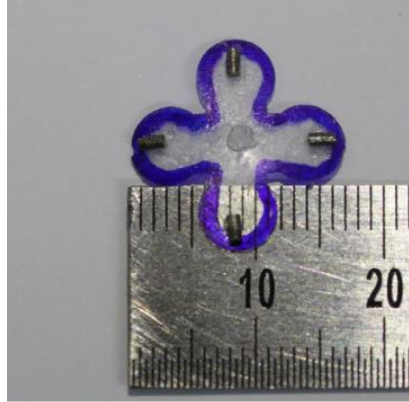


Fig. 2.7: Jellyfish like mini robot [32]

Yeom et al., [33] developed a biomimetic jellyfish robot (Fig.2.8) that is based on curved ionic polymer metal composite (IPMC) actuators. It is fabricated and activated for mimicking the real locomotion of jellyfish with pulse and recovery processes. To imitate the curved shape of the jellyfish, a thermal treatment was applied to obtain a permanent initial deformation of a hemispherical form. A bio-inspired input signal was generated for mimicking the real locomotion of the jellyfish with two-phase locomotion of pulse-recovery processes. The vertical floating displacement and force of the biomimetic jellyfish robot under various input signals were measured and compared. Unlike the pure sinusoidal excitation, the bio-inspired input signal that mimics the real locomotion of jellyfish induced much larger changes in the vertical floating displacement of the biomimetic jellyfish robot.

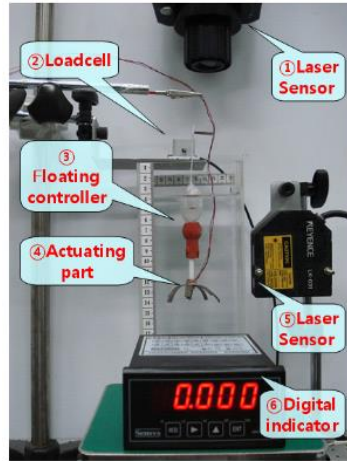


Fig. 2.8: IPMC actuated robotic jellyfish [33]

Xiao et al., [34] developed a novel self-propelled jellyfish robot based on six-bar linkage mechanisms (Fig.2.9) by mimicking the jet propelled swimming mechanism in jellyfish. The robotic jellyfish has a rigid head and a hollow body (hull), both of which are made of ABS material. The robotic jellyfish with four actuators exhibits similar propulsion behaviors. Four drive mechanisms and four actuators are centrally symmetric about the center axis of the cavity. An elastic rubber skin is enwrapped the actuators, thus the skin can move with the actuators to produce jet propulsion. By coordinately controlling the four actuators, the robot successfully achieves swimming.

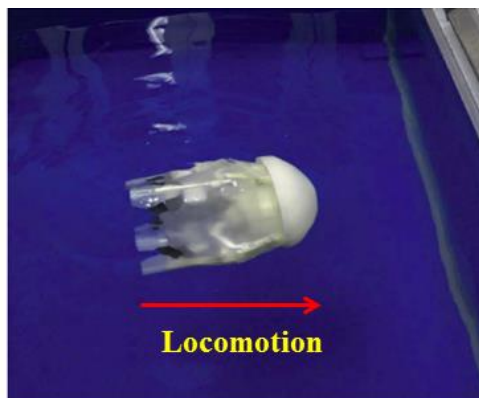


Fig. 2.9: Self-propelled jellyfish robot based on six-bar linkage mechanisms [34]

Li et al., [35] developed a novel self-propelled jellyfish robot (Fig. 2.10) based on mechanical structure drive and barycenter adjustment mechanism. The robotic jellyfish consists of a bell-shaped rigid head, a tubbish main cavity and four six- bar linkage mechanisms. The main cavity is made of white nylon and is hollow molding for placing the barycenter adjustment mechanism, circuit board, communication module, battery and sensors. Through the design and actualization of the noumenon and circuit of the robotic jellyfish, a jellyfish-like robot which is able to locomote in the water. The average swimming speed can attain 100 mm/s

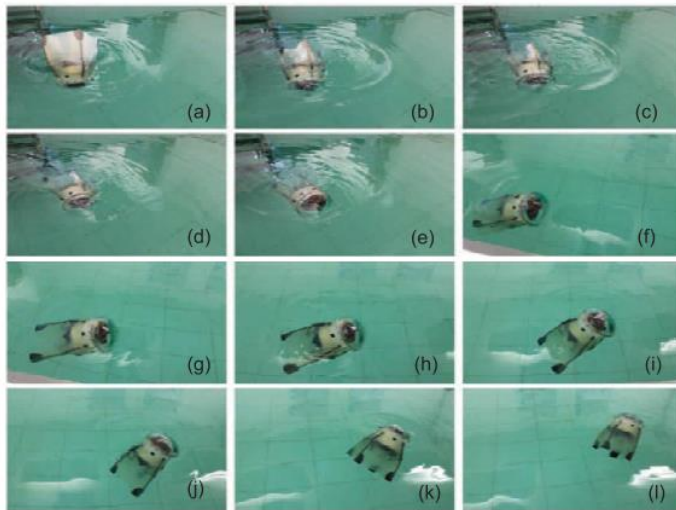


Fig. 2.10: Jellyfish robot based on barycenter adjustment mechanism [35]

Godaba et al., [36] developed a jellyfish robot (Fig.2.11) which consists of a bell, an air chamber, and a membrane of a dielectric elastomer. The dielectric elastomer actuator is subject to voltage, the membrane expands, the volume of air increases, and the buoyant force acting on the robot increases. Meanwhile, water is ejected from the robotic body, which can induce propulsion to make the robot move up. The preliminary studies show that the soft robot based on dielectric elastomer technology can move effectively in water.

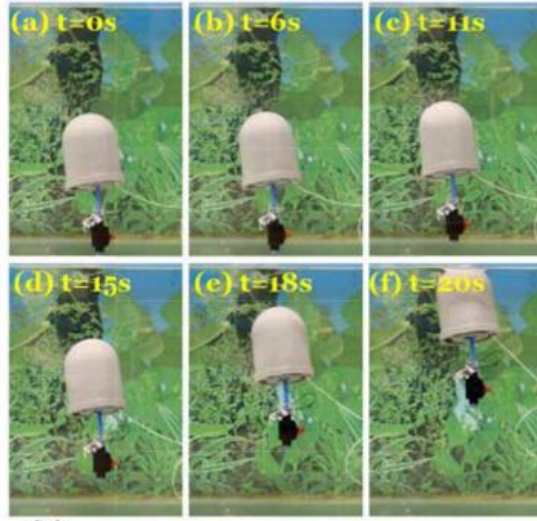


Fig. 2.11: dielectric elastomer based jellyfish [36]

Frame et al., [37] developed soft robotic jellyfish (Fig.2.12) were constructed with hydraulic network actuators. Each tentacle had a common channel extending radially outward from the center of the robot; four of these channels were connected on each side of the jellyfish so that four tentacles could be driven by a single impeller pump. Two pumps were used to actuate the eight tentacles, four tentacles per pump. The silicon rubber material is used for tentacle actuators. Results showed that the material composition of the actuators significantly impacted the measured force produced by the jellyfish. The greatest forces were measured with a half-stroke amplitude at 0.8 Hz and a tentacle actuator-flap material Shore hardness composition of 30–30. The jellyfish was able to swim through orifices more narrow than the nominal diameter of the robot and demonstrated the ability to swim directionally by temporally offsetting tentacle actuation strokes on opposing sides of the robot. The jellyfish robots were tested in the ocean and have the potential to monitor and explore delicate ecosystems without inadvertently damaging them.



Fig. 2.12: Hydraulic based soft robotic jellyfish [37]

Tadesse et al., [38] developed a hydrogen-fuel-powered artificial jellyfish (Fig.2.13) bell segment. The fuel-powered muscle comprises platinum nanoparticles wrapped with multi-wall carbon nanotube (MWCNT) sheets on the surface of NiTi alloy. A mixture of oxygen and hydrogen produces an exothermic reaction as it encounters the platinum. This reaction activates the NiTi based SMA. MWCNT serves as a support for the platinum powder and enhances the heat transfer due to the high thermal conductivity between the composite and the SMA. The optimum cyclic condition was found to be 0.1 Hz.

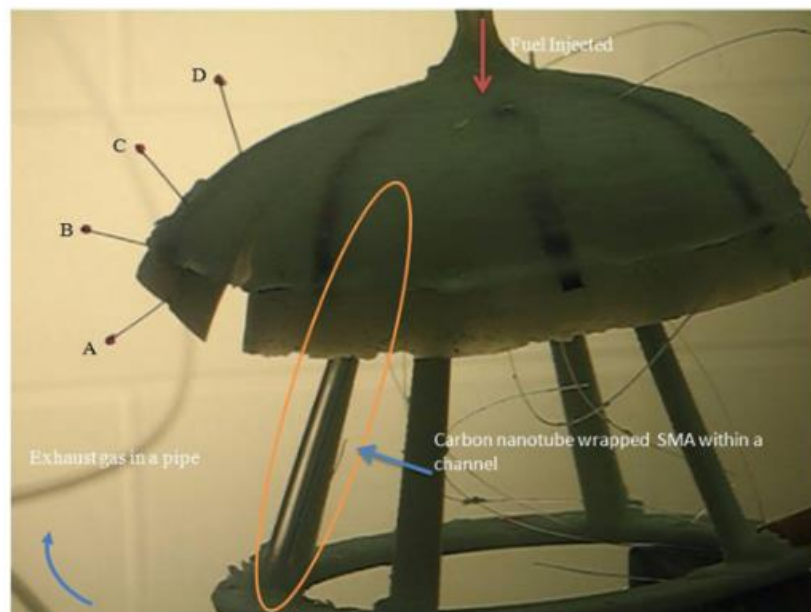


Fig. 2.13: Hydrogen fuel powered jellyfish robot [38]

2.3. Smart materials based fish robots

Cho et al., [39] developed a body caudal fin propulsion system (Fig.2.14) using SMA spring actuators mounted on a multi-segmented, flexure based frame. It is composed of a flexure-jointed composite fiber spine that will be covered with a PDMS skin. The motion of the caudal fin is driven by the SMA springs attached on either side of each flexure. These are actuated in succession to create a traveling waveform. Flexures, electrical wiring, and actuator attachment points are all embedded into a copper-laminated polyimide foil patterned with copper traces, solder pads and other features needed for assembly. Undulatory motion is created by using a sequence of mode shapes. This scheme of using a single actuator to create a single mode that coordinates multiple joint angles further simplifies the design and control of the device. Varying each segment length to fit the natural motion of a fish as well as increasing total number of segments will result in a more realistic tail motion.

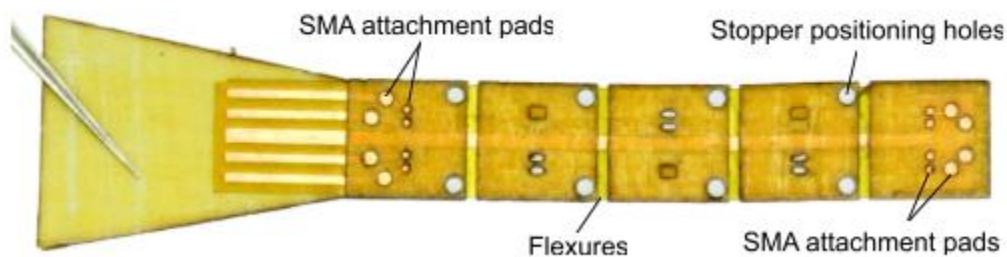


Fig. 2.14: SMA spring based flexural caudal fin propulsion [39]

Wang et al., [40] developed a wireless micro robot manta ray using a pair of SMA wire actuated oscillating pectoral fins (Fig.2.15). Micro robot manta ray prototype consisting of a body, two pectoral fins and a tail. A pair of SMA wire sets lay on the two surfaces of elastic substrate and they are covered by the skins of each face. The elastic substrate of biomimetic

fin is made of polyvinyl chloride (PVC) sheet. The forward swimming and the turning swimming capabilities of the micro robot manta ray were investigated. A maximum swimming speed of 57 mm/s was achieved and the maximum amplitude was 40 mm.

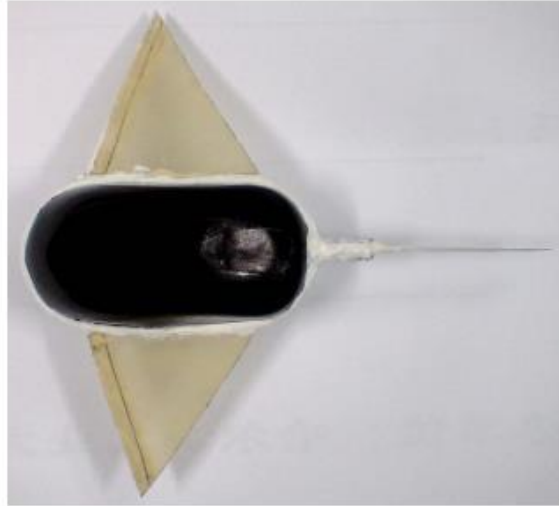


Fig. 2.15: SMA wire based micro manta ray fish robot [40]

Ravalli et al., [41] developed a bio-inspired fish robot (Fig.2.16) capable of swimming according to the directives sent in form of chemical messengers. The robot prototype adopts SMAs actuators that bend a continuous flexible structure (the backbone of the robot fish), made of polycarbonate. Electro-chemical sensors platform was used in order to detect the presence of the hydrogen ions as chemical messengers and transform them into electronic signals to be used in robot control. The proof-of-concept for the development of multi-sensors fish robot as future core technology that can be used for water quality parameters providing early information on environmental change and improving farm management decisions, fish well-being and consequently sustainable productivity.

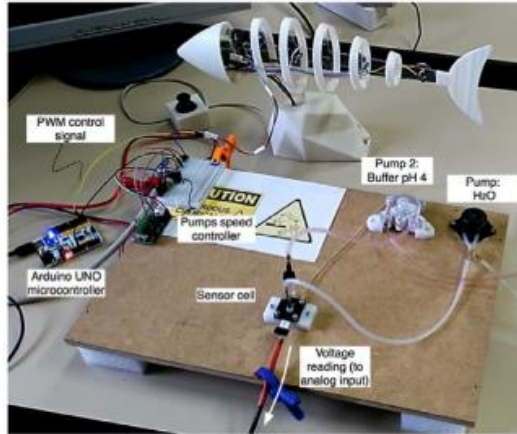


Fig. 2.16: Robotic fish based on chemical sensors [41]

Wang et al., [42] developed a micro-robot fish propelled by a biomimetic fin (Fig.2.17). The embedded SMA wire actuated biomimetic fin imitates the structure of squid/cuttlefish fin. The biomimetic fin consists of elastic substrate, skin, and transverse muscle-like SMA wires. The propulsor consists of a biomimetic fin (active component) and a caudal fin (passive component). The caudal fin is used to enlarge the control surface and the thrust. Elastic energy storage and exchange mechanism is incorporated during the bending of biomimetic fin. Initial experiments of bending were conducted to verify the concept of biomimetic fin. Thermal analysis is also applied to find proper actuation strategy. Then a radio frequency controlled micro-robot fish prototype was built based on the biomimetic fin. With different tail fin, subcarangiform and carangiform-like swimming movements were realized. Experimental results show that the micro-robot fish can swim forward and turn with a biomimetic fin. A maximum swimming speed of 112 mm/s and a minimum turning radius of 136 mm were obtained.

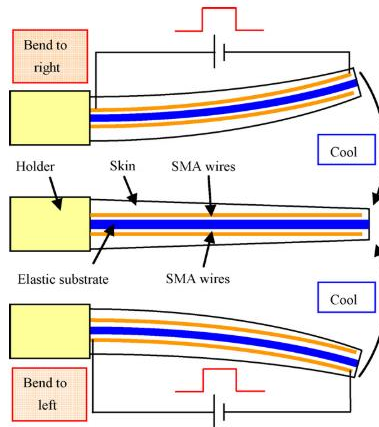


Fig. 2.17: SMA wire actuated biomimetic fin [42]

Guo et al., [43] proposed a new prototype model of an underwater micro robot in water using Ionic Conducting Polymer Film (ICPF) actuator (Fig.2.18). ICPF actuator is made from the film of perfluorosulfonic acid polymer chemically plated on it's both sides with platinum. It is known as an ion exchange membrane. It is a kind of high polymer gel actuator, works only in water and in wet condition. It has two tails with a fin driven respectively, a body posture adjuster and a buoyancy adjuster. Characteristic of the micro robot is measured by changing the frequency of input voltage from 0.1 Hz to 5 Hz in water and the amplitude from 0.5 V to 10 V. The structure of the underwater micro robot was effective and the swimming speed can be controlled by changing the frequency of the applied voltage.

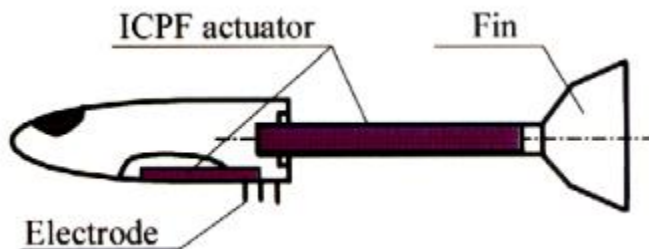


Fig. 2.18: ICPF actuated underwater microrobot [43]

McGovern et al., [44] studied a method for directly measuring the thrust

force generated by a polypyrrole (PPy) powered tail fin (Fig.2.19). It produced the highest thrust forces to propel an untethered robot fish and the straight line speeds were determined as a function of voltage input frequency. The thrust force generated by PPy tri-layer actuators attached to a fish-like tail fin was investigated. The study provides valuable insight into the means for tailoring polymer actuator performance to achieve maximum fish swimming speeds.

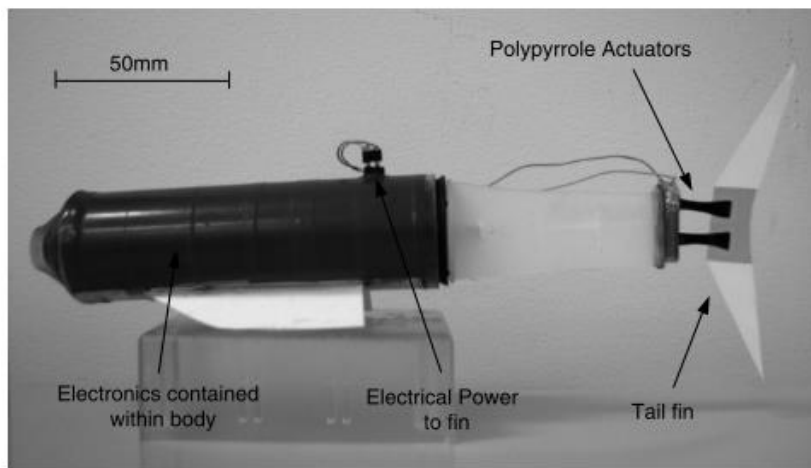


Fig. 2.19: Polypyrrole actuator based robot fish [44]

Rossi et al., [45] presented bio-inspired locomotion for underwater robots. They have investigated the new kinds of robots capable of changing their shape in a continuous way, and the use of smart materials as alternative actuation systems. The novelty of using a bendable structure as the backbone of the fish based on the V-shape configuration of antagonistic SMA-based actuation muscles has great potential for improving the maneuverability of the fish while performing the aforementioned swim patterns underwater. The prototype (Fig.2.20) used SMA actuators to bend a continuous flexible structure, representing the backbone of the robot fish, made of polycarbonate. An additional structure of ribs is employed to support the silicon-based skin that provides the three-dimensional shape of the robot.

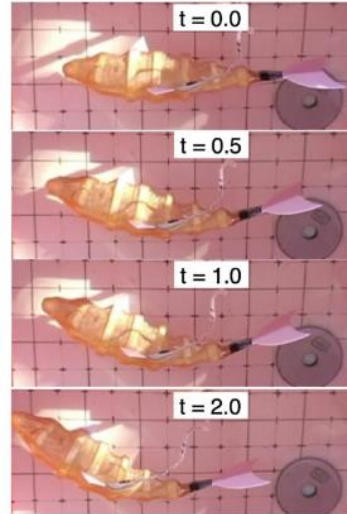


Fig. 2.20: SMA based bendable structured robotic fish [45]

Shintake et al., [46] developed a fish type DEA-based soft biomimetic underwater robot (Fig.2.21) that swims by BCF propulsion. The robot exhibited swimming motion resembling real fish, as also quantitatively estimated by the Strouhal number. The results suggest that the high potential of DEA-based underwater robots relies on BCF propulsion and the applicability of the proposed design and fabrication methods. The peak swimming speed of the robot was 37.2 mm/s (0.25 body length/s) at 0.75 Hz.

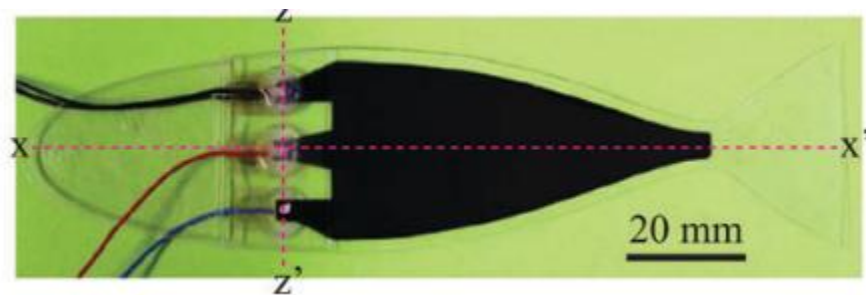


Fig. 2.21: DEA based soft robotic fish [46]

Zhang et al., [47] developed a bioinspired flexible SMA pectoral fin (Fig.2.22). A SMA fin ray capable of two-DoFs oscillation is introduced and a lightweight bioinspired pectoral fin formed by the SMA fin rays is

developed. The proposed bioinspired pectoral fin possesses several major features as those by the biological fin. For example, the fin could provide the motion with four basic patterns: relaxation, expanding, bending, and undulation. It is obvious that the bioinspired pectoral fin is still a very simplified version of the biological pectoral fin. A live pectoral fin of a Koi Carp has 15 fin rays, whereas only five fin rays are used in the bioinspired fin.

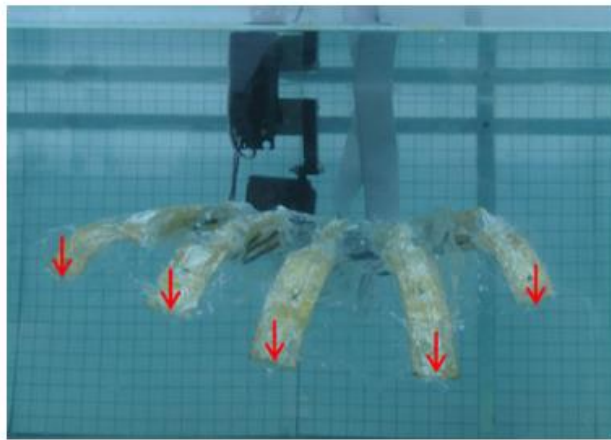


Fig. 2.22: Flexible SMA pectoral fin [47]

2.4. Smart materials based thin film robots

Smart materials have been used widely in the development of micro devices for better performance. Piezoelectric, SMA and Ionic Polymer Composites (IPMC) are the smart materials which have garnered interest in the development of micro actuators [48-55]. Among these smart materials, SMA possesses highest energy density and benefits the development of high performance micro actuators [56-61]. SMA can recover large strain and suitable for the development of micro devices like micro pump, micro wrapper/micro grippers, micro cantilever, micro thermostat array and micro mirror [62-69]. SMA thin film has potential applications as sensors/actuators in the fields of biomedical, MEMS, automobile, military and aerospace [70]. SMA thin film is considered as a

core technology for actuation of MEMS devices, where large force and stroke are essential in conditions of low duty cycles or intermittent operation and in extreme environment such as radioactive, space, biological and corrosive conditions [71]. However, the hysteresis, response speed and precise motion control are the potential problems associated with SMA thin film towards the development of micro devices.

Usually, the SMA will be deposited as a thin film on rigid substrate and peeled off after deposition to enable the development of devices [72-76]. Subsequently, shape training of the SMA thin film is required before deployment. However, the free standing SMA thin films are unable to produce large actuation force. To eliminate the tedious training and to increase the force produced, the SMA thin film was deposited over the flexible substrates. Ishida et al. have developed a SMA NiTi bimorph and investigated its suitability as micro flapper [77-80]. Kotnur et al. have studied the influence of various parameters on NiTi SMA bimorph [81-82]. Copper based shape memory alloys exhibits a low hysteresis along with interesting electrical and thermal properties. Our research group has developed different types of NiTi and Cu based SMA bimorph actuators using thermal and electron beam evaporation technique [83-88]. Detailed investigations on the influence of substrate temperature on the materials properties and performance of actuators have been reported. Furthermore, the actuation behavior of the developed copper based SMA bimorph has been evaluated towards its suitability as micro flappers in aerial robots. The attractive actuation behavior coupled with better life cycle characteristics has enabled the copper based bimorph as the viable candidate for micro mechatronics and micro robotics applications. It was found that the addition of Mn to CuAlNi thin film has significantly increased the life cycles of the SMA bimorph. Because of the higher life cycles, it can be used as an efficient MEMS actuator with larger load capacity for developing low cost and efficient micro and soft robots. Bimorph is a composite structure with films grown over the passive

flexible substrate. The bimorph provides two way shape memory effect without any additional bias mechanism.

Ishida et al., developed Ti-Ni-Cu SMA thin films were sputter-deposited on heated polyimide substrates. The (Ni,Cu) rich Ti-Ni-Cu films deposited at a substrate temperature of 543 K were found to possess a high martensitic transformation temperature above room temperature over a wide range of Cu content from 7 to 23 at%, which allows stable production of actuators that operate at room temperature. Additional deposition of a Cu film onto the Ti-Ni-Cu films facilitated the soldering of wires onto the actuators and also decreased the power consumption and response time of the actuator. The force of a polyimide/Ti-Ni-Cu SMA actuator could be increased merely by increasing the thickness of the polyimide film. An actuator composed of a 125 μm thick polyimide film and an 8 μm thick TiNiCu film was able to lift a 13.5 g weight and proposed an SMA thin film based dragon fly.

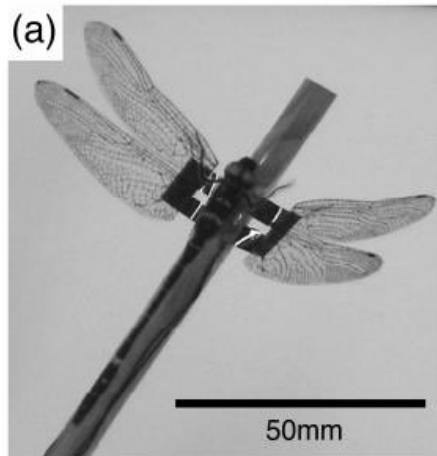


Fig. 2.23: SMA thin film based dragonfly [24]

Abuzaiter et al., developed a novel structure of a shape-memory-alloy (SMA) micromanipulator with gripping mechanism. A featured integration of multiple SMA bimorph microactuators has been utilized to form a micromanipulator with three degrees of freedom. The design consists of two links (SMA sheets) and a gripper at the end of the second

joint. The displacement of each actuator is controlled by a heating circuit that generates a pulse-width modulation signal. The SMA micromanipulator is able to move in the x- and y-axis by 7.1 mm and 5.2 mm, respectively, resulting in a maximum displacement of 8.9 mm. The micro-gripper has a maximum opening gap between its fingers of 1.15 mm. The maximum actuation force generated by the x- and y-axis was around 100 mN and 130 mN, respectively. The developed micromanipulator has been successfully used to move a small object.

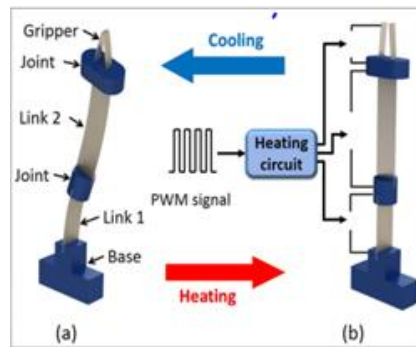


Fig. 2.24: SMA based micro manipulator [89]

Huang et al., developed a micro gripper using NiTi shape memory alloy thin sheet. The shape memory alloy was trained to be with two way shape memory by re-heat treatment. The micro gripper was actuated by electrical current directly.

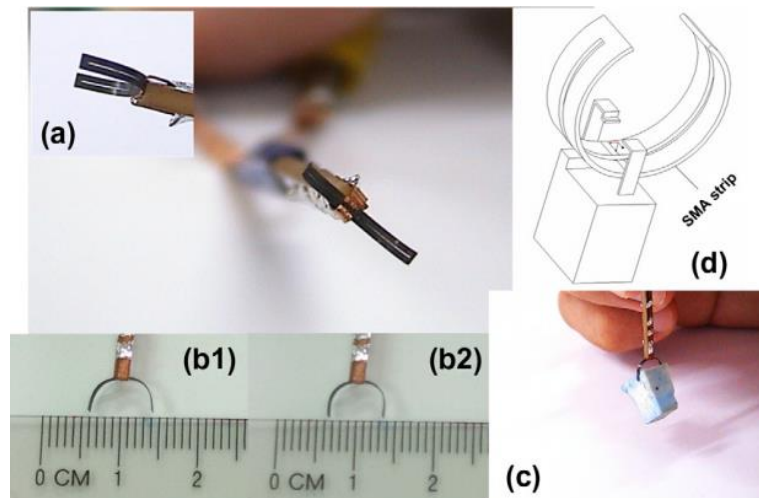


Fig. 2.25: NiTi thin sheet based micro gripper [90]

Fu et al., developed a TiNi/diamond-like-carbon (DLC) microcage has been designed for biological applications. The structure is composed of a top layer of TiNi film and a bottom layer of highly compressively stressed DLC for upward bending once released from the substrate. The fingers of the microcage quickly close through the shape memory effect once the temperature reaches the austenite start transformation point to execute the gripping action

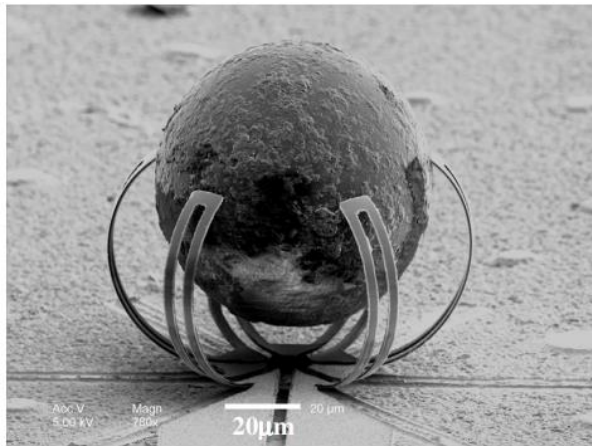


Fig. 2.26: TiNi/DLC based microcage [15]

Many researchers have studied the shape recovery behavior i.e. thermally induced actuation using different heating methodologies, such as Joule heating, hot fluidic actuation, laser actuation, electromagnetic heating and RF electromagnetic actuation. In general, Joule heating of SMA element is simple and used widely but requires electrical insulation from other metal/conductive components for safety and better energy efficiency.

2.5 Inference and research gap from the literature-Summary

The bio-inspired soft robots have been developed with various soft material actuator technologies. There is a need for alternative actuators to mimic the natural living species. In the literature, different soft actuator technologies such as SMA, Pneumatic, IPMC, hydraulic, ICPF and dielectric elastomer have been used to developed bio-inspired soft robotics

for different applications with different soft and flexible materials. However there are limitation associated with scaling and utilizing the mentioned technologies with respect to different designs. Notably SMA can be made into any convenient forms and the technology can be fitted to variety of robotic designs. We have proposed several bio-inspired robots based on the different SMA forms like spring, wire and bimorph.

2.6 Detailed Objectives and Methodology

As mentioned in the first chapter, the thesis aims to employ the different forms of SMA structures like spring, wire and bimorph towards the development of soft robots.

- The feasibility of SMA based spring structure in the development of bio-inspired soft robots
 - ✓ To evaluate the electrical actuation parameters of SMA spring using finite element analysis.
 - ✓ To study the thermo-mechanical behaviour of SMA spring using electrical actuation.
 - ✓ To study the Laser actuation parameters of SMA spring towards non-contact actuation applications.
 - ✓ Development of soft mesh worm prototype and evaluation of its bending characteristics through both electrical and laser based actuation.
 - ✓ Kinematic and dynamic analysis of SMA spring based robotic fish propulsion mechanism.
 - ✓ Development of SMA spring based robotic fish prototype and its performance evaluation.
 - ✓ Investigation on the caudal fin displacement and force produced during undulation.
- The feasibility of SMA based bimorph structure in the development of bio-inspired soft robots

- ✓ To evaluate the electrical actuation parameters of SMA bimorph using finite element analysis.
- ✓ To study the thermo-mechanical behaviour and electrical actuation characteristics of SMA bimorph with varying voltage and load.
- ✓ Displacement control study on SMA bimorph toward the development of SMA bimorph based soft robot.
- ✓ Development of SMA bimorph based soft robot prototype and its performance evaluation.
- The feasibility of SMA wire embedded composite structure in the development of bio-inspired soft robots
 - ✓ To evaluate the electrical actuation parameters of SMA wire embedded soft composite using finite element analysis.
 - ✓ To study the electrical actuation characteristics of SMA wire embedded soft composite.
 - ✓ To study the pre straining effect of the SMA wire and life cycle analysis on the soft composite
 - ✓ Development of SMA wire embedded soft composite based soft robotic gripper prototype and its performance evaluation.
 - ✓ To model the deflection and hydrodynamic study of the SMA wire based polyimide soft structure
 - ✓ To analyse the tip displacement of the SMA wire based polyimide soft structure with varying wire diameter.
 - ✓ To study the electrical actuation characteristics of SMA wire based polyimide soft structure.

- ✓ Development of SMA wire/polyimide soft structure based soft robotic jellyfish prototype and its performance evaluation.

The work methodology is shown in Fig.2.27.

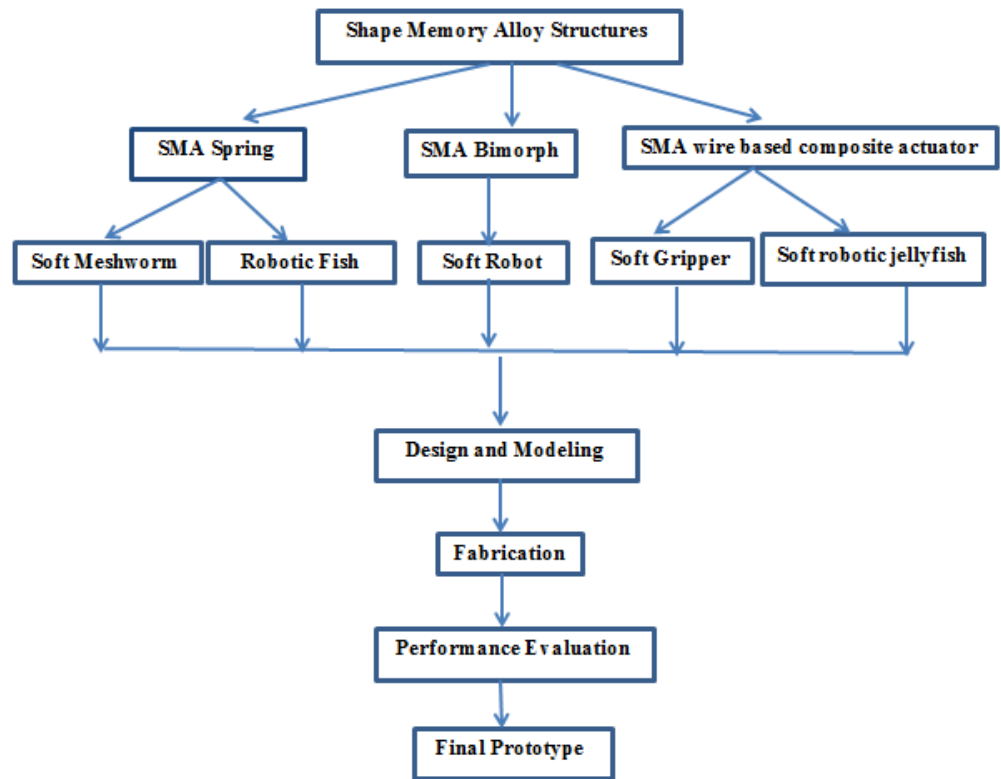


Fig. 2.27: Methodology

Chapter 3

Investigations on SMA spring based actuators towards bio-inspired soft meshworm

3.1 Introduction

In this chapter, SMA spring based meshworm and robotic fish has been developed and its various performance characteristics have been investigated. Initially the modelling of SMA spring has been performed to evaluate the temperature generation during joule heating. Then the mechanisms, fabrication, and performance evaluation of meshworm and robotic fish have been investigated in detail. In addition, a novel laser based technique for the actuation of SMA spring has been demonstrated. Interestingly, the non-contact laser based technique has been employed for evaluating the bending characteristics of meshworm. The final prototypes of the robots have been demonstrated.

3.2 Bio-inspired softworm robot

A biomimetic soft worm robot has been developed using soft mesh structured polyethylene terephthalate (PET) thermoplastic driven by SMA springs. The fabrication of bio-inspired robots, selection of the material, investigations on the locomotion behaviour, bending characteristics, and underwater experiments are discussed. The bending behaviour of the robot for achieving steering in peristaltic and bending for two anchor locomotion has been investigated in detail. A flex sensor is attached to the soft worm to measure the bending/steering angle. An open loop control approach is adopted for the study of soft worm's bending actions. The movement of the soft

worm robot has been probed towards imitating the bending action of two anchor crawling locomotion with kapton polyamide legs.

Many researchers have studied the SMA based soft robotic inchworm structures and their linear locomotion. However, the curvilinear motion of inchworm is not reported to the best of the author's knowledge. In this chapter, a detailed study of soft worm robot bending in peristaltic and two anchor based locomotion is done with the aid of the SMA spring actuator. An attempt has been made to completely understand the bending characteristics of braided mesh structure as a function of various actuation parameters such as current, duty cycle, and bending angles. The detailed procedure on fabrication and the shape setting of braided mesh tube structure have been discussed. In addition, the thermal characteristics of the SMA actuator have been studied via both experiments and numerical simulation. The mesh like braided tube is used for imitating the bending action of two anchor locomotion with the help of kapton polyamide as prolegs.

3.3 Modeling of SMA spring

The thermal characteristic of nitinol SMA spring was studied to understand the behaviour of the spring during heating. The heating of the spring is performed through Joule heating. The thermal simulation was carried out in COMSOL to find the safe working temperature of the SMA spring. Fig. 3.1 (a, b) shows the temperature distribution of SMA spring at the end of the heating and cooling cycle respectively.

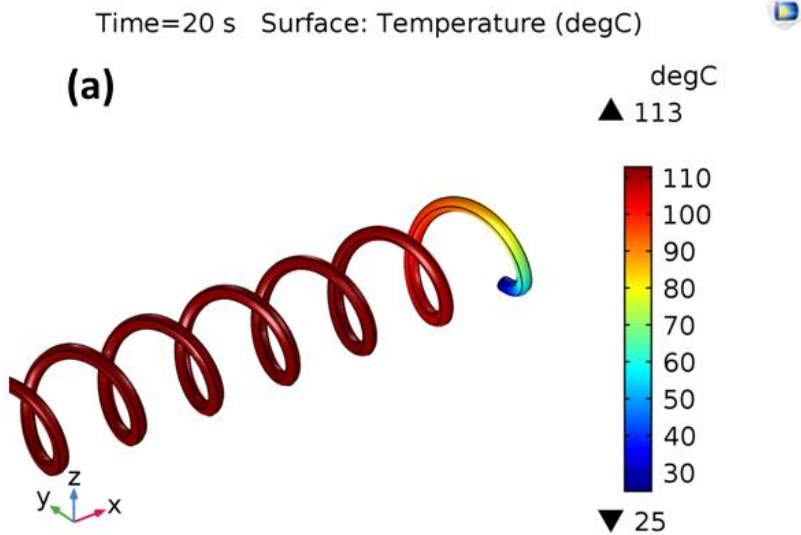


Fig. 3.1: a) Temperature distribution of nitinol SMA spring in COMSOL at the end of the heating cycle

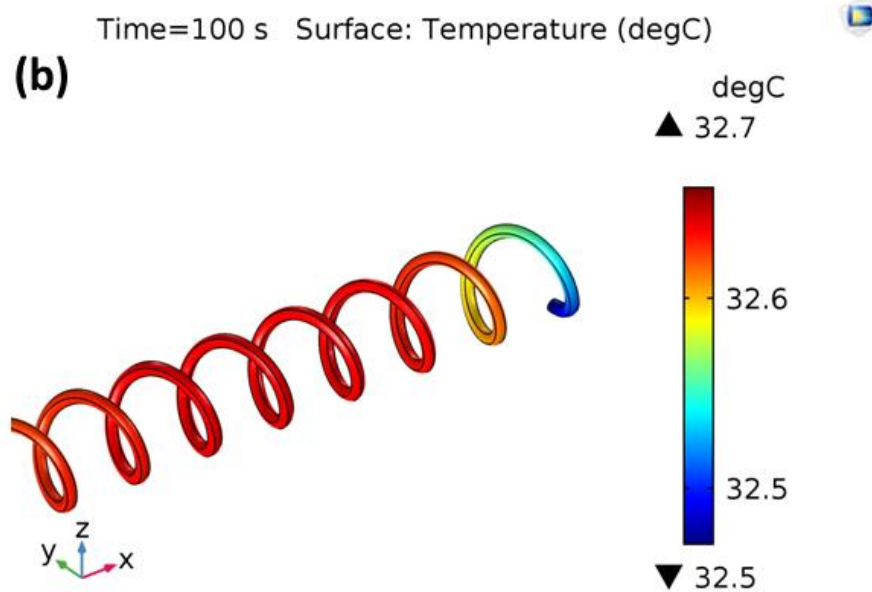


Fig. 3.1: b) Temperature distribution of nitinol SMA spring in COMSOL at the end of the cooling cycle

The properties of the NiTi wire used for the COMSOL simulations are obtained from the literature. The required properties for the COMSOL simulation considered for simulation are shown in Table 3.1.

Table.3.1: Spring simulation properties

Property	Value
Density	6450 Kg/m ³
Specific heat	550 J/Kg °C
Thermal conductivity	12 W/mK
Electrical resistivity	6 x 10 ⁵ Ωm
Solid length	13.86 mm
Number of turns	18
Wire diameter	0.77 mm
Coil diameter	5.69 mm

The thermal simulation shows that the SMA phase transformation from detwinned martensite to high temperature austenite occurred in 20 s in which the temperature reached the saturation point of 113 °C. The spring took 80 s to cool and reach the twinned martensite phase i.e., room temperature. During experimentation, the SMA spring was heated for less than 20 s to maintain the threshold limit. Fig. 3.2 shows the heating and cooling curve obtained from the COMSOL simulation data. The results from the simulations have been validated using a thermography camera (FLIR ONE thermal imager). Thermography camera was used to capture the temperature changes experienced in the SMA spring through Joule heating. Table 3.2 shows the comparison of the simulation temperature data with the experimental thermography. The data are in good agreement with each other.

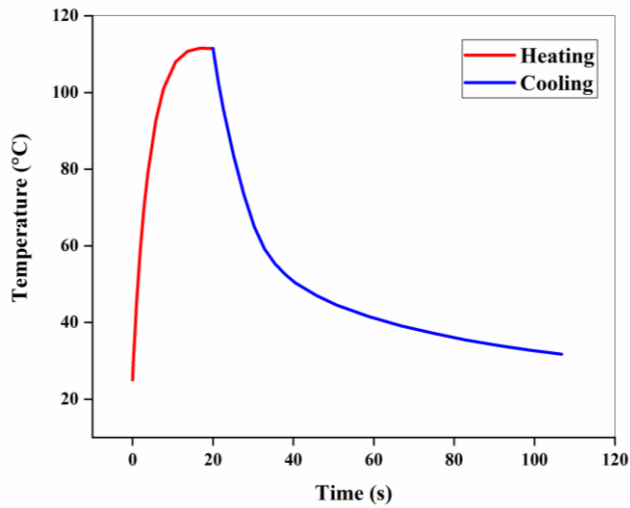
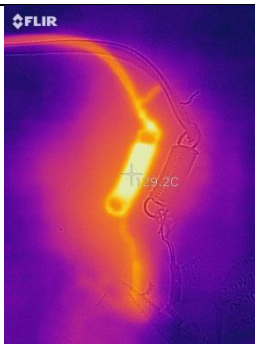
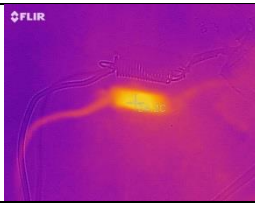


Fig. 3.2: Heating and Cooling curve of nitinol SMA spring

Table.3.2: Validation of SMA spring with thermography

	Simulation value (°C)	Thermography value (°C)	Thermography image
1	113 at 20 s	129.2	
2	32.7 at 100 s	34.6	

3.4 Inchworm Mechanism

Peristaltic locomotion mechanism: In earthworms, coelom in each septum contains a liquid that acts as fluidic transmission between the radial and longitudinal directions. With this fluid-filled divided cavity, worm segment deformation follows a constant volume constraint. Thus, the hydrostatic skeleton can be considered as an elastic tube that

varies its radius and length subject to a fixed internal volume. The hydrostatic bodies of earthworms are controlled by the antagonism between radial (or circular) and longitudinal muscles.

Two anchor locomotion mechanism: Generally, inchworm locomotion is based on the anchor motion crawling principle, where the legs are used for anchoring. To complete a stride, an inchworm needs to use its front and back legs sequentially for anchoring body contraction and elongation. The design of the anchor-motion mechanism of the robot is very important for producing inchworm-like locomotion. Fig. 3.3 shows the crawling mechanism of an inch worm.

SMA spring mechanism: In the closed coil configuration at room temperature, the SMA spring has twinned martensite crystal structure. The closed coil position is the trained shape of the SMA spring. The minimum and maximum stress required to deform the material is called de-twinning start stress (σ_s) and de-twinning finish stress (σ_f) respectively. Due to the applied load, de-twinning of the martensite structure takes place. This de-twinning induces a deformation coaxially on the spring up to a certain limit depending on the load. The joule heating converts the electrical energy into heat due to which the SMA spring reaches austenite phase temperature and returns to its original closed coil position as shown in Fig. 3.4.

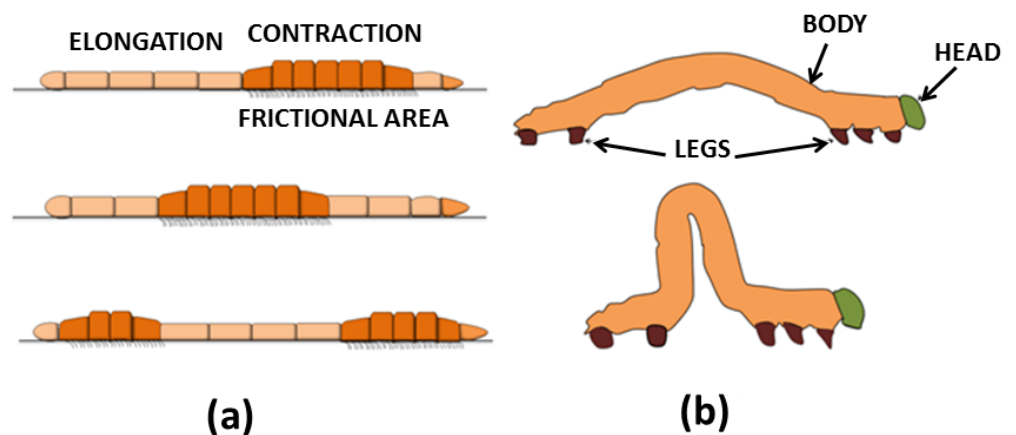


Fig. 3.3: a) Peristaltic crawling b) Two anchor crawling

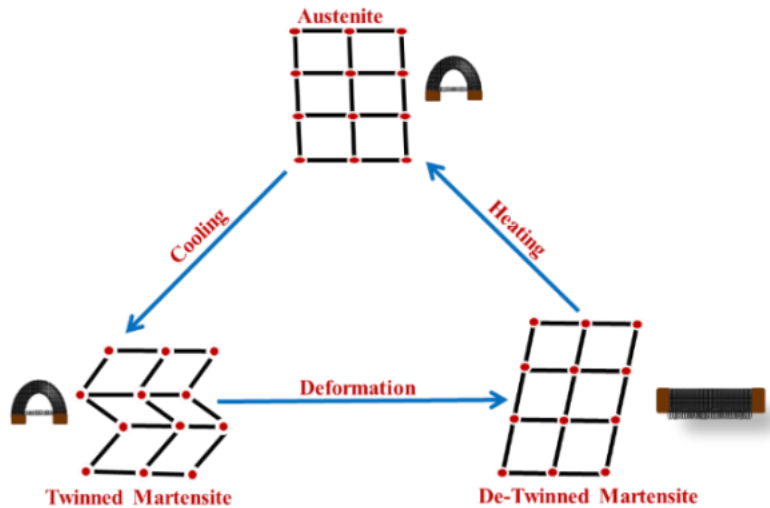


Fig. 3.4: Soft meshworm structure at different SMA phases

3.5 Fabrication of softworm skeletal structure

PET belongs to the group of materials known as thermoplastic polymers. The application of heat leads to the softening and deformation of thermoplastics. Initially, a steel rod of diameter 44 mm was inserted into the PET mesh structure. The PET structure with the rod was kept inside a muffle furnace. It was heated at 215° for 20 minutes and cooled through natural convection. The process was repeated until the soft mesh tube structure was obtained. The diameter of the soft mesh tube structure was measured to be 46 mm upon removal of the rod. The process of fabricating the softworm skeletal structure is shown in Fig. 3.5.

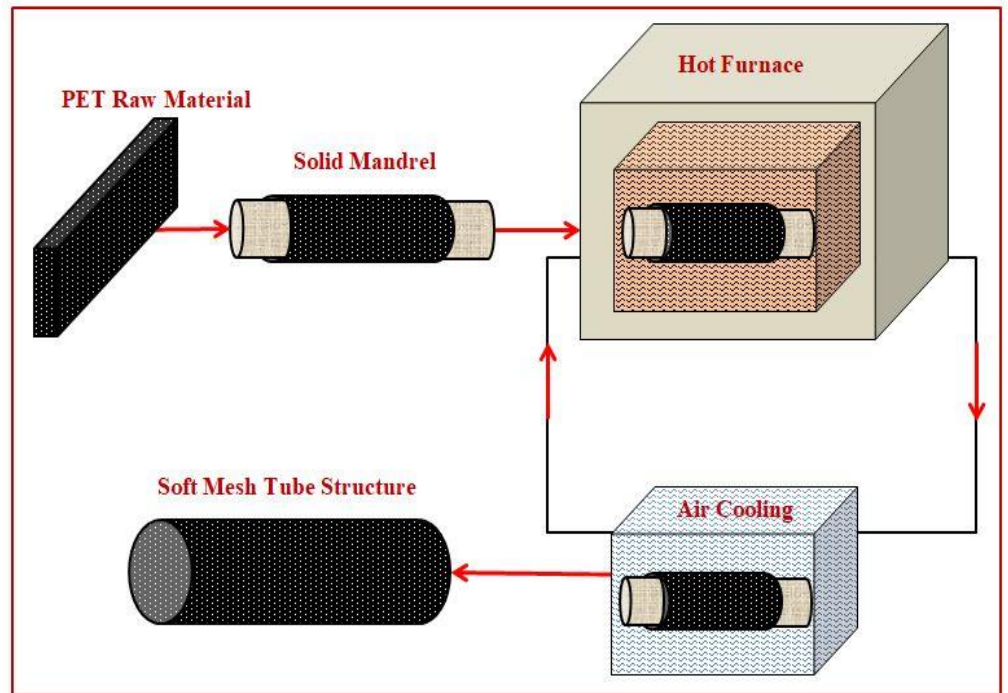


Fig. 3.5: Fabrication process of softworm skeletal structure

The length of the soft worm structure was 90 mm. The commercially available nitinol SMA spring has been used with the worm structure to create the peristaltic, two anchor locomotion, and bending.

PET possesses good flexibility with high strength to weight ratio. Initially, the load bearing capacity of PET material before and after the fabrication process was studied using a universal tensile testing machine. The parameters used for testing are given in the below table.

3.3.

Table.3.3: Tensile test parameters

Parameter	Raw PET	Annealed PET
Type of test	Tension	Tension
Thickness	1.50 mm	1.50 mm
Width	40 mm	25 mm
UTL	4.679 kN	2.539 kN
Displacement at UTL	30.410 mm	36.838 mm
Test Speed	1 mm/min	1 mm/min

Fig. 3.6 shows the load vs. displacement curve for PET material before and after the heat treatment process. Before annealing, the PET was able to undergo deformation up to 6 mm at 0.082 kN load, which corresponds to 0.0375 % strain indicating the elastic limit (region A). After the annealing process, the elastic limit (region B) was enhanced and it can take up to 0.114 kN with deformation up to 11 mm (0.0706 % strain). The increased elastic limit of the material will be suitable for the softworm structure.

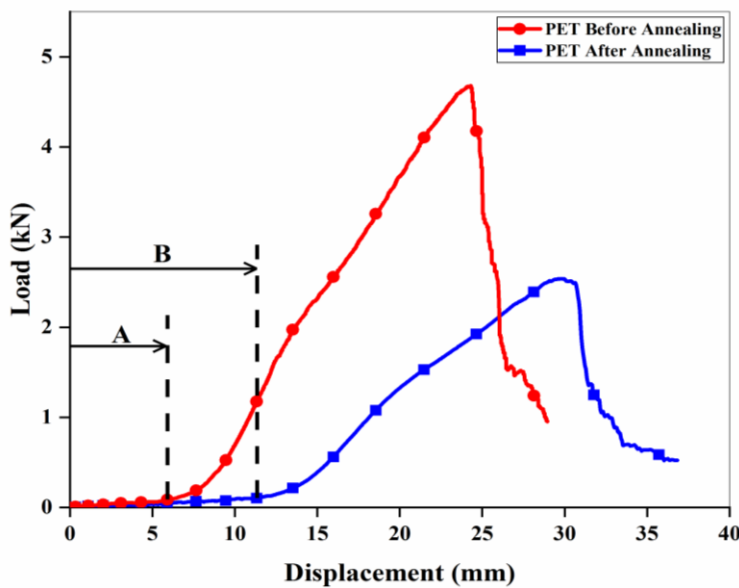


Fig. 3.6: Behaviour of PET under loading condition

3.6 Experimental Setup

DC power supply (Instek PSB-2400L) was used to heat the SMA spring via Joule heating. A laser displacement sensor (LDS – Panasonic Laser Sensor HL-G108-A-C5) was used to measure the displacement of the softworm. A Data Acquisition system (NI C-DAQ 9174 with NI 9219, 4 channel, 24 bit, Universal Analog Input Module) was used to collect the displacement data from LDS. PC with Lab VIEW 2017 is connected with the DAQ to record and process data. A flex sensor (FS – L – 0055 – 255 – ST) has been attached to the inner surface of the softworm and connected to arduino UNO to acquire the bending angle of the softworm. The Arduino UNO was connected to the relay used to switch between actuation (heating) and cooling

cycles. The change in resistance of the flex sensor is mapped to the corresponding change in the bending angle. The resolution of the flex sensor is 1° . The block diagram and the image of the sensor and control setup are shown in the Fig. 3.7.

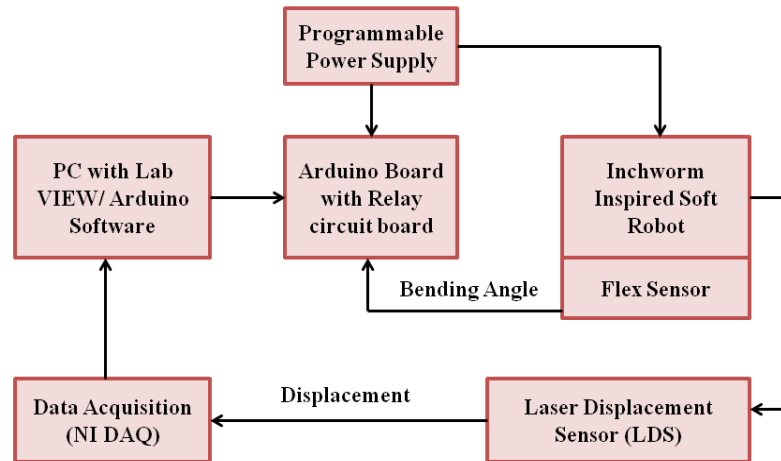


Fig. 3.7 a) Block diagram of Softworm setup

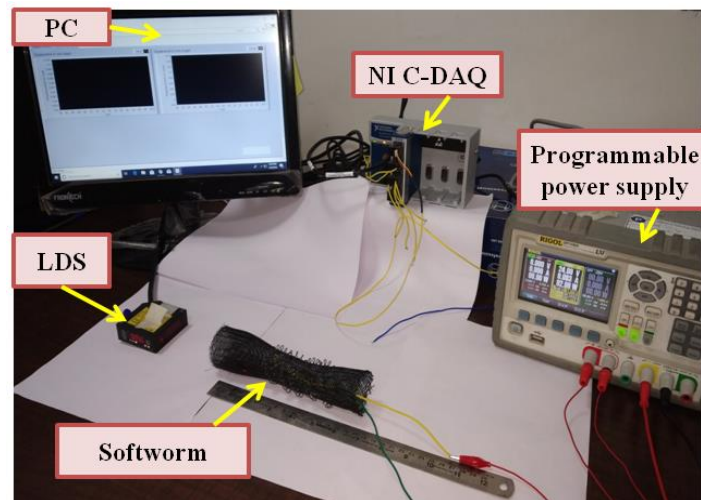


Fig. 3.7 b) Softworm experimentation

3.7 Performance Evaluation

3.7.1 Peristaltic crawling

The SMA NiTi (Nitinol) spring, supplied by Dynalloy Inc. was used for studies. In order to achieve the peristaltic crawling, different SMA spring configurations were employed. Here, the configuration represents the way by which the spring is affixed to the PET mesh

structure. In the first configuration, three SMA springs were attached longitudinally with the softworm structure as shown in Fig. 3.8 (a). Then the bending behaviour of soft worm structure in left, right, and upward directions were studied.

In the second configuration, a nitinol SMA spring was wound around the soft worm structure to achieve linear motion as shown in Fig. 3.8 (b).

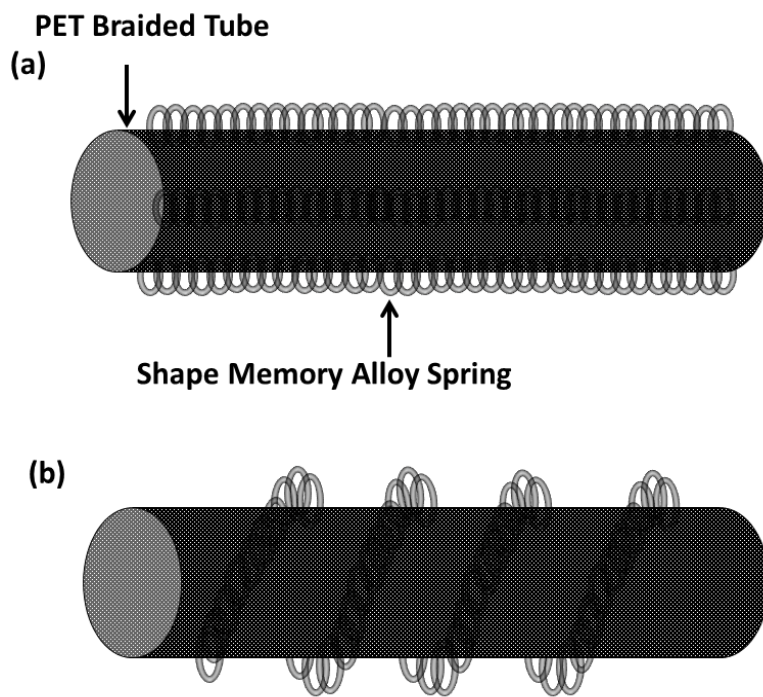


Fig. 3.8: SMA spring a) in line with Soft worm for bending analysis
b)wound around

The SMA spring was electrically divided into 4 segments where each segment is actuated sequentially to create the locomotion. Lastly, a radial muscle configuration has been developed with the combination of SMA spring and a bias spring to provide structural stability as shown in Fig. 3.9.

In this configuration, the Ni-Ti spring is placed coaxially inside the bias spring. The bias spring has a larger diameter than the Ni-Ti spring. The diameter of the bias spring is 10 mm. The reason behind choosing larger diameter bias spring than the NiTi spring is to have a pull force

that can induce strain. With the induced strain, the NiTi spring changes from twinned martensite to detwinned martensite.

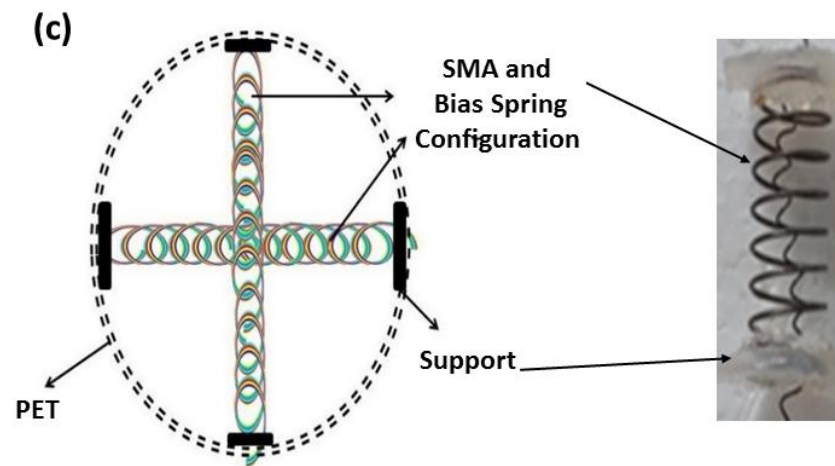


Fig. 3.8: c) Radial muscle configuration

3.7.2 Two anchor crawling

For two anchor crawling, a leg like support made of kapton polyamide has been attached circularly at both the ends of a soft mesh tube. The advantage of using kapton polyimide as a leg of two-anchor structure is that with polyimide (PI) film can obtain a low friction force with the ground. To create the bending action, a nitinol SMA spring has been attached with the soft mesh structure as shown in Fig. (a). The SMA spring was actuated with 3 V and 2.5 A input supply, which created a bent structure as shown in Fig. 3.9.

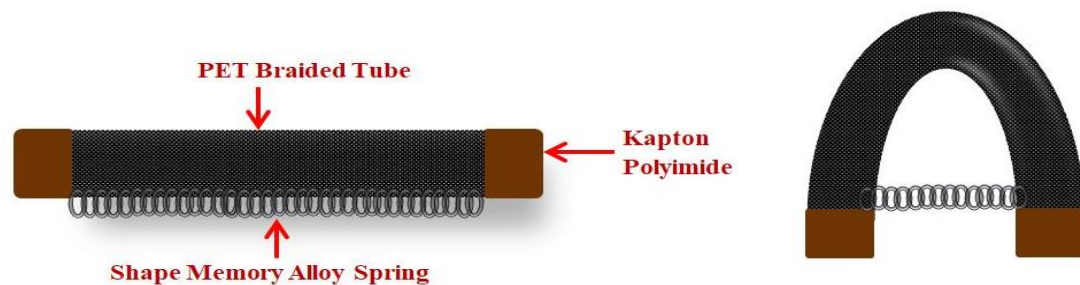


Fig. 3.9: Schematic of proposed two anchor crawling structure and bending

The initial position is the stretched out deformed (Detwinned martensite) shape. While heating the spring moves to the compressed shape (Austenite). In the Longitudinal configuration where the spring is placed outside and along with the mesh structures, the spring is placed off the axis of the mesh structure. So, when the spring is heated, the compression in the spring is converted to bending of the mesh structure due to the off axis placement of the SMA spring.

An open loop control approach is adopted for the study of bending characteristics. A fixed heating (actuation time) and cooling time of 2 s are applied to SMA spring in each segment to achieve peristaltic locomotion for both the proposed configurations.

A thermal camera (FLIR ONE) is used to capture the heat distribution in the spring during the heating cycle. To study the behavior of the spring under various loads, the spring was loaded 1.5 N, 2.5 N, and 3.5 N with an experimental set up as shown in Fig.3.10.

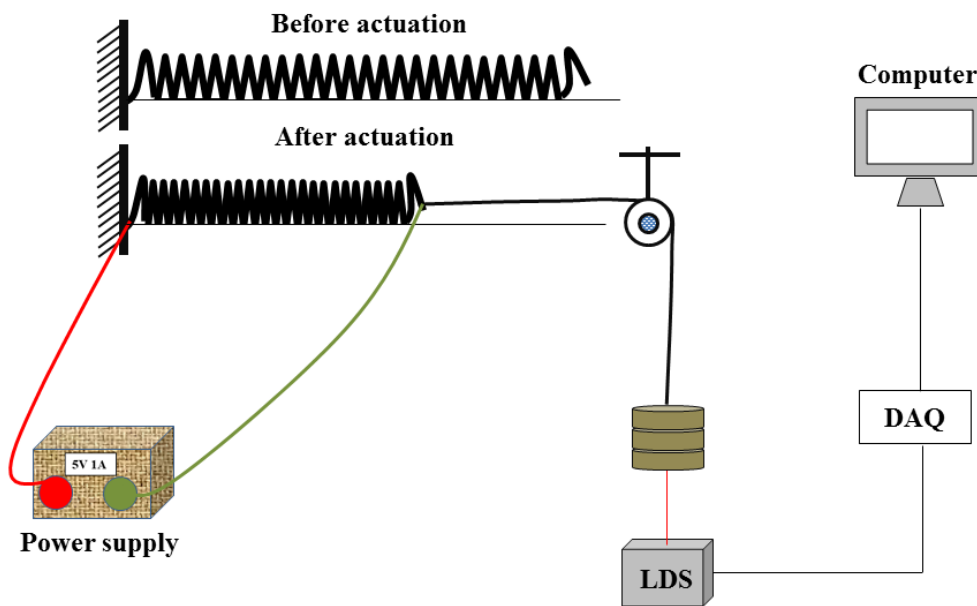


Fig. 3.10: Schematic of load Analysis

The heating and cooling period of the spring was studied under various loads. Fig. 3.11 (a-c) shows the maximum displacement plot for varying voltages and loads. The preliminary load study of the SMA

spring and tensile test of the mesh structure has been done to analyze the coupled effect of the SMA actuation and structure. The bending can be easily achieved in mesh structure because of its flexible nature with the SMA actuation. The recovery to its initial position is possible with the mesh structure which can create a pull force to induce strain in the SMA spring. The induced strain will change the SMA spring from martensite to detwinned martensite.

One end of the spring is fixed and the free end has been loaded. The load used here acts as a bias force which de-twin the martensite structure once it cools down to its martensite temperature. Since the load is antagonistic in nature, increasing the load produces higher displacement as compared to lesser loads. At 1.5 N, a maximum displacement of 3.9 mm was observed. The loads 2.5 N and 3.5 N have produced a maximum displacement of 7.54 mm and 9.17 mm respectively. At higher voltage, there is a minor increase in recovery due to the reduction in inter-coil gap. Table 3.4 shows the increase in recovery of the spring for various voltages, and load. It is observed that the increase in voltage has decreased the heating time required to reach the maximum displacement. At 2 V, 3 V, and 4 V the total heating time (i.e., time taken to reach saturation) was observed to be 20 s, 15 s, and 10 s respectively. At 3 V and 4 V, the maximum current of 2.5 A and 3 A has been drawn by the spring respectively. The actuation speed of the spring was moderate and controllable at 3 V/2.5 A. Therefore, the electrical process parameter of 3 V/2.5 A has been used for further investigations.

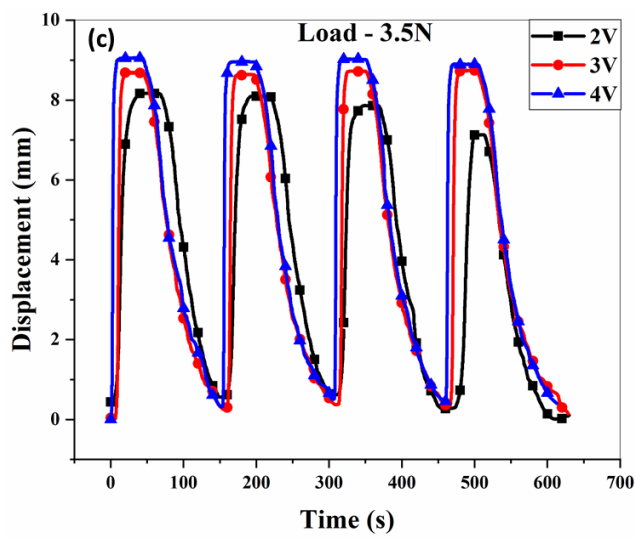
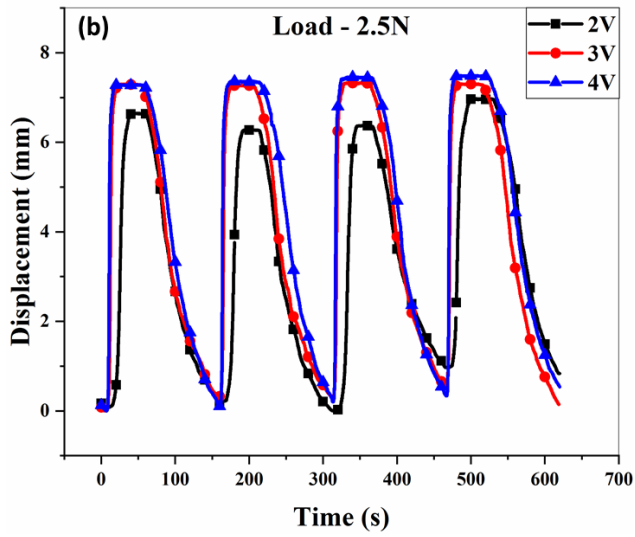
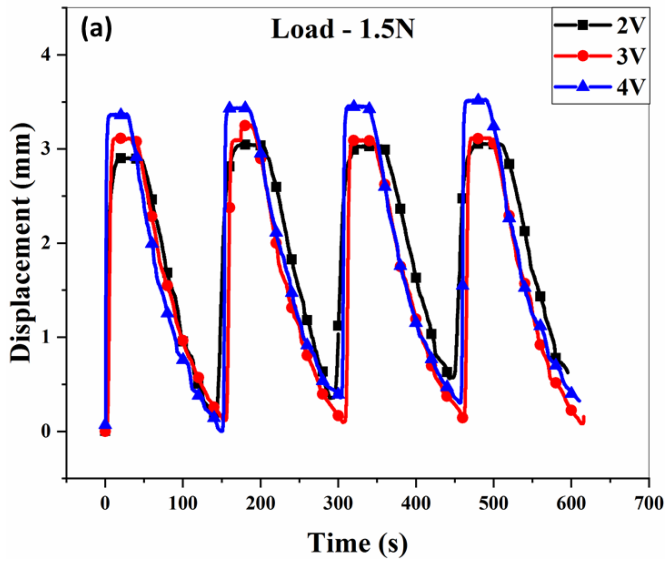


Fig. 3.11: Behavior of SMA spring with bias loads a) 1.5 N, b) 2.5 N and c) 3.5 N

Table.3.4: Spring recovery under various loading conditions.

	2 V	3 V	4 V
1.5 N	3.08 mm	6.96 mm	8.17 mm
2.5 N	3.28 mm	7.36 mm	8.75 mm
3.5 N	3.93 mm	7.54 mm	9.17 mm

Experiments were conducted to measure the bending angle and displacement of the softworm. Electrical current is applied sequentially to actuate the SMA spring and get the locomotion. The maximum bending deflection for the softworm structure was studied using a SMA spring of diameter 5 mm and a solid length of 16.5 mm. The ends of the spring were attached longitudinally at two ends of the softworm body; the arrangement by which the longitudinal compression of the spring is converted into the bending of the mesh body structure (Fig. 3.12).

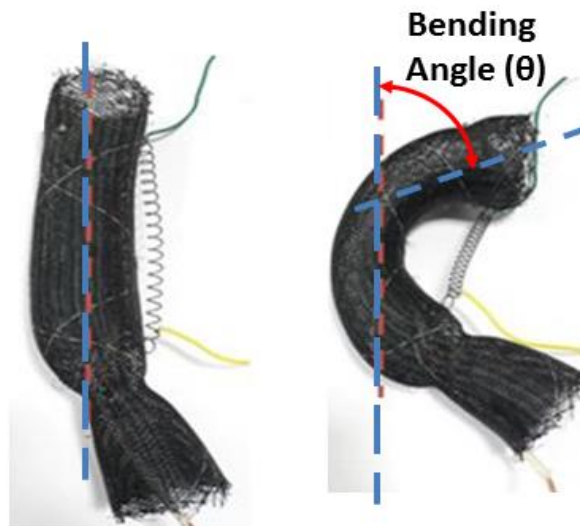


Fig. 3.12: Bending angle during actuation of SMA spring

The spring was actuated for different bending angles of the structure and the results are shown in Fig. 3.13.

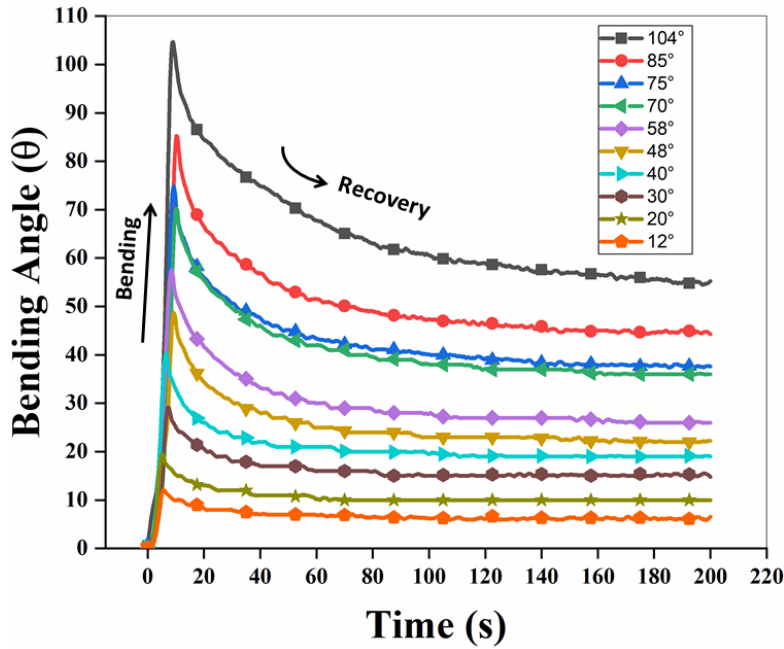


Fig. 3.13: Comparison of various bending angles and their recovery

The initial position is the stretched out deformed (detwinned martensite) shape. Upon electrical stimulation, the spring moves to the compressed shape (austenite) due to heating. In the Longitudinal configuration where the spring is placed outside and along with the mesh structures, the spring is placed off the axis of the mesh structure. So, when the spring is heated, the compression in the spring is converted to bending of the mesh structure due to the off axis placement of the SMA spring. When the spring was completely actuated until it reached the solid length, a maximum bending angle of 104° was observed.

The maximum bending angle and recovery percentage of the soft worm were also investigated. The recovery is due to the compression and tension created on the inner and outer surface of the bent soft mesh structure. During the study, the spring was allowed to cool by natural convection. The heating and cooling cycles lasted up to 200 s. The percentage recovery at various bending angles is shown in Fig. 3.14.

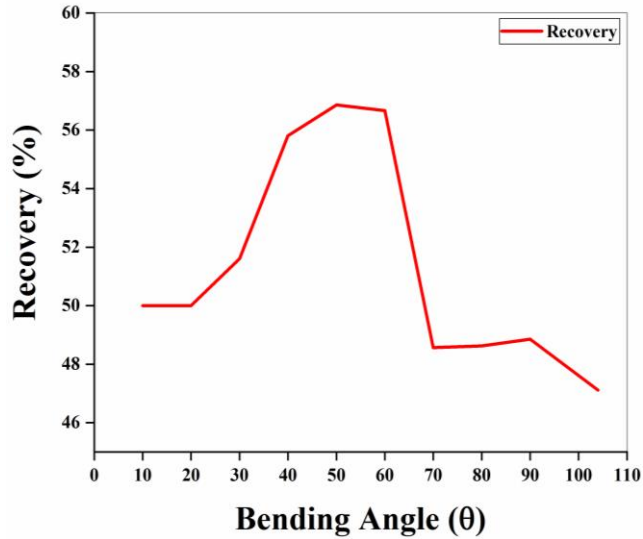


Fig. 3.14: Percentage recovery for various bending angles

It can be seen that maximum recovery of about 57 % was obtained between 50° to 60°. Based on recovery percentage, the optimal bending angle is between 50° to 60°. However, bending angles lesser than 50° can also be used for steering the softworm. Then the effect of duty cycle on the maximum bending angle was studied. The total cycle time was fixed at 60 s and the duty cycle was varied from 2 % in steps of 2. The results of various duty cycles at 2.5 A are shown in Fig. 3.15.

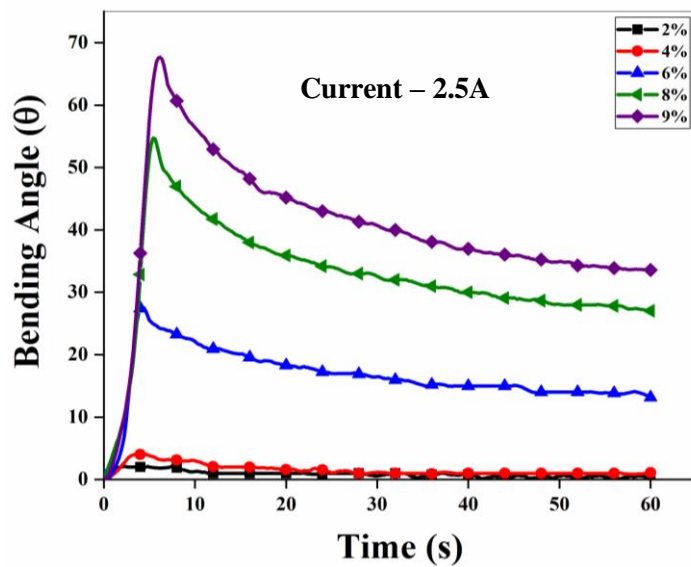


Fig. 3.15: Variation of bending angles with change in duty cycle

The increase in the duty cycle has increased the bending of the structure. The bending angle has increased substantially at 6% duty cycle due to the spring reaching its austenite start temperature 48 °C (3.6 s of heating time). At 8% duty cycle (4.8 s heating time), the bending has reached almost 55°. Therefore it can be concluded that, 8% duty cycle is optimal for steering application. The snapshots from the thermal camera for 4 %, 6 %, and 8 % are shown in Fig. 3.16 a, b, and c respectively.

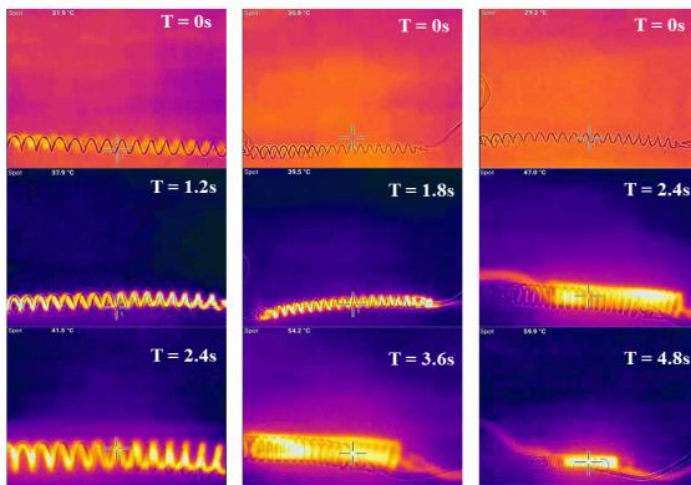


Fig. 3.16: Thermographic images for Duty cycle a) 4 % b) 6% c) 8 %

In order to determine the optimal current to achieve a 50° bending angle at 8 % duty cycle, the current was varied in steps of 0.5 A and the corresponding bending angles were evaluated. The bending observed at various values of current is shown in Fig. 3.17. At 0.5 and 1 A, there was no bending observed in the structure, since the time is not sufficient to provide the required temperature suitable for actuation i.e. austenite temperature is not reached.

It can be observed that a maximum deflection of 97° at 3 A which is not desirable. The curve shows that a current of 2.5 A to 2.6 A is suitable to achieve an optimal bending angle of 50° to 60° at 8 % duty cycle. The bending behavior of peristaltic locomotion in left, right, and upward directions is plotted in Fig. 3.18.

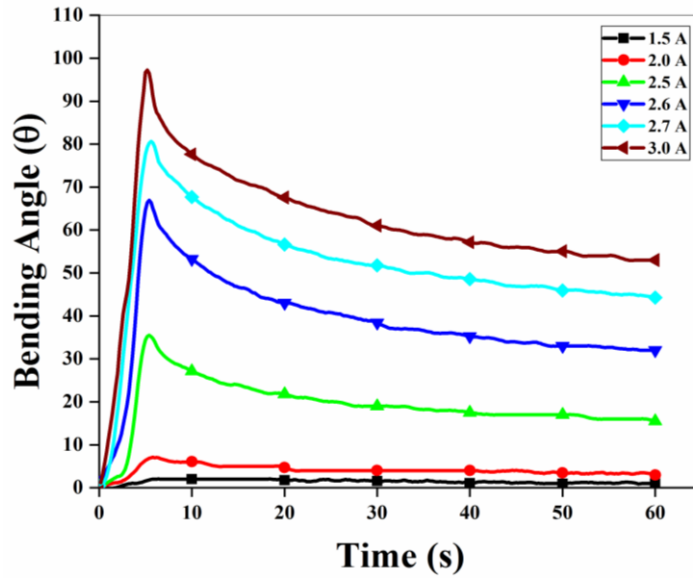


Fig. 3.17: Variation in bending angles for different current

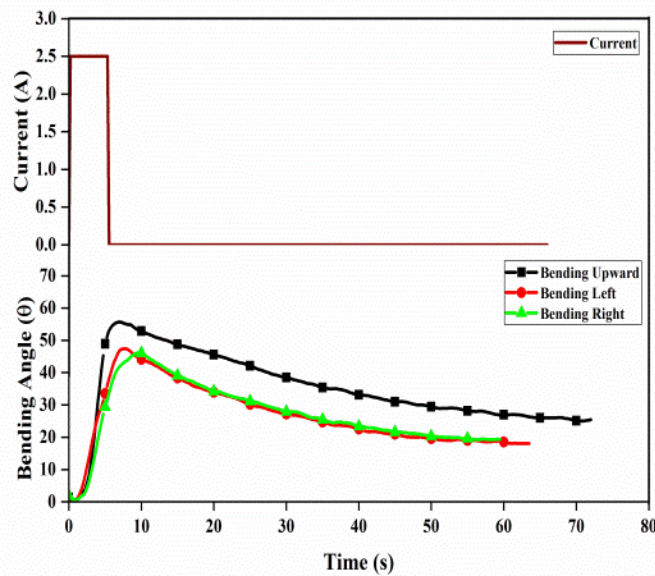


Fig. 3.18: Bending curve for peristaltic crawling

The maximum bending angle achieved in upward, left and right directions are 57° , 48° , and 48° respectively with 8% duty cycle and 2.5 A. During heating of SMA spring the maximum bending angles in upward, left and right direction was reached in 5 s. After bending, the SMA spring is allowed to cool through natural convection for 60 s. The recovery is achieved due to the forces induced in the structure during bending of the flexible PET structure and also due to the increase in the elastic limit as noticed during the tensile test after

forming the skeletal structure. The bending behaviour for two anchor crawling in downward bending is plotted in Fig. 3.19.

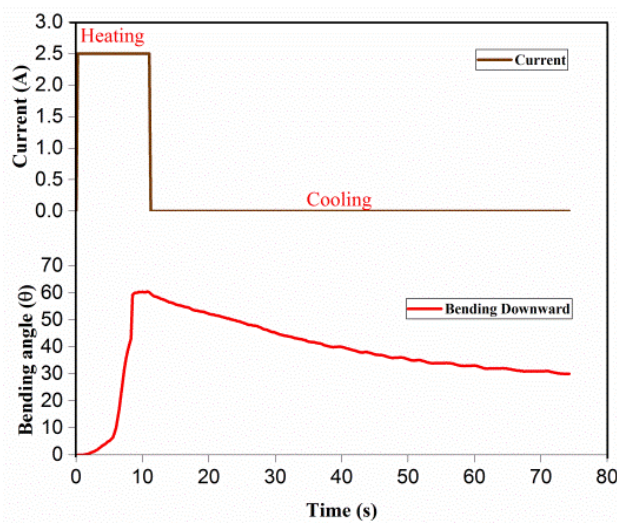


Fig. 3.19: Bending curve for two anchor crawling

The downward bending action resembles the two anchor crawling motion exhibited by inchworm. The kapton polyamide is used as a leg for the two anchor structure which supports the overall structure during downward bending. The advantage of using kapton polyimide as a leg of two-anchor structure is that with polyimide (PI) film can obtain a low friction force with the ground. The maximum bending angle achieved in the downward direction is 60° . During heating of SMA spring, the maximum bending angles in the downward direction was reached in 10 s. After bending, the soft worm structure is cooled to room temperature by convection. The structure has not completely recovered its initial position. It took approximately 70 to 75 s to reach 30° . Miniature suction cups may be used in place of polyimide legs at both the ends of mesh structure for better grip while crawling. Fig. 3.20 (a-f) shows the locomotion gait for the peristaltic type and bending action of two anchor crawling type respectively. The upward bending action can be used to manoeuvre over obstacles and the same was investigated towards stair climbing application with a single stair kind of arrangement of 5 mm height as shown in Fig. 3.20 (a-c). It was

observed that the downward bending action can be used for creating two anchor inchworm structure and motion.

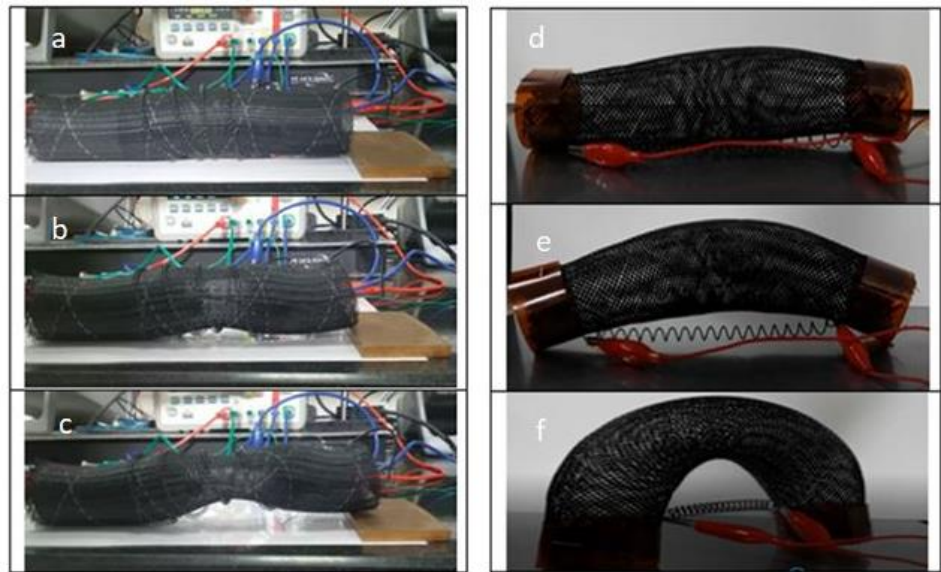


Fig. 3.20: a-c) Peristaltic locomotion to maneuver a single stair arrangement

d-f) Bending action of Two anchor locomotion

Fig. 3.21 (a-c) shows the soft worm bending at various times. Fig. 3.21d shows the flex sensor arrangement inside the mesh worm structure. Fig. shows the meshworm with the flex sensor.

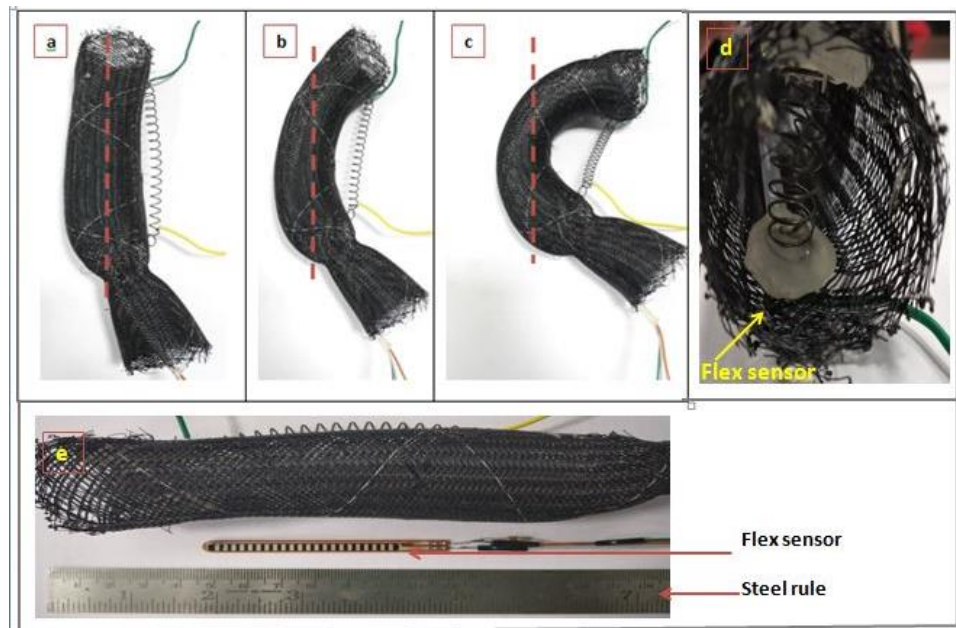


Fig. 3.21: Flex sensor arrangement

SMA's have found a number of applications in different areas. Hence, the easy and inexpensive estimation of reliability of critical components, subassemblies, or systems using SMA's is an area of importance. There are many specific reasons for looking at component data to estimate the overall system reliability. One of the most important is that in many situations it is easier and less expensive to test components/subsystems rather than the entire system. Various methods are available for the displacement measurement and life cycle analysis of the SMA spring based on inductance, resistance, load change, etc. The SMA spring reliability analysis for electrical actuation is done with simple interferometry technique. Based on the study, the SMA spring shows good performance with minimal displacement drift even after 5000 cycles.

3.8 Non-Contact actuation of Soft Meshworm

In this section, the non-contact actuation of SMA spring has been carried out using a continuous laser setup. In case of higher thickness and lengthy SMA actuators, the current required for actuation will be very high due to large inherent material resistance. Besides, SMA's cannot be permanently bonded to the electrical circuits hence there is a possibility of contact failure during operation. Though fluidic actuation is economical, there is a risk of working fluid interaction and it may lead to corrosion or erosion of the SMA element. These demerits in the contact actuation methods insist on developing a laser irradiation based actuation methodology. The actuation characteristics with varying laser power and load have been studied. After understanding the laser actuation of SMA spring, it has been applied to the bending of softworm structures. The non-contact method facilitates long distant actuation, improves actuator mobility and degree of freedom over other actuation methods. The absence of intricate connections eliminates additional element requirements such as wiring and connectors, thus favouring MEMS applications. Places where human intrusion will be

difficult or hazardous such as nuclear reactors, space explorations, mining, etc.

A novel scanning technique for the contactless laser actuation of SMA spring has been performed. The influence of laser power on the actuation behavior is studied in detail for the power ranges from 5 W to 50 W with bias loads of 1.5 N, 2.5 N, and 3.5 N. In order to deform the spring for actuation studies, one end of the closed coil spring is fixed and the free end is loaded with 1.5N, 2.5N, and 3.5N loads. Fig. 3.22 shows the experimental setup for the laser actuation of the SMA. Due to the applied load, deformation begins in the spring at an ambient temperature of 17°C. Once the deformation due to the applied load terminates, the laser is switched on. Continuous Laser from the fiber laser source, doped with Yb active gain medium of 1064 nm wavelength was used for irradiating the SMA spring. To move this laser beam along the length of the spring for heat distribution, a dynamic reflecting mirrors or simply galvo mirrors are used. Laser guided through the optical fiber cable is made to fall on the galvo mirrors. These mirrors reflect the line beam of width 0.2 mm over the top surface and scan throughout the length of the spring with a scanning speed of 30 mm/s.

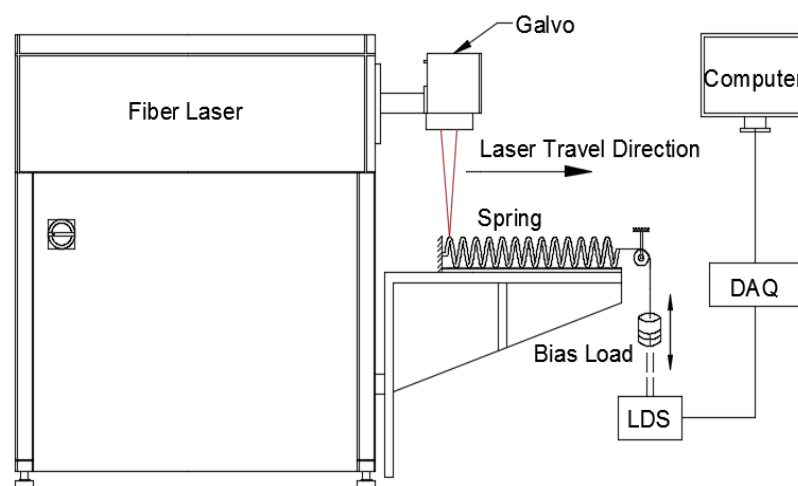


Fig. 3.22: Experimental setup for the laser actuation of SMA spring

The Laser beam scanning provides the necessary heat to attain the phase transformation temperature. Due to the shape memory effect, the spring displaces and returns to its initial closed coil position. A LDS of the 2.5 μ m resolution was used to measure the change in length of the spring. Data from the LDS is acquired in the data acquisition system (Agilent 34790A) interfaced with the computer for further data processing. Once the actuation was accomplished, the spring was allowed to cool to room temperature. During cooling, the applied bias load brings the spring to the initial deformed state. After complete cooling, the next actuation cycle was carried out. The laser power, irradiated in steps of 5 from 5W to 50W, was used for the investigation of the thermo-mechanical behavior of the SMA spring.

Initial trial experiments were conducted to choose the optimum bias load required for the thermo-mechanical actuation study of the SMA spring. A sufficiently observable deformation was obtained only with a load of 1.5 N, hence a minimum load of 1.5 N was chosen. When 4.5 N of bias load was used, the spring was subjected to failure i.e. bifurcation of the spring happens during laser irradiation. Hence a minimum and maximum bias load of 1.5 N and 3.5 N were chosen respectively for obtaining the required two-way shape memory behaviour of the SMA spring.

For experiments, the laser power from 5W to a maximum capacity of the available laser system 50W was used. It was observed that the minimum laser powers of 5W and 10W were not sufficient enough to actuate the spring. The Laser irradiation at these powers was unable to increase the temperature of the spring beyond A_s , even after many passes and hence no actuation was observed. Here, the increase in the number of passes has no effect on temperature, since the heat absorbed by the spring may equal the heat given out to the surrounding. Hence the powers 5W and 10W were neglected for the actuation studies, considering the inefficiency during any practical application.

Then the Laser beam of power 15W was scanned over the top surface of the spring. Initially, for 2 passes, there was no actuation observed in the spring as illustrated in Fig. 3.23. In order to initiate the actuation, at least 3 passes were required for a power of 15 W. Fig. shows the number of passes required to initiate the actuation in the spring with respect to the increase in laser power. The gradual step observed from the graph conveys that the increase in Laser power has decreased the minimum number of passes required for actuation. It is also evident that above 30 W, no initial passes were required to initiate the actuation as As can be reached in the first pass itself. Fig.3.24 shows the schematic of the typical heating and cooling curve during ON and OFF of Laser irradiation.

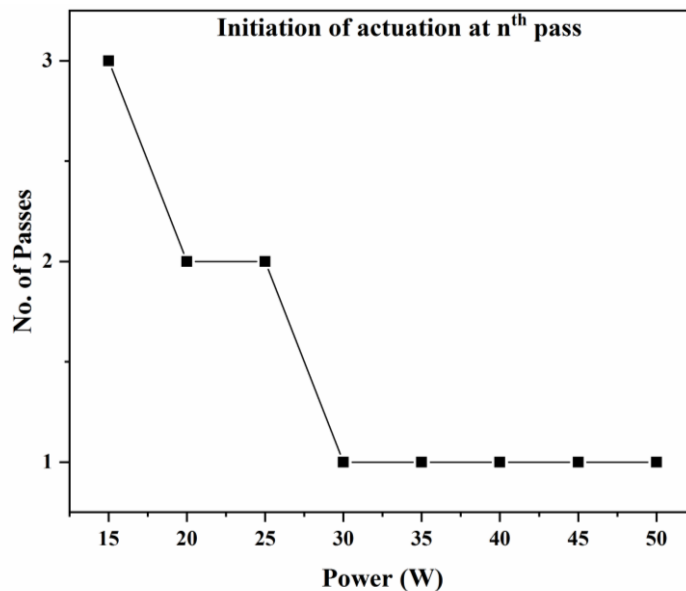


Fig. 3.23: Number of passes required to initiate the actuation in the spring for various powers

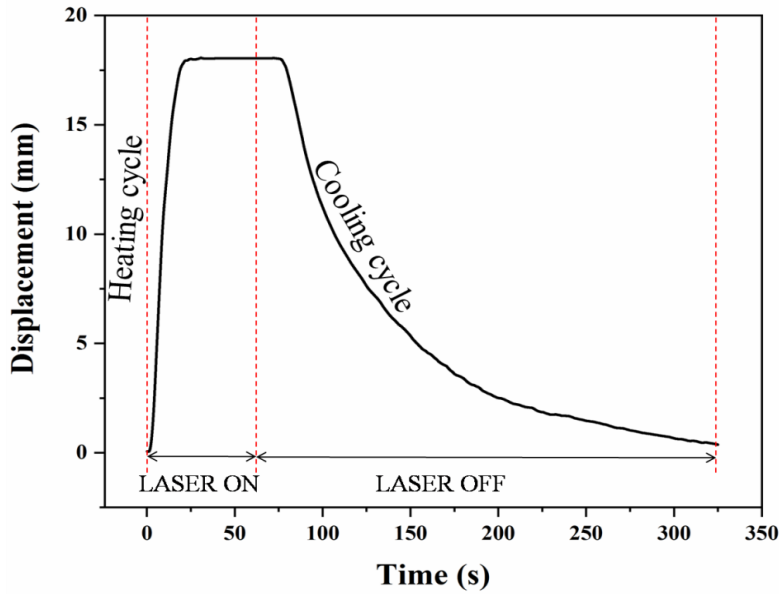


Fig. 3.24: schematic of the typical heating and cooling curve during ON and OFF of Laser irradiation

Since the number of passes decides the heating time the same trend was observed in Fig. 3.25a. The actuation against the higher bias load has taken slightly more number of passes and heating time for a particular power due to the associated higher displacements. Fig. 3.25b shows the cooling time required for each power. The higher laser power has taken more time for cooling than the lower powers. Based on this time scale the application can be designed in the future.

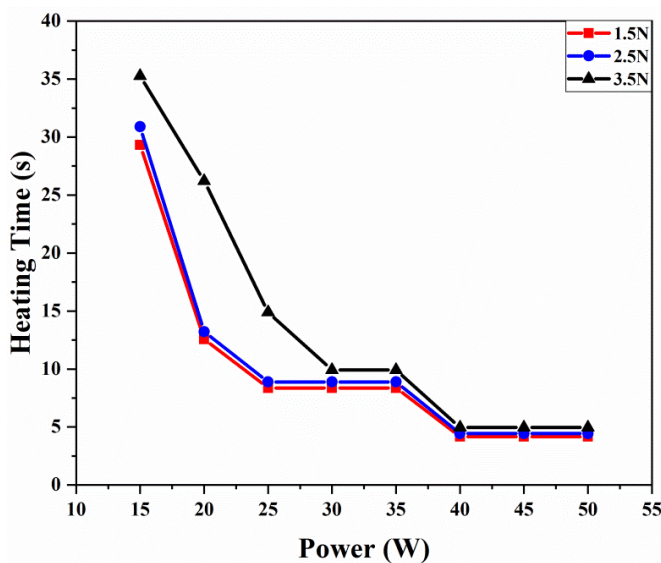


Fig. 3.25 a) Heating time vs. Power Graph

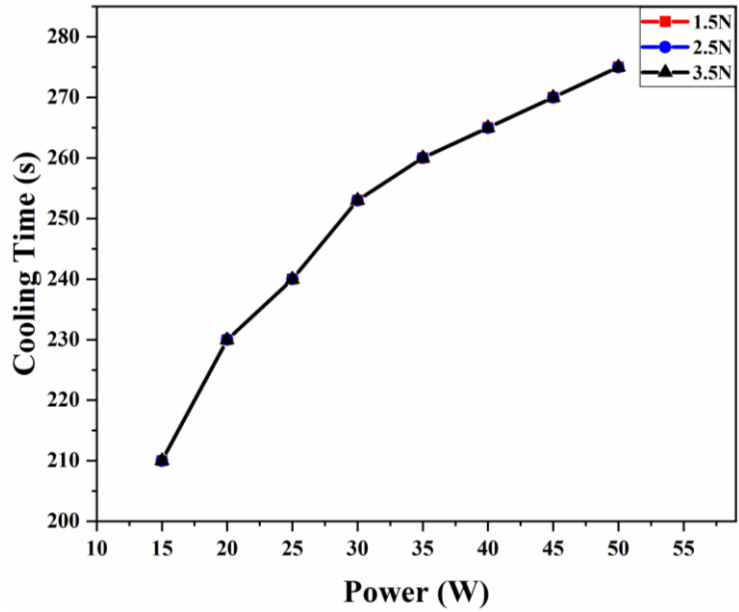


Fig. 3.25 b) Cooling time vs. Power Graph

It was observed that the increase in laser power decreases the number of passes required for the actuation, as shown in Fig 3.26.

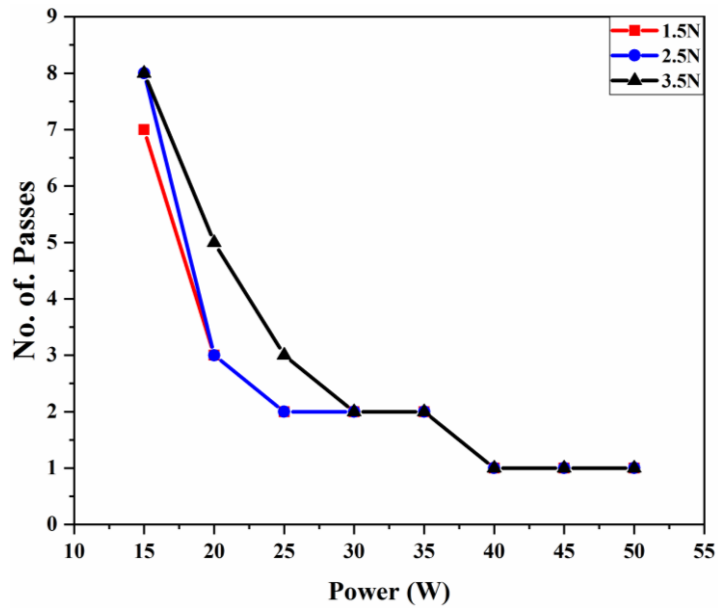


Fig. 3.26: Required number of passes with respect to an increase in laser power for complete strain recovery

Fig. 3.27 shows the displacement of the spring at various laser powers. An increasing trend in displacement against the increase in laser power was observed. This is due to the fact that the higher power has reduced

the inter-coil gap in a closed coil configuration of the spring. This is clearly evident in 2.5 N load, where above 30 W, the displacement is almost the same. So, the slightly less displacement for lower powers is due to the existence of an inter-coil gap in closed coil configuration due to the action of bias load. The inter-coil gap nullifies at higher power due to the increased heat input leading to more pull force exerted by the spring.

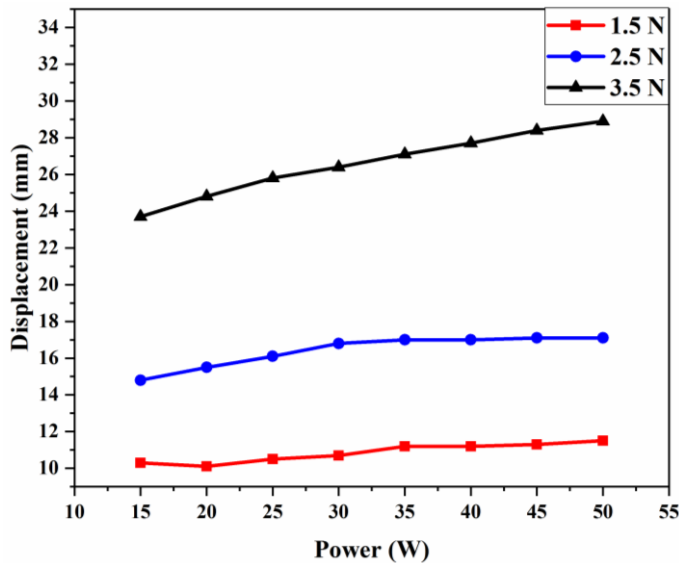


Fig. 3.27: Influence of Laser power on the displacement for the loads 1.5 N, 2.5 N and 3.5 N

A detailed study on the influence of process parameters involved in the contactless laser actuation behaviour of SMA spring has been studied. The actuation mechanism involved during the laser interaction with the SMA spring has been probed. The actuation time, involving the power and number of passes for the initiation as well the completion of actuation, for a particular bias load has been concluded. A rapid actuation with a minimum actuation time was achieved for a higher power of 50 W, whereas a higher number of passes were required for lower powers for a bias loads of 1.5 N, 2.5 N and 3.5 N. Influence of increasing the load for a constant power results in increased heating time. A better understanding of contactless actuation was attained for

the betterment of the future investigations and application for the actuation of SMA actuated meshworm robot.

Fig. 3.28 shows the continuous laser machine with the soft meshworm structure. The meshworm structure has been placed on the machine worktable. The laser in the form of a line beam has been irradiated on the SMA spring attached longitudinally to the soft meshworm structure.

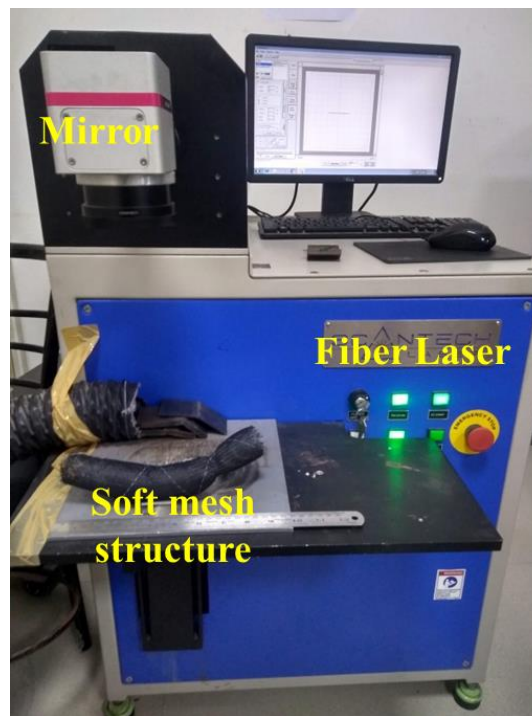


Fig. 3.28: Laser actuation of the soft mesh structure

During the irradiation of the laser line beam on the SMA spring, the soft meshworm structure bent due to the actuation of SMA spring. The laser power has been varied with no of passes to bend the meshworm structure. The initial and final position of the soft mesh structure after and before laser actuation is shown in Fig. 3.29.



Fig. 3.29: Soft mesh structure bending during laser actuation

It was observed that the increase in laser power decreases the time required for the bending of meshworm as shown in Fig. 3.30.

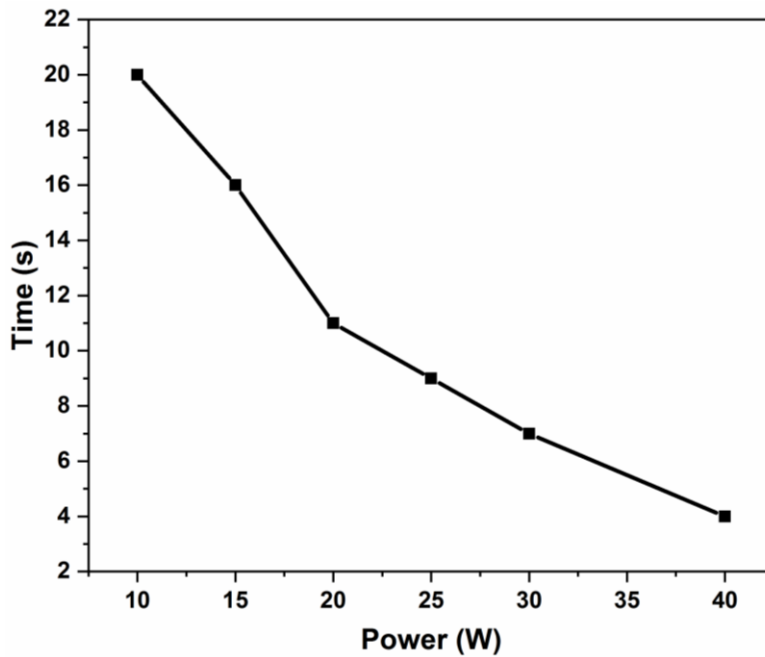


Fig. 3.30: Bending time with varying power

A maximum time of 20 s at 10 W power and a minimum time of 4 s at 40W power has been observed during the bending of soft meshworm structure.

3.9 Summary

A braided soft worm structure has been developed and its bending behavior has been studied in detail. The temperature distribution of SMA spring during the heating and cooling cycle has been evaluated using COMSOL. Thermo mechanical behavior of the SMA spring has been studied. Experiments were carried out to study the behavior of the SMA spring under conditions like varying voltage and load. The study of the bending angle was carried out with the aid of a flex sensor attached to the inner surface of the structure. Peristaltic and two anchor crawling of the mesh worm has been investigated. Non-contact type actuation of the developed robot bending has been performed using laser actuation.

- The thermal simulation SMA spring has recorded a maximum temperature of 113 °C. The spring has taken 20 s to reach the saturation temperature and 80 s to return to normal position.
- In thermo mechanical analysis, at 1.5 N, a maximum displacement of 3.9 mm was observed. The loads 2.5 N and 3.5 N have produced a maximum displacement of 7.54 mm and 9.17 mm respectively.
- Maximum bending angles of 50° to 60° showed maximum recovery of 57%. At 8% duty cycle (4.8 s heating time), the bending has reached almost 55°
- In peristaltic crawling, a bending angle of 57°, 48°, and 48° is achieved in upward, left, and right directions respectively.
- In two anchor crawling, a bending angle of 60° is achieved in the downward direction
- During laser actuation, a minimum and maximum displacement of 10.1 mm 28.9 has been obtained at 20 W and 50 W respectively.

Chapter 4

Investigations on SMA spring based actuators towards bio-inspired robotic fish

4.1 Introduction

In this chapter, a noiseless SMA spring based propulsion method for subcarangiform robotic fish has been proposed which can be employed for under water applications. The bio-inspired robotic fish has been developed with SMA spring actuators and light weight 3D printed components. The proposed SMA spring-based design without conventional motor and other rotary actuators was able to achieve two-way shape memory effect and has reproduced the subcarangiform locomotion pattern. The positional kinematic model is developed and the dynamics of the proposed mechanism were analyzed and simulated using ADAMS. An open loop Arduino-relay based switching control has been adopted to control the periodic actuation of the SMA spring mechanism. The undulation of caudal fin in air and water has been analysed. The caudal fin and posterior body of the developed fish prototype have taken part in undulation resembling subcarangiform locomotion pattern and steady swimming was achieved in water.

In conventional motor-based actuation, the motor is used to undulate the last one third portions of the body and caudal fin. Here, the SMA spring is chosen as an actuating mechanism to undulate the posterior body and the fin because of its simplicity, high stroke length, and the ability to exert more compressive force during actuation. SMA spring switches between low temperature martensite phase and high temperature austenite phase when subjected to thermal stimulation. The thermal stimulation in the form of hot water, Joule heating, and

laser-based can be used for actuating the SMA elements. However, electrical actuation or Joule heating is a simple and efficient technique for recovering the induced linear strain of a SMA spring and the actuation can be controlled effectively by varying the input current.

The main focus is to undulate the caudal fin and posterior body using a SMA spring-based mechanism and to achieve forward swimming. The design comprises of three pairs of SMA springs connecting the joints on each side. The body of the fish is made of light weight 3D printed parts driven by SMA spring arrangement. An open loop ON/OFF relay-based control was adopted to control the motion of the sequential spring arrangement and which in turn controls the fish locomotion. Preliminary studies were performed on a single SMA spring to understand the thermo-mechanical behavior in both air and water. To visualize the dynamics of the proposed design, the SMA based spring mechanism has been simulated using ADAMS. A planar positional kinematic model of the proposed robotic fish was derived using Denavit-Hartenberg (DH) parameters. The variation of caudal fin angle during oscillation was measured on air and underwater. Finally, the forward swimming of the developed robotic fish has been demonstrated.

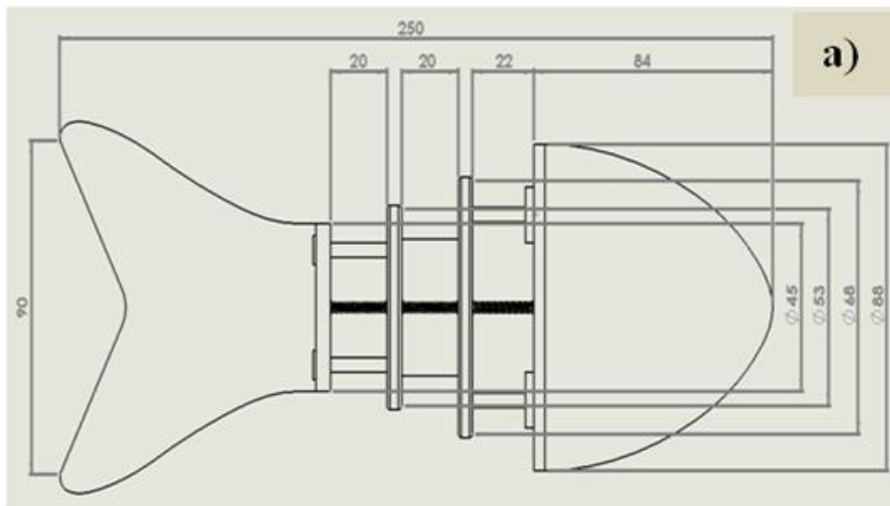
4.2 Fish Bio Mechanics

In Body caudal fin (BCF) locomotion, body undulation waves are generated which move towards the caudal fin, thereby producing propulsion. BCF locomotion is usually performed by fishes to cruise at a relatively higher speed compared to Median/Paired fin (MPF) locomotion. Based on the movement characteristics, BCF locomotion is further classified into two types, namely, (1) undulatory motion and (2) oscillatory motion. Undulatory motion is generated as a wave of muscle contraction that moves from the head to the tail and can be classified into Anguilliform, Subcarangiform and Carangiform locomotion. Oscillatory motion, on the other hand, involves swiveling

of the body and the caudal fin in order to propel the fish and can be classified into Thunniform and Ostraciiform locomotion.

The major part of the anterior portion of Carangiform and Subcarangiform robots is maintained rigid during the locomotion and therefore the body undulation is localized in the posterior portion. This causes an enhanced propulsive force. Therefore, robots inspired by Carangiform and Subcarangiform locomotion are more likely to have higher speeds compared to their Anguilliform counterparts. On the other hand, the degree of freedom of Subcarangiform and Carangiform robots ranges from one to nine which is lower as compared to Anguilliform robots in which the degree of freedom ranges from three to twenty, hence have low maneuverability compared to Anguilliform robots. Subcarangiform locomotion requires undulation of posterior half of the body of the swimmers which provides the thrust required for forward locomotion.

The proposed design of SMA based robotic fish is shown in Fig. 4.1.



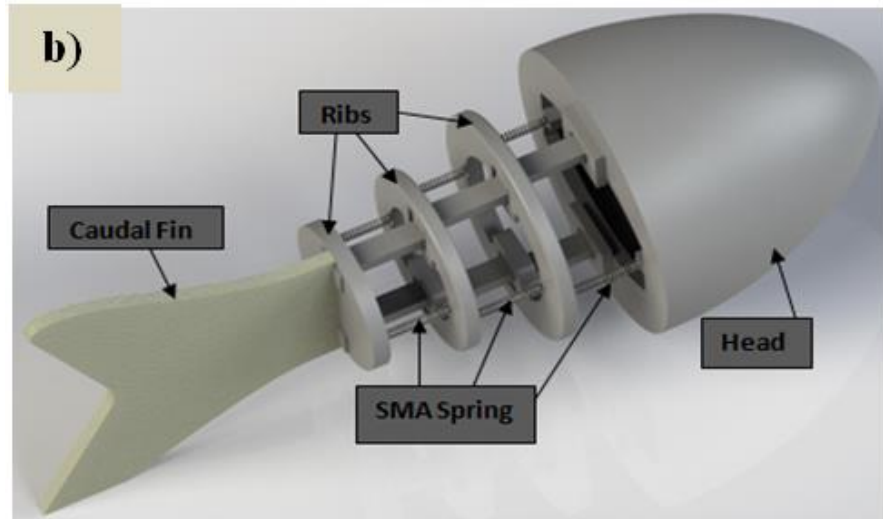


Fig. 4.1 a) Configuration of the proposed bio-inspired robotic fish in mm and b) Skeletal structure of the proposed bio-inspired robotic fish

4.3 Modeling of SMA robotic fish

In order to visualize the dynamic motion of the proposed model and fish fin oscillating mechanism in the air medium, a simulation was performed with ADAMS. The proposed fish model was developed in solid works and then imported into ADAMS for performing the dynamic simulation as shown in Fig. 4.2-4.4.

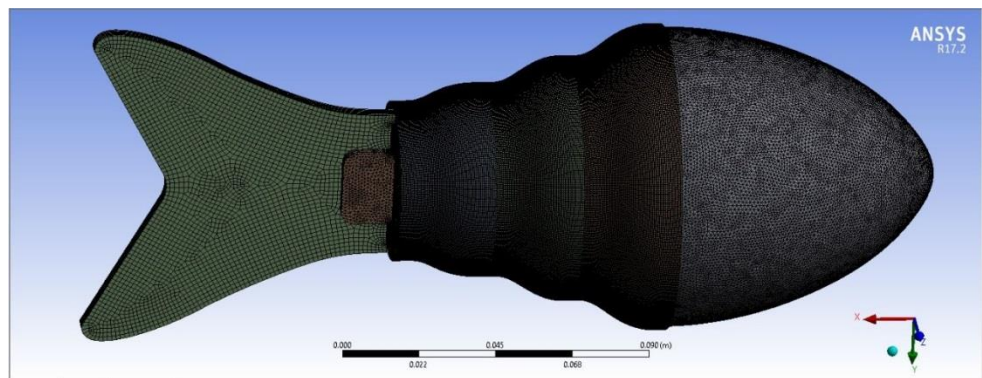


Fig. 4.2: a) Mesh structure of fish

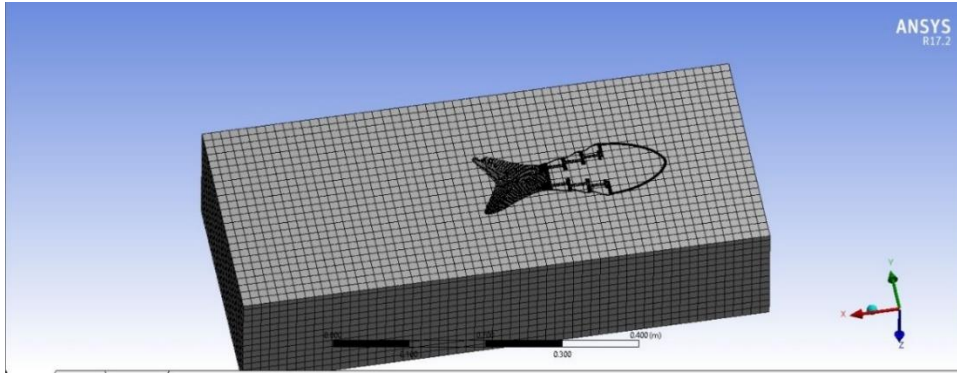


Fig. 4.3: b) Mesh structure of fish planar view

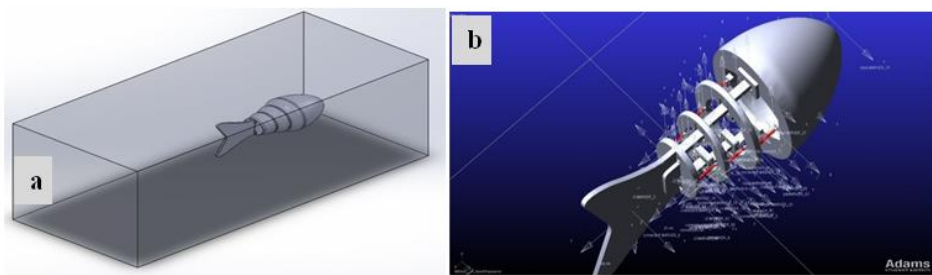


Fig. 4.4: a) Solid works model b) Adams model

The SMA spring design was developed using an inbuilt spring force function. All joints were considered as revolute joints for the simulation. The tail was fixed with respect to the last joint to hold it in position and fish head was considered as fixed. To create the fish fin like oscillation each spring was provided with external periodic force in compressive direction. The force was decided with the preliminary load study conducted on the individual SMA spring. The forces considered for the simulation were 0.01 N, 0.02 N and 0.03 N. The force less than 0.01 N would not be able to actuate the fish as it cannot overcome the inertial resistance, whereas the force more than 0.03 N would be redundant due to geometrical constraints. This was confirmed by the analysis as the simulation showed negligible motion at a force less than 0.01N and unstable motion if the force applied exceeded 0.03 N. The spring stiffness coefficient was taken to be 3 Kg/s² while the damping coefficient was taken to be 1 Kg/s. A series of simulations were performed to get dynamic behavior of the bio-inspired robotic fish for different force parameters.

The fish was assumed to actuate without cover and surrounding water for this analysis in order to get a better insight into the motion of the proposed SMA based mechanism. Through ADAMS analysis the fish fin oscillation was visualized at a frequency of 0.1 Hz. The simulated tail oscillation for the proposed SMA spring-based mechanism is shown in Fig. 4.5a. The fin displacement with respect to the time is plotted as shown in Fig. 4.5b

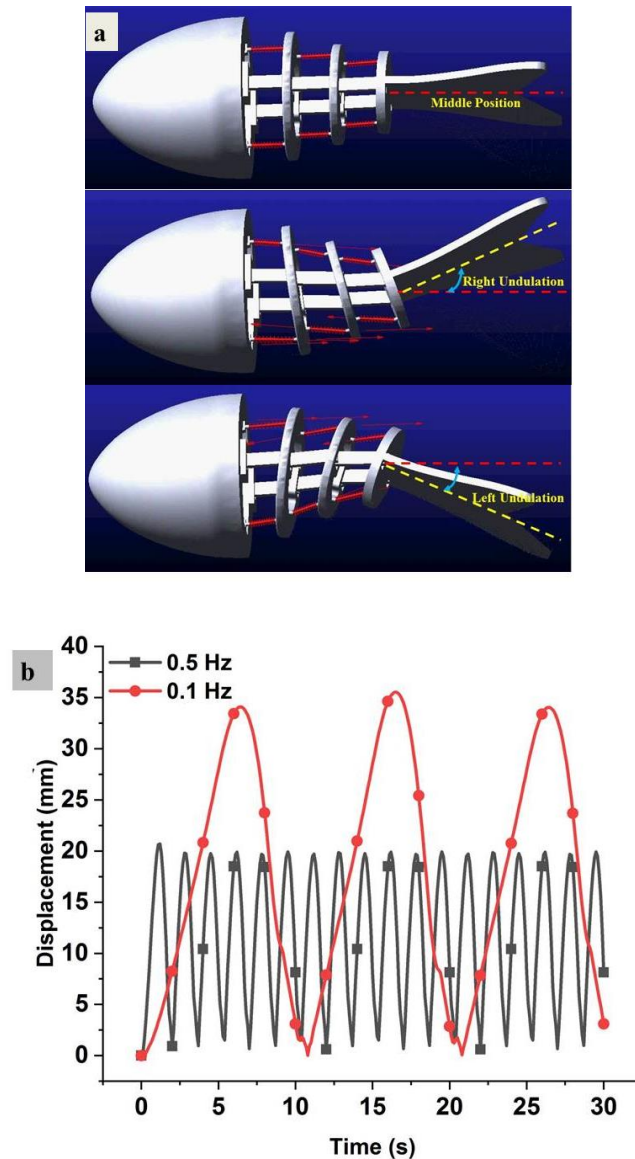


Fig. 4.5a) Adams simulation stills of the proposed SMA based robotic fish and b) Tail position at 0.1Hz and 0.5Hz

The displacement was periodic like a sine wave which showed the proper fin oscillation. This can be observed in the displacement curves

near the middle position of the fin. The data clearly depicted the presence of symmetry which plays a vital role in the actuation of SMA springs. From the simulation, it was confirmed that the proposed design could produce a smooth fish fin like oscillation which can be further investigated in the real time experimentation.

To describe the kinematic analysis, a planar positional kinematic model for the proposed bio-inspired robotic fish was obtained. The kinematic model frame diagram for the proposed fish is shown in Fig. 4.6 and 4.7

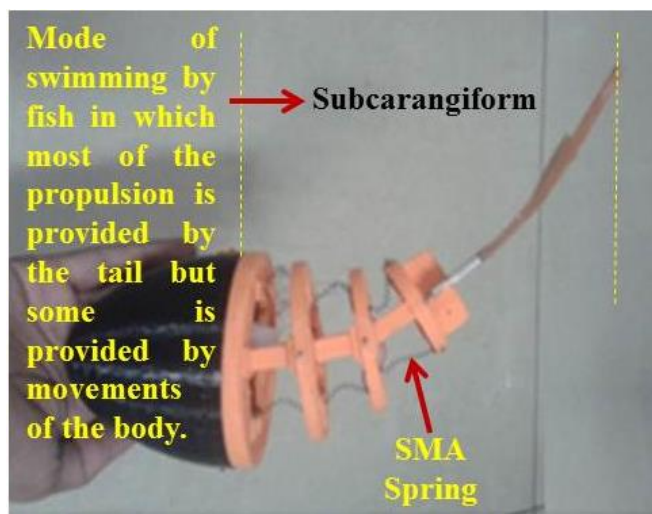


Fig. 4.6: Planar configuration for the proposed bio-inspired robotic fish

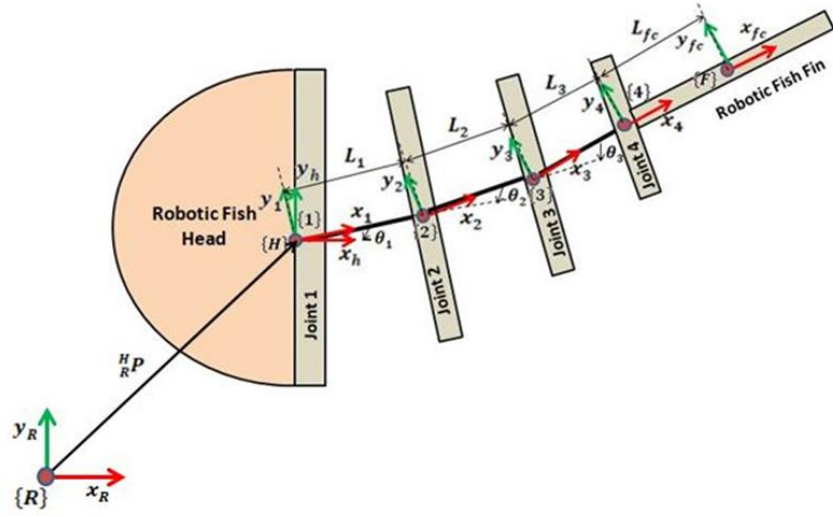


Fig. 4.7: Kinematic configuration of the proposed robotic fish

The generalized homogeneous transformation matrix is as follows.

$${}^{i-1}T_i = \begin{bmatrix} C\theta_i & -S\theta_i & 0 & a_{i-1} \\ S\theta_i C\alpha_{i-1} & C\theta_i C\alpha_{i-1} & -S\alpha_{i-1} & -S\alpha_{i-1}d_i \\ S\theta_i S\alpha_{i-1} & C\theta_i S\alpha_{i-1} & C\alpha_{i-1} & C\alpha_{i-1}d_i \\ 0 & 0 & 0 & 1 \end{bmatrix}$$

(4.1)

The DH parameters for the proposed fish were obtained from the frame diagram. Table 4.1 shows the DH parameters for the proposed fish from Fish head $\{H\}$ to center of mass position of the fish caudal fin $\{F\}$. The individual homogeneous transformation matrices are obtained from the DH Table. The number of independent kinematic parameters are θ_1 , θ_2 and θ_3 . The individual homogeneous matrices were multiplied to get the final homogeneous transformation matrix.

Table.4.1: .DH parameter table

i	α_{i-1}	a_{i-1}	d_i	θ_i
1	0	0	0	θ_1
2	0	L_1	0	θ_2
3	0	L_2	0	θ_3
4	0	L_3	0	0
5	0	L_{fc}	0	0

$$T = \begin{bmatrix} C(\theta_1 + \theta_2 + \theta_3) & -S(\theta_1 + \theta_2 + \theta_3) & 0 & L_1C(\theta_1) + L_2C(\theta_1 + \theta_2) + L_3C(\theta_1 + \theta_2 + \theta_3) + L_{fc}C(\theta_1 + \theta_2 + \theta_3) \\ S(\theta_1 + \theta_2 + \theta_3) & C(\theta_1 + \theta_2 + \theta_3) & 0 & L_1S(\theta_1) + L_2S(\theta_1 + \theta_2) + L_3S(\theta_1 + \theta_2 + \theta_3) + L_{fc}S(\theta_1 + \theta_2 + \theta_3) \\ 0 & 0 & 1 & 0 \\ 0 & 0 & 0 & 1 \end{bmatrix} \quad (4.2)$$

The planar positional kinematic model of the proposed fish at the centre of mass position of the caudal fin $\{F\}$ from the fish head $\{H\}$.

$$x_{fc} = L_1C(\theta_1) + L_2C(\theta_1 + \theta_2) + L_3C(\theta_1 + \theta_2 + \theta_3) + L_{fc}C(\theta_1 + \theta_2 + \theta_3) \quad (4.3)$$

$$y_{fc} = L_1S(\theta_1) + L_2S(\theta_1 + \theta_2) + L_3S(\theta_1 + \theta_2 + \theta_3) + L_{fc}S(\theta_1 + \theta_2 + \theta_3) \quad (4.4)$$

To get the transformation from the reference $\{R\}$, the final transformation matrix T is multiplied for the position vector ${}^H_R P$.

The caudal fin dynamics has been simulated and the maximum caudal fin angle has been recorded as shown in Fig.4.8.

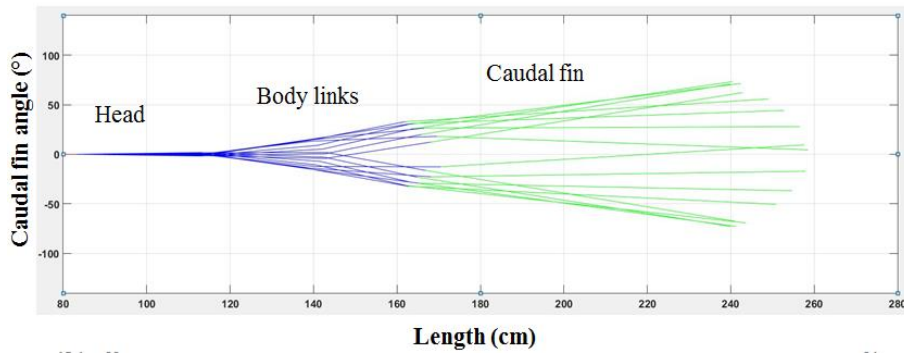


Fig. 4.8: Simulation of caudal fin angle

4.4 Fabrication of the proposed fish:

The commercially available Nickel Titanium (NiTi) SMA springs from Dynalloy Inc was used for the study. Three pairs of NiTi SMA Springs were arranged sequentially between O-ring joints on both sides. Individual SMA springs were fixed between the rib joints with an induced strain and thereby detwinning of the low temperature

martensite phase will be achieved. The flexible caudal fin made from UV cured photo polymer was attached to the rear end of the body. Initially, the springs on the right side will be actuated through Joule heating which compresses the springs and transforms to high temperature austenite phase. This actuation enables the fin to oscillate in one direction. Then the springs on the left side will be actuated and thus the two-way oscillation of the fin will be achieved. The actuation to the left will induce a pull force to the right-side springs which cools down from its high temperature austenite phase. The heating/cooling actuation cycle of the SMA springs were controlled via Arduino-relay based switching control. The actuation of the SMA springs on either side one after another enables the fin to oscillate and eventually undulate the posterior body of the fish. Fig. 4.9 and 4.10 shows the fabrication of the proposed model.



Fig. 4.9: Fabrication and validation of proposed bio-inspired robotic fish design

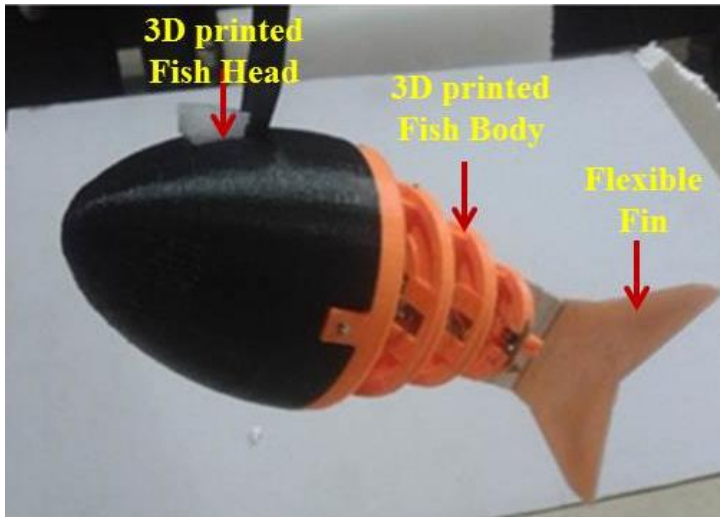


Fig. 4.10: Final robotic fish prototype

4.5 Performance Evaluation

To understand the undulation mechanism of the bio-inspired robotic fish, preliminary investigations had been conducted under water. The structure with skin covered with UV cured photo curable polymer, without head and with fin structure was tested underwater as shown in Fig. 4.11.



Fig. 4.11: Experimentation of robotic fish without head

It has been observed that the proposed SMA spring based mechanism was able to mimic the undulation pattern of a subcarangiform fish. However, the metal frame increases the inertia of the bio-inspired

robotic fish and hampering the robot to move in water with the proposed SMA spring based mechanism. Based on the understanding, the entire fish body was fabricated using 3D printed Acrylonitrile Butadiene Styrene (ABS). To investigate the performance of final 3D printed SMA spring based bio-inspired robotic fish, we conducted a set of experiments both in air and underwater. The fin displacement and maximum angle during the actuation were the key factors evaluated from the experiments. The overall weight and length of the fish without battery and electronic control board were 416 grams and 25 cm respectively. The control circuit for the fin undulation is shown in the Fig. 4.12. The SMA springs are powered through a relay circuit which is enabled by arduino control board. The arduino has been programmed to switch the relay sequentially in order to achieve the caudal fin undulation.

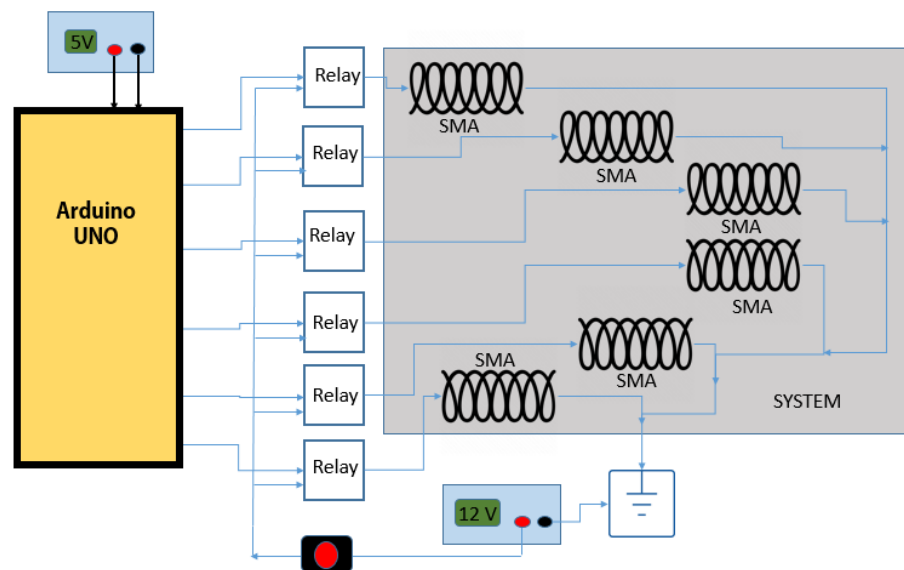


Fig. 4.12: Control circuit of the SMA spring based robotic fish

The robotic fish has been tested under water at different water channels as shown in Fig. 4.13 and 4.14. The testing has been done with and without in built onboard electronics circuit. The actuation behavior of SMA depends on input power and ambience. Here, the input current affects the rate of actuation of SMA spring and water temperature affects the cooling rate.

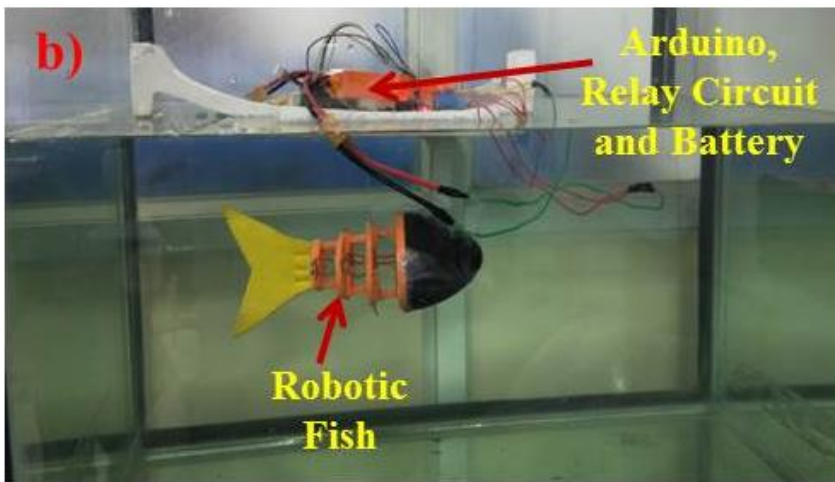
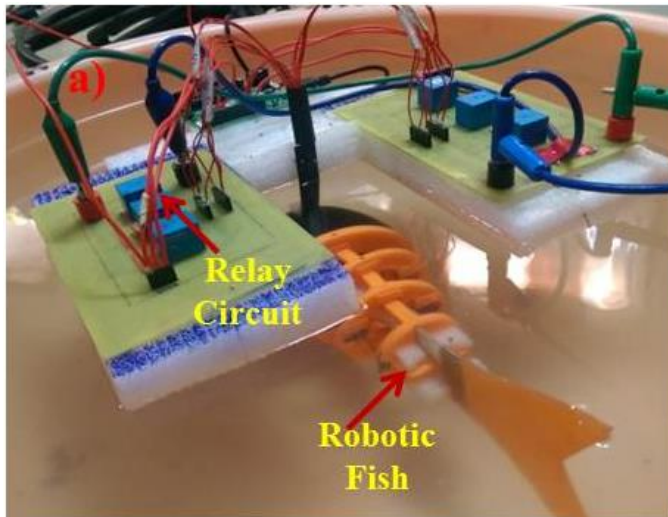


Fig. 4.13: a) Experimentation in water and b) Robotic fish experimentation in tank



Fig. 4.14: Experimentation with inbuilt electronics

In air medium, experimentation was conducted with an input current of 3 A at which the proper undulation resembling the subcarangiform fish has been obtained. The actuation behavior of SMA depends on input power and ambience. Here, the input current affects the rate of actuation of SMA spring and water temperature affects the cooling rate. This input current and water temperature influence the undulation of the bio-inspired robotic fish.

In air medium, experimentation was conducted with an input current of 3 A at which the proper undulation resembling the subcarangiform fish has been obtained. Proper undulation underwater resembling the subcarangiform fish has been obtained at an input current of 10 A. Using an infrared thermometer, the water temperature in the tank was found to be 24° C. The input current required for proper undulation has increased due to the increased heat transfer and pressure conditions experienced by the robotic fish under water.

The velocity of the SMA actuated bio-inspired robotic fish was measured at the parametric condition of 10 A and 0.1 Hz. This parametric condition has enabled the robotic fish to undulate and imitate the locomotion of the subcarangiform fish. At input currents lower than 8 A, the undulation was not proper or insufficient to enable the forward propulsion of the fish. At input current of 8 A and 9 A, the forward velocity is very minimal.

A laser displacement sensor was placed perpendicular to the fish fin to measure the fin displacement during the undulation. The measured displacement with respect to time is plotted in Fig. 4.15a. The schematic of displacement measurement is shown in Fig. 4.15b. The graph shows that the proposed SMA based mechanism generated an undulatory motion like a fish.

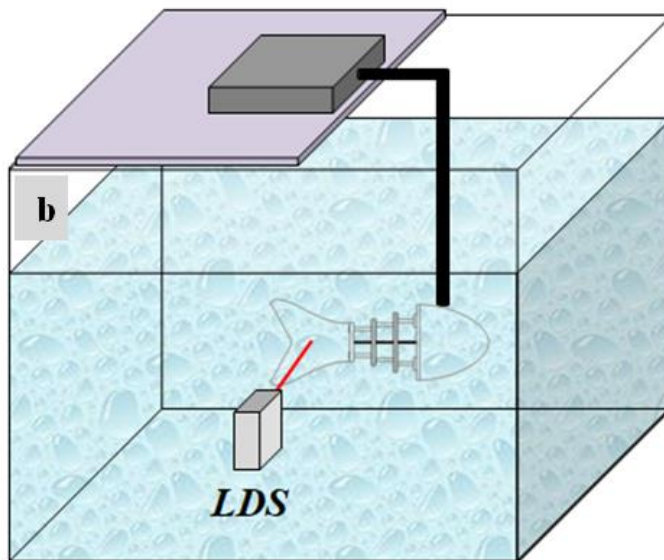
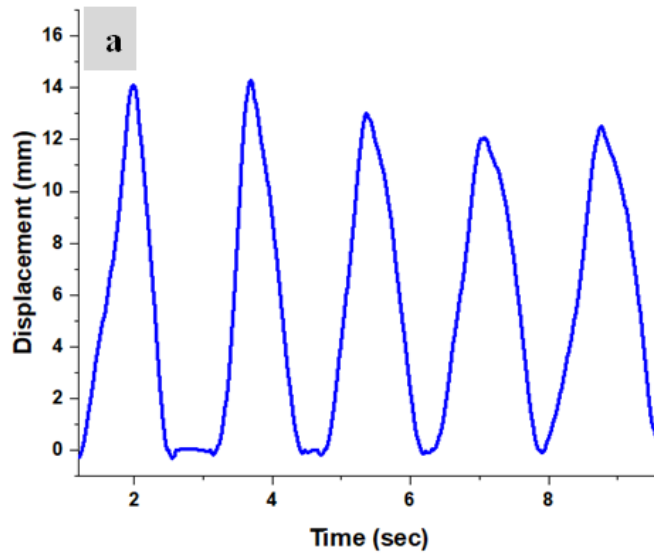


Fig. 4.15 a) Displacement curve plotted using Laser Displacement Sensor and **b)** Experimental setup for displacement measurement

To know the maximum amplitude during the oscillation of the proposed design, the angle was measured manually. The maximum angle was measured on both sides of the bio-inspired robotic fish fin in air and water medium. The angle was measured with actuating single spring, two springs together and three springs together on both sides. In air medium, a maximum angle of 51° in the right side and 50° in the left side was achieved. Whereas in the water medium, a maximum angle of 50° in right side and 49° on left side was attained. The

measured angle in both air and water with one spring, two springs and three springs were plotted and shown in Fig. 4.16.

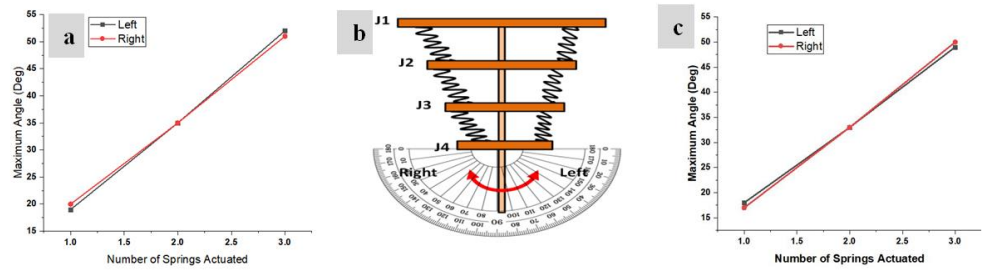


Fig. 4.16 a) Maximum Angle (Amplitude) measurement in air, b) Schematic of the angle measurement and c) Maximum Angle (Amplitude) measurement in water

The forward swimming of the proposed bio-inspired robotic fish using the SMA based caudal fin actuation mechanism is showed as a sequence of images in Fig. 4.17.

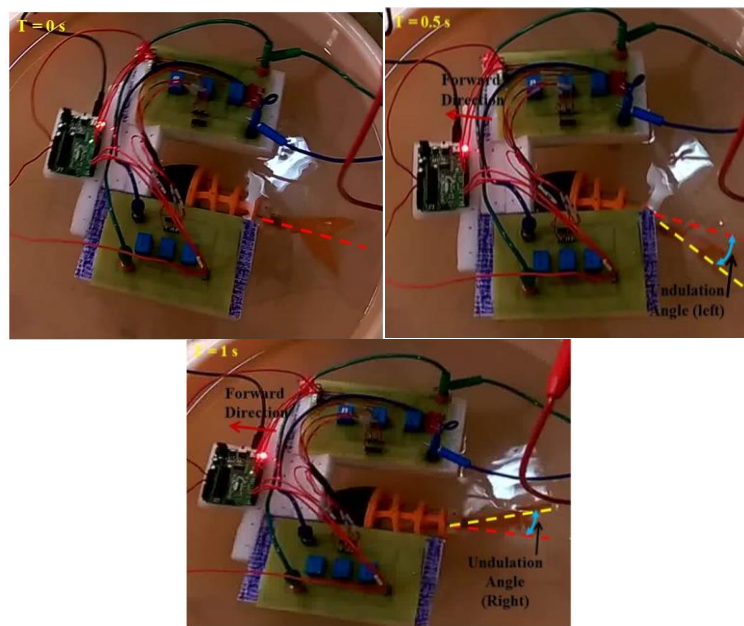


Fig. 4.17: Robotic Fish demonstration at various time instances

The force produced by SMA springs during fin oscillation was measured using a load cell arrangement in the air medium. A maximum peak force of 0.39 N at 0.1Hz was observed during the measurement. It can be noted that, over a period of time the force was reduced and becomes constant when the SMA springs reach its high

temperature austenite phase. The measured force data was plotted and showed in Fig. 4.18.

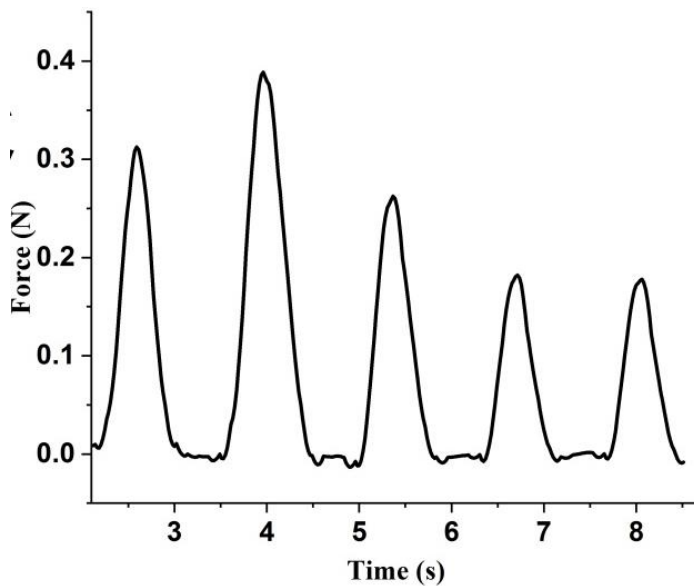


Fig. 4.18: Force produced by the proposed SMA mechanism

The caudal fin oscillation was performed by actuating the SMA springs in a sequence one after another in both the sides which bends the posterior fish body except fish head results in steady forward motion. The sequence of operation of SMA spring created a bending motion of the fish body except for the fish head and oscillated the tail, resulted in steady forward locomotion with a forward velocity of 24.5 mm/s at an actuation frequency of 0.1 Hz. The velocity of the SMA actuated bio-inspired robotic fish was measured at the parametric condition of 10 A input current at 0.1 Hz. Due to the utilization of a constant input parameter set, the undulation becomes consistent and stable forward velocity was attained by the robotic fish. Based on the length of the fish (250 mm), the speed was found to be 0.098 BL/s. As per the literature, the reported smart material based robotic fish with a velocity ranges from 25 mm/s to 150 mm/s. In our initial study, the proposed SMA spring based fish propulsion recorded a forward velocity (24.5 mm/s) which is on par with the developed smart material based robotics fish developed.

The rigidity of the fin and fish body makes the entire system stiffer and affects the swimming performance. Hence, a flexible fin structure made up of a UV cured photopolymer has been used in the study. The fish body except the head has been made flexible by incorporating a joint based design with the 3D printed parts. The SMA spring stiffness varies in its two phases. The stiffness will be more in high temperature austenite phase than the low temperature martensite phase. The Elastic modulus of SMA in austenite and martensite phases are 75-83 GPa and 28-40 GPa respectively. The swimming performance can be improved by increasing the actuation frequency which is mainly restricted by the hysteresis of SMA spring.

According to the momentum theorem, when fish swim by pushing water away behind them, momentum is transferred from the fish to the surrounding water and thrust is generated. Other kinds of forces acting on a swimming fish are drag, weight, buoyancy, and hydrodynamic lift in the vertical direction [91]. Aspect ratio, Reynolds number, reduced frequency, and Strouhal number have an important role in the thrust and propulsive efficiency of a caudal fin actuator. Table 4.2 shows the critical design parameters and its corresponding obtained values for the proposed bio-inspired robotic fish where the SMA spring based actuator mechanism was used for creating caudal fin oscillation.

Table.4.2: Critical design parameters for robotic fish [91, 92]

Critical Design Parameters	Formula	Nomenclature	Value for the Proposed Model
Aspect Ratio (AR)	$AR = b^2 / S_c$	$b =$ caudal fin span $S_c =$ caudal fin surface area	1.889
Reynolds number (R_e)	$R_e = L_F U / \nu$	$L_F =$ Characteristic length (m) of the fish $U =$ average forward velocity ($\frac{m}{s}$)	6110

		ν = kinematic viscosity of water(m^2/s^{-1})	
Reduced Frequency (σ)	$\sigma = 2\pi \frac{fL_A}{U}$	f = tail beating frequency (Hz) L_A = Characteristic length(m) of actuating system	21.39
Strouhal number (S_t)	$S_t = fA/U$	A = A is the wake width (m) (usually approximated as the tailbeat tip to tip amplitude)	0.217

For adult fish swimming, lift, acceleration reaction and pressure drag can contribute to thrust generation when the Reynolds number ranges between 10^3 to 10^5 [36]. The Reynolds number for the proposed bio-inspired robotic fish is 6110 which lies between the ranges. The Strouhal number obtained for the proposed bio-inspired robotic fish is 0.217 which is near optimal for thrust development in oscillation.

SMA's have found a number of applications in different areas. Hence, the easy and inexpensive estimation of reliability of critical components, subassemblies, or systems using SMA's is an area of importance. There are many specific reasons for looking at component data to estimate the overall system reliability. One of the most important is that in many situations it is easier and less expensive to test components/subsystems rather than the entire system. Various methods are available for the displacement measurement and life cycle analysis of the SMA spring based on inductance, resistance, load change, etc. The SMA spring reliability analysis for electrical actuation is done with simple interferometry technique. The experiments for many hours in SMA springs for various purposes and the springs were found to work without failure. The in-house experimental setup of the reliability test of SMA spring is used for the reliability study. The SMA spring has been fixed at one end and the other end has been attached with the load. The reliability test has been conducted with accelerated loading conditions. Based on the study, the SMA spring shows good performance with minimal displacement drift even after 5000 cycles. As per the life cycle of SMA spring, the reliability is

expected to be good. However, detailed in order to find the overall reliability of the overall system detailed investigation can be carried in our future works.

4.6 Summary

Design and experiments of a bioinspired noiseless SMA based propulsion method for robotic fish is successfully developed and tested underwater. The dynamics of the proposed design, the SMA based spring mechanism has been simulated using ADAMS. A planar positional kinematic model of the proposed robotic fish was derived using Denavit-Hartenberg (DH) parameters and simulated. The maximum amplitude angle during oscillation in both sides (on air and underwater) with concern SMA springs is observed. The displacement during caudal fin undulation has been measured. The force produced by SMA springs during fin oscillation was measured using a load cell arrangement.

- ADAMS analysis of the fish fin oscillation was visualized at a frequency of 0.1 and 0.5 Hz. A maximum fin displacement of 35 mm and 20 mm has been observed at 0.1 and 0.5 Hz respectively.
- A maximum displacement of 15 mm during the caudal fin undulation has been recorded experimentally at 0.5 Hz.
- In the air medium, a maximum angle of 51° on the right side and 50° on the left side was achieved. Whereas in water medium, a maximum angle of 50° on the right side and 49° on the left side was attained.
- Force produced during the fin oscillation is measured and maximum force of 0.39 N at 0.1 Hz is obtained.
- The developed robotic fish achieved a steady swimming at velocity of 24.5 mm/s.

Chapter 5

Investigations on SMA bimorph towards bio-inspired soft robot

5.1 Introduction

In this chapter, SMA bimorph has been developed and its various performance characteristics have been investigated. Initially, the modelling of SMA bimorph has been performed to evaluate the temperature generation during actuation. Then the fabrication and actuation characteristics of the SMA bimorph have been investigated in detail. In addition, a PID control scheme has been implemented for SMA bimorph. A SMA bimorph based soft robot for micro positioning applications has been proposed and demonstrated.

5.2 SMA Bimorph based soft Robot

A SMA bimorph actuator is a composite structure composed of flexible polyimide substrate and SMA thin film deposited using the thermal evaporation technique. The substrate thickness in the range of 25 - 75 μm was selected for the development of CuAlNiMn SMA bimorph actuator. An investigation on the control behavior of copper based SMA bimorph towards the development of micro positioning system has been performed. The actuation behavior of the SMA bimorph was studied using electrical actuation. Subsequently, a Proportional Integral Derivative (PID) controller was designed to control the bimorph actuator with proper tuning of gain parameters. The displacement of the bimorph actuator was controlled through a dedicated experimental setup consisted of a laser displacement sensor, data acquisition system and LabVIEW software. The CuAlNiMn SMA bimorph actuator resulted in a satisfying control performance which can be extended to MEMS applications. A preliminary prototype of the

SMA bimorph actuator based micro positioning system has been developed. It consists of three SMA bimorph links arranged in a parallel manipulator configuration with one end of each bimorph fixed to the base. The other end of bimorph is attached to the top plate which undergoes micro positioning. By actuating three bimorph links simultaneously, the top plate moved in a vertical direction along z axis. By actuating any two links, a twisting orientation can be achieved. The proposed design of the SMA bimorph based soft robot is shown in Fig. 5.1.

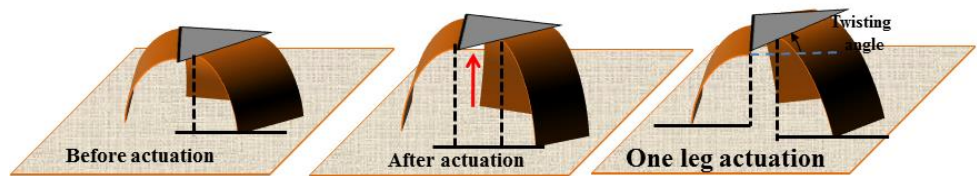


Fig. 5.1: Design of the SMA bimorph based soft robot

5.3 Modeling of SMA bimorph

The SMA bimorph has been modeled in COMSOL and its temperature distribution with respect to the input voltage has been simulated. For the case of Boundary Conditions in Joule heating, The bimorph is kept in ambient temperature. A small copper plate was added to the bimorph and it will be connected to the ground and source respectively. The governing equations for joule heating as follows.

Heat Transfer and Electric currents module in COMSOL Multiphysics were coupled. The heat generation in the sample during the electricity supply is given by,

$$J = \sigma E \quad (5.1)$$

$$E = -\nabla V \quad (5.2)$$

Where J - Current Density, E - Electric Field, V- Electric potential. The heat transfer due to conduction and convection is given by,

$$\rho C_p u \cdot \nabla T + \nabla \cdot q = Q \quad (5.3)$$

$$q = -k \nabla T \quad (5.4)$$

$$q = h_c A \Delta T \quad (5.5)$$

Where ρ -density of the sample, C_p -specific heat, u -velocity of flow, k -thermal conductivity, A - exposed surface area and h_c -convective coefficient.

From the COMSOL simulation, it can be observed that at 3 V, a maximum temperature of 193°C has been recorded which is closer to the DSC values (Fig. 5.2).

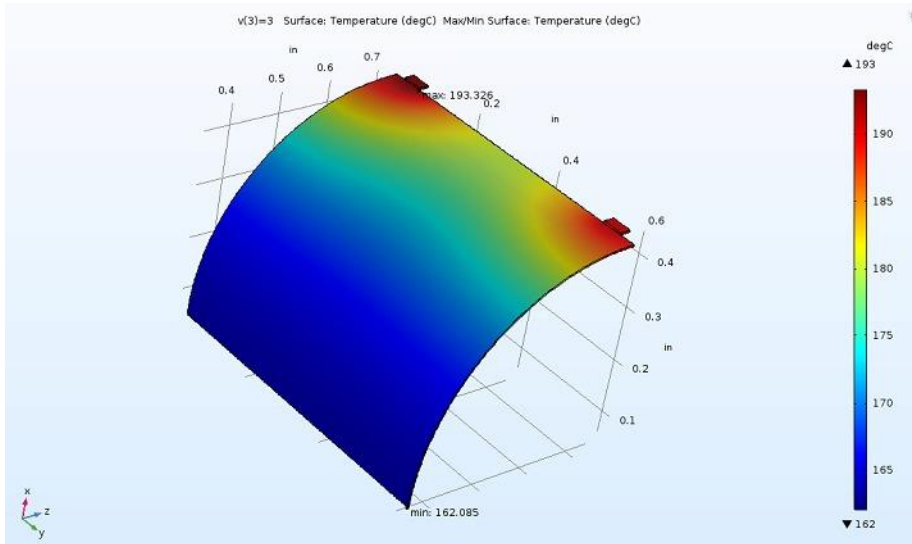
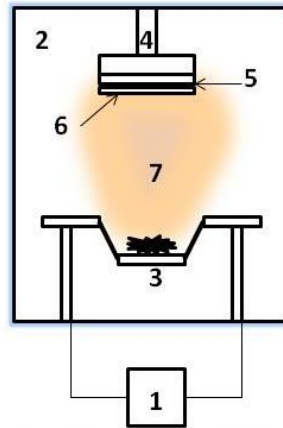


Fig. 5.2: Temperature distribution of SMA bimorph

5.4 Fabrication of SMA bimorph

CuAlNiMn thin film of thickness 2 μm was deposited on kapton polyimide (flexible substrate) using thermal evaporation technique as shown in Fig. 5.3.



1. To vacuum pump 2. Vacuum chamber 3. Tungsten boat
4. Substrate holder 5. Substrate 6. SMA thin film
7. Thermal Evaporation

Fig. 5.3: Schematic of thermal evaporation technique

The kapton polyimide substrate was cleaned and baked before deposition. The polyimide was prestrained and placed in the substrate holder. The source material CuAlNiMn pellet of weight 1 g was placed in the tungsten crucible and evaporated to form the thin film over the polyimide substrate. During the deposition, the vacuum pressure of 5×10^{-5} mbar was maintained in the chamber. Thin films were fabricated on different substrate thicknesses viz. 25 μm , 50 μm , and 75 μm . Fig. 5.4 shows the developed SMA bimorph actuator with different substrate thicknesses. The SMA film thickness was kept constant throughout the work and the substrate thickness has been varied.

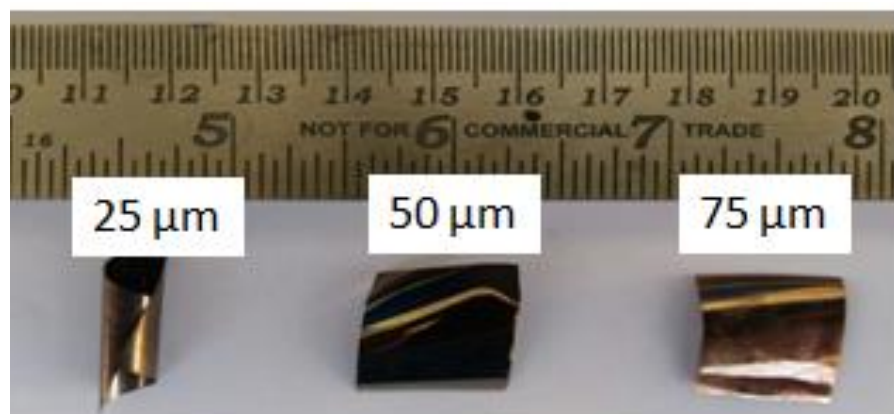


Fig. 5.4: Developed bimorph with different substrate thickness

The phase transformation temperature was identified using differential scanning calorimetry (DSC). The phase transformation temperature of CuAlNiMn bimorph after deposition was found to be austenite start (A_s) = 221 °C and austenite finish (A_f) = 235 °C as shown in Fig.5.5. There was no evidence of martensite transformation during the cooling cycle for the samples. The absence of a transformation peak might be due to the effect of the polyimide substrate, which might affect the cooling rate.

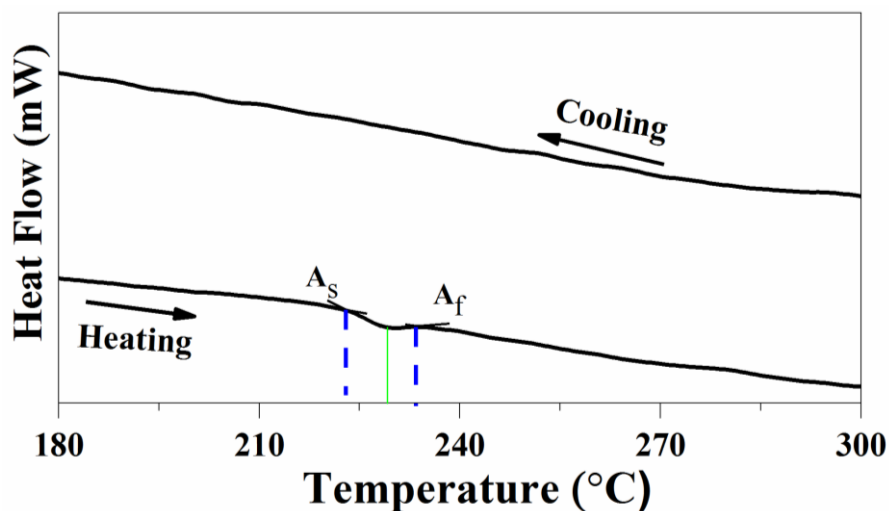


Fig. 5.5: DSC plot of CuAlNiMn SMA Bimorph

Energy dispersive spectroscopy was used to analyze the composition of the thin film. The atomic composition of CuAlNiMn SMA bimorph is given in table.5.1.

Table.5.1: Composition of CuAlNiMn Bimorph

Element	Composition (at. %)
Cu	66.90
Al	25.85
Ni	3.2
Mn	4.01

5.5 Performance Evaluation

5.5.1 Experimental setup for actuation and motion control

The schematic of the experimental setup is shown in Fig. 5.6. LDS was used to measure the tip displacement of the bimorph and interfaced with LabVIEW software through a data acquisition (DAQ) Agilent 34970A system.

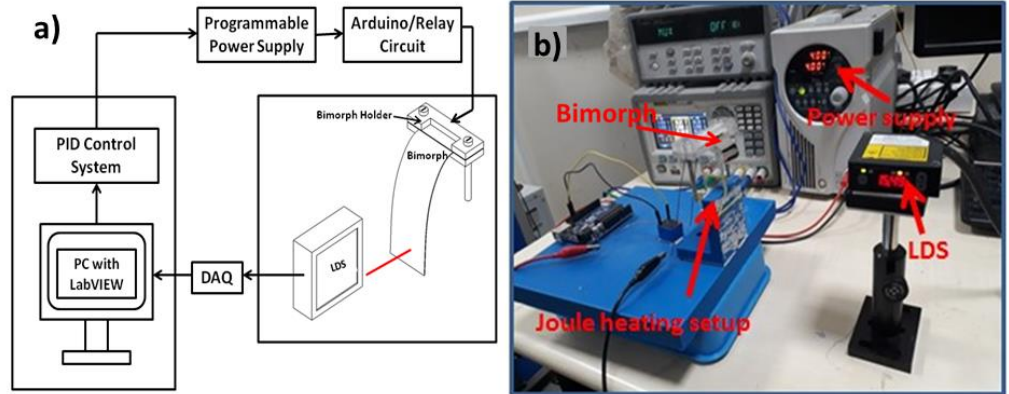


Fig. 5.6: a) Schematic of Experimental Setup b) Actual image of the experimental setup

The bimorph was actuated through electrical actuation (Joule heating) and the input to the bimorph was fed using RIGOL programmable power supply with an Arduino based relay circuit. The resolution of DAQ and LDS are 12.5 ns and 2.5 μm respectively.

5.5.2 Actuation capability of SMA bimorph actuator

SMA bimorph actuator with varying substrate thickness (75 μm , 50 μm , and 25 μm) have been used for the analysis. The sample size considered for the experiment was 2 cm \times 3 cm. Fig. 5.7 shows the maximum displacement of bimorph with respect to varying voltage and different substrate thicknesses. The voltage was applied until the SMA bimorph moves from the initial position to the maximum position (i.e. until it stops moving) and the corresponding displacement was considered as maximum displacement.

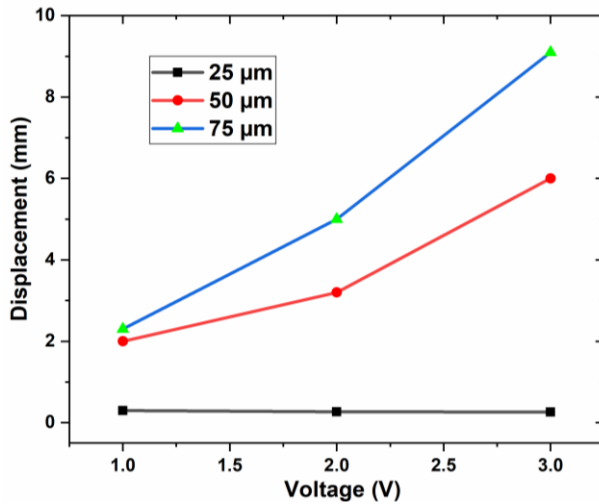


Fig. 5.7: Voltage vs. displacement curve with different substrate thickness

It can be clearly observed that the bimorph with substrate thickness 75 μm shows higher displacement than the others. During the deposition, the material vapor will transfer some thermal energy to the substrate. Due to this, the thinnest substrate (25 μm) swirls more after deposition (Fig. 5.4). Because of the lower stiffness of 25 μm and 50 μm substrate, it was unable to counteract the compressive thermal stress induced by SMA film on the substrate upon deposition. The radius of curvature is higher for bimorph with lesser substrate thickness. When the substrate thickness increases, the bimorph stiffness gets increased and it can easily counterpart the thermal compressive stress induced by SMA thin film. This could be the reason for the higher displacement with respect to increased substrate thickness. Hence, the SMA bimorph actuator having 75 μm substrate thickness was utilized for further investigations. The actuation characteristics with respect to displacement and voltage have been performed. The bimorph displacement was measured for 2 V and 3 V and plotted in Fig. 5.8. It can be observed that a maximum of 9 mm was achieved at 3 V.

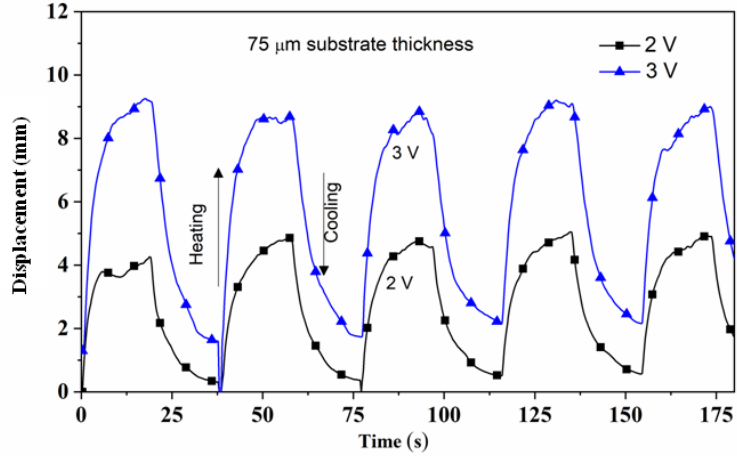


Fig. 5.8: Time vs. displacement curve for 2 V and 3 V

As a part of thermo mechanical analysis through Joule heating, displacement under different bias loads has been carried out. The SMA bimorph was considered as a cantilever beam. One end of the bimorph is fixed in the bimorph holder and load has been attached to the other end. The load has been varied as 30 mg, 45 mg, and 60 mg for the investigation. Fig. 5.9 shows the maximum displacement with varying loads. It is evident that the bimorph can be actuated with load and extended for MEMS application.

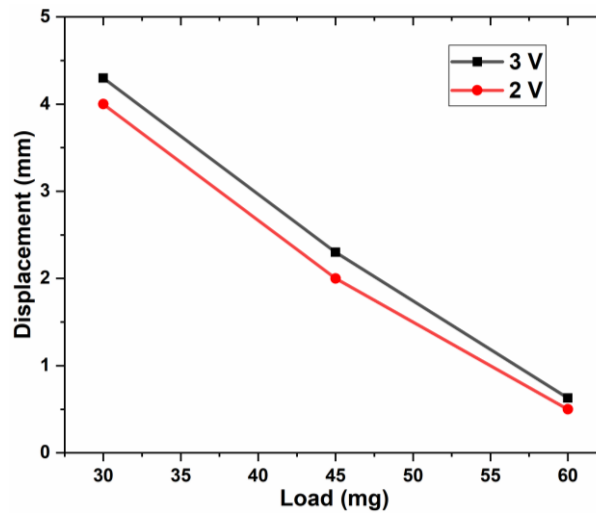


Fig. 5.9: Maximum displacement with different loads

5.5.3 Shape Recovery Analysis

The performance of the SMA bimorph was evaluated using shape recovery ratio analysis. The set of experiments were performed with plate heating to investigate the heating and cooling behavior of the composites by direct heat transfer. The shape recovery ratio was plotted as shown in Fig. 5.10. CuAlNiMn SMA/Kapton composite had a recovery of 2.43.

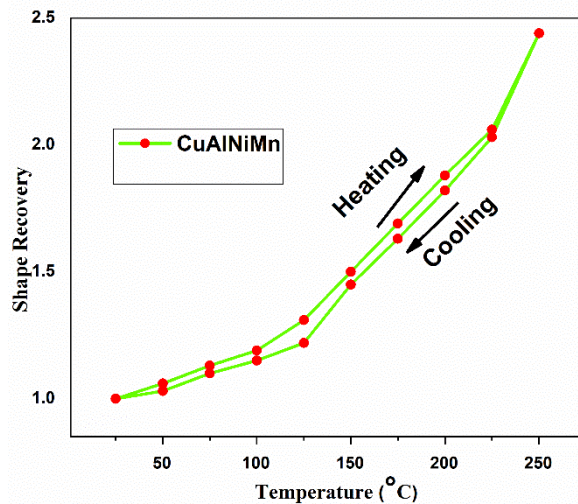


Fig. 5.10: Shape recovery analysis of SMA bimorph

In order to verify the life cycle of the bimorphs, an actuation condition of 2 V was taken for the analysis. Eight samples were considered for the study and the samples were actuated till the displacement reduced less than 50 % of the initial value. Most of the samples had life more than 20,000 cycles before losing 50 % of the displacement. The life cycle analysis exhibited the property of the composite films to actuate under high loads for more number of cycle, making it a suitable for micro actuators.

5.5.4 Controller Design

Proportional Integral Derivative is a method based on the control loop feedback. PID controller can be understood as a controller that takes the present, the past, and the future of the error into consideration. The PID control equation is given as

$$u(t) = K_p * e + K_i * \int_0^t e dt + K_d * \frac{de}{dt} \quad (5.6)$$

Where $u(t)$ = Displacement, e = error, K_p = Proportional gain, K_i = Integral gain, K_d = Derivative gain. Error $e = D_d - D_a$ where, D_d = Desired displacement (set point) and D_a = Actual displacement. The schematic block diagram of the PID controller design used for the SMA bimorph is shown in Fig. 5.11. The PID controller was designed in LabVIEW platform. The desired set point is given through the front panel of the LabVIEW. The actual displacement of the bimorph was measured using LDS. The difference between desired displacement and actual displacement is the displacement error e which will be further fed into the PID control equation.

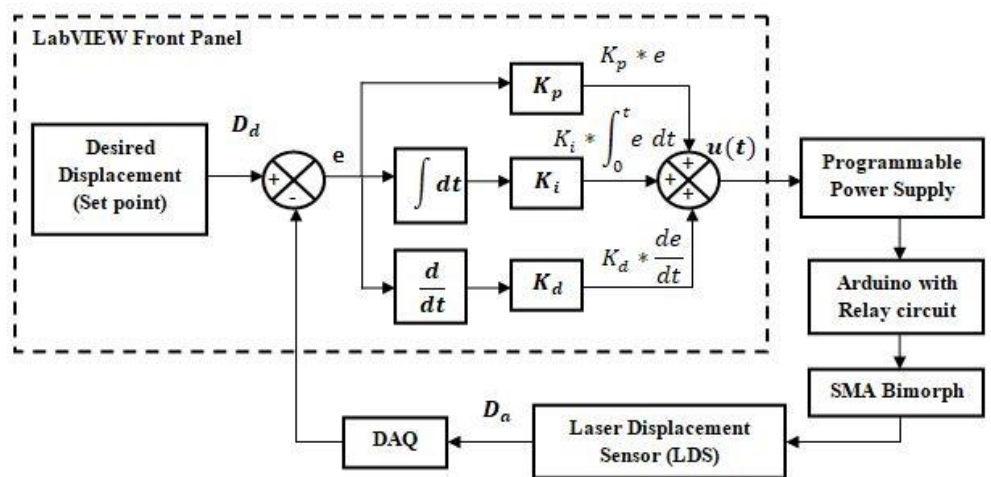


Fig. 5.11: Block diagram of PID control of SMA bimorph actuator

The final displacement correction $u(t)$ is fed into the SMA bimorph through programmable power supply and Arduino with a relay circuit. The controller gain is adjusted and tuned accordingly to minimize the error to zero. The PID control module in LabVIEW was fed with preliminary study data of bimorph actuation. The voltage fed into the bimorph is controlled through programmable power supply. The voltage with a stipulated time is the control signal fed to the SMA bimorph. The LabVIEW acts as the main controller and Arduino acts as a slave controller. The Arduino was interfaced with LabVIEW through Interface for Arduino (LIFA).

5.5.5 Investigation on control of the bimorph

An initial test has been performed to find the input range at which the displacement of bimorph occurs. The bimorph started actuating between an input range of 0-3 V. The operating range has been given to the PID module output in the LabVIEW environment. Initially, the PID controller gain parameters are tuned based on trial and error method. A set point displacement control has been done to find out the critical gain. The bimorph control has been performed to know the critical gain values region where the system is stable. The gain value K_p increased until the displacement reached the set point, K_i increased to decrease the precision error and K_d was increased to reduce the overshoot. In trial and error based method different gain values generated quasi-semi stability of displacement to reach the desired set point position. It has been observed that the gain $K_p=9.5$ produce less oscillation and achieved stable displacement compared to other gain values. The proportional gain value has been varied from 0 to 9.8. The integral gain value has been varied from 2.5-3.2. The derivative gain value has been varied from 2.7-3.3. For integral gain, above these ranges, the system showed more oscillation. For derivative gain, above these ranges, the system could not reach the set point. Integral absolute error (IAE) has been calculated for different gain values and tabulated as shown in Table.5.2.

Table.5.2: Cumulative error for the various proportional gain

Proportional Gain	IAE (m)
9	0.08298
9.5	0.01497
9.75	0.0823
9.74	0.09476
9.76	0.0847
9.78	0.07864

9.82	0.07678
9.85	0.08713
9.8	0.07469

The set point 0.5 mm is again tested with the gain values and plotted in Fig. 5.12. Here the error comparing to set point was more and has more peaks. The controller needs to be tuned more precisely to reach the desired set point with less fluctuation, minimum error and stability.

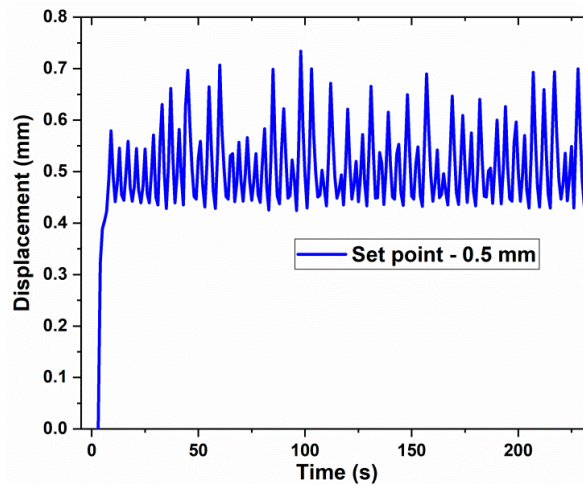


Fig. 5.12: Displacement Stability for gain $K_p = 9.5$ (set point of 0.5 mm)

Based on the critical gain values the controller was designed using standard Zeigler Nichol's (Z-N) method [93]. In the Z-N method, increasing the K_p value from 0 to a critical value $K_{cr} = 9.8$ exhibited sustained oscillations. The corresponding critical period value $P_{cr} = 4$ have been determined experimentally. Based on the K_{cr} and P_{cr} values, the proportional gain K_p , integral gain K_i and derivative gain K_d have been found using the Z-N tuning rule. As per Zeigler-Nichol's rule, it was performed by setting the integral and derivative gains to zero. Then the proportional gain was increased from zero until it reaches the ultimate gain or critical gain, at which the output of the control loop has stable and consistent oscillations.

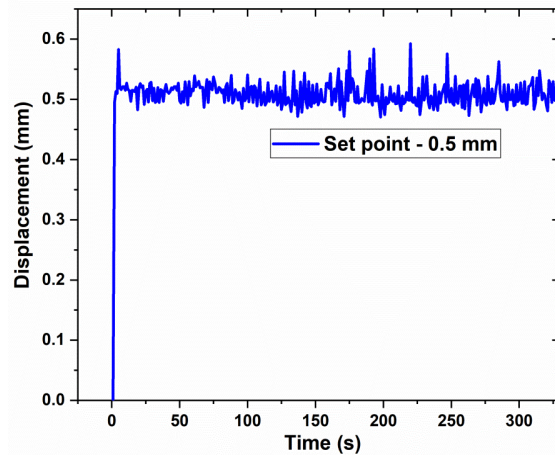


Fig. 5.13: Time vs. Displacement for set point of 0.5 mm using the standard parameter Z-N method

The bimorph stability for the standard Z-N method critical gains is shown in Fig. 5.13. It can be observed that the system is stable with minimal error. The tuned value of PID controller parameters is $K_p = 5.88$, $T_i = 2$ and $T_d = 0.5$. Based on the obtained result using tuned Z-N parameters, it shows that the SMA bimorph motion can be controlled. The error with respect to the desired set point is less for CuAlNiMn bimorph and evidences the better control characteristics of CuAlNiMn bimorph. To ensure the same behavior, the bimorph control has been tested for different set points from 0.6 mm to 1 mm at an interval of 0.1 mm. Fig 5.14-5.16 shows the time vs. displacement graph for various desired set point of 0.6 mm to 1 mm. From the results, it was observed that the position of the bimorph actuator accurately changes with respect to the desired set point with minimal error and stability. Especially with the tuned Z-N parameters, the oscillations were reduced and the bimorph becomes stable with minimum error. The standard deviation, a 95% confidence interval is 0.793 ± 0.020 (range between 0.793 to 0.813).

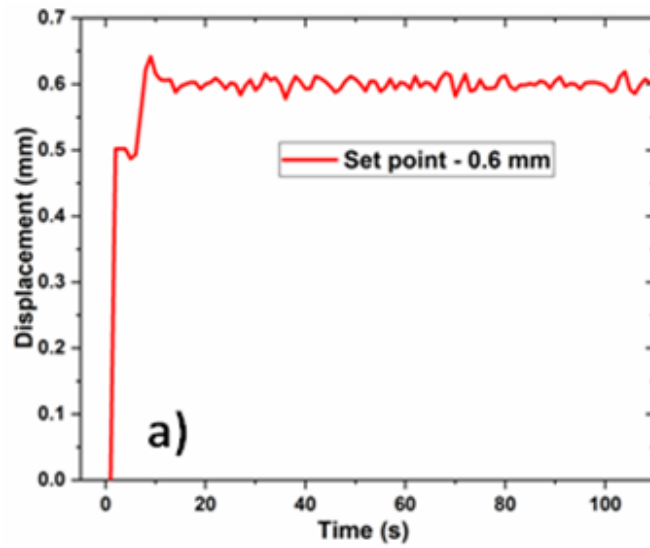


Fig. 5.14: Set point control for 0.6 mm

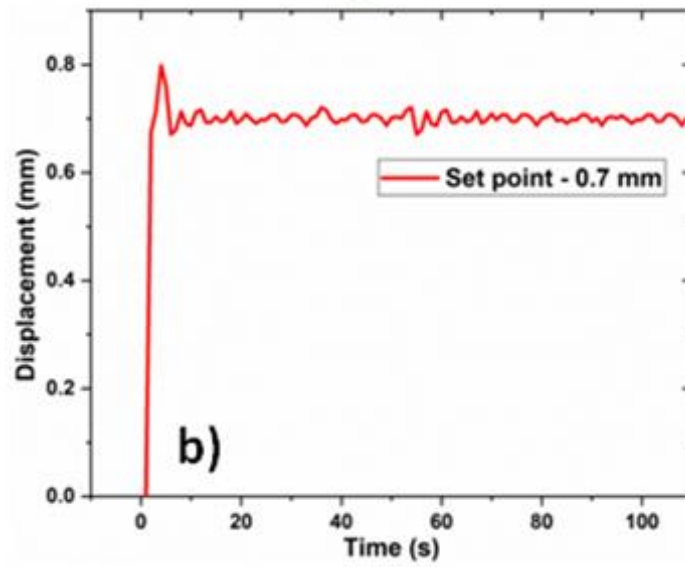


Fig. 5.15: Set point control for 0.7 mm

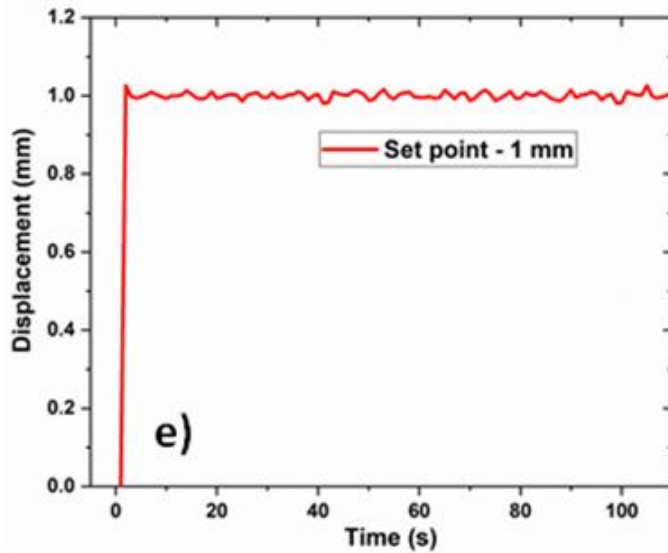


Fig. 5.16: Set point control for 1 mm

5.5.6 SMA bimorph based soft robot prototype

A preliminary prototype of SMA bimorph actuator based micro positioning system has been developed for MEMS applications. The developed micro positioning prototype can be used for manipulating smaller objects with high precision. The developed SMA bimorph actuator based micro positioning system is shown in Fig. 5.17-5.18.

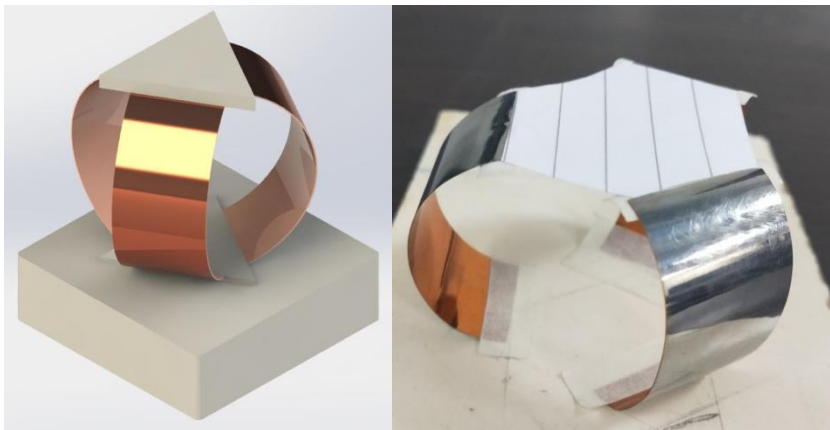
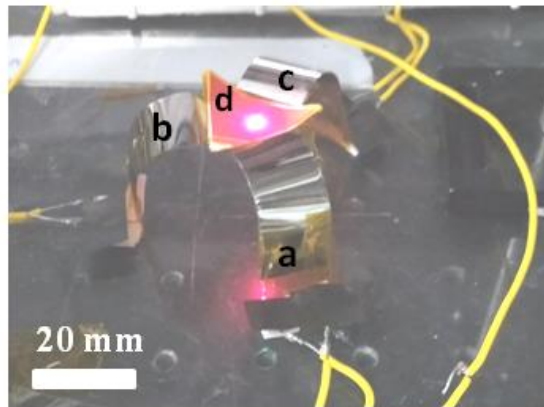


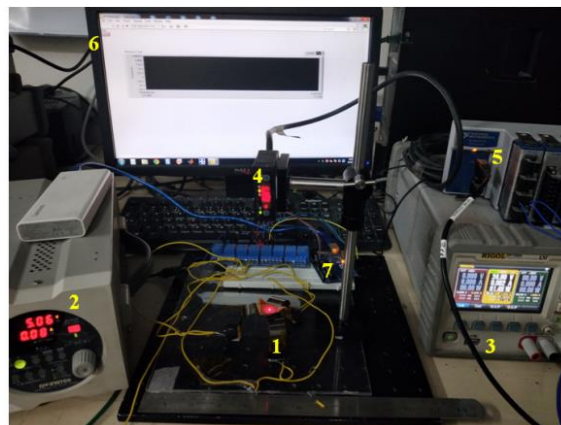
Fig. 5.17: SMA bimorph based soft robot



a) Link 1 b) Link 2 c) Link 3 d) Top plate

Fig. 5.18: Preliminary prototype of the proposed SMA bimorph actuator based soft robot for MEMS applications

During the initial study, it has generated a displacement of 5 mm vertically. The displacement has been measured using LDS and the experimental setup as shown in Fig. 5.19.



1) SMA Bimorph based Stewart platform 2) Power supply for Bimorph 3) Power supply for LDS 4) Laser displacement sensor (LDS) 5) Data acquisition system (DAQ) 6) PC with Lab VIEW 7) Arduino with relay circuit

Fig. 5.19: Experimental Setup

By actuating three bimorph links simultaneously, the top plate moved in vertical direction along z axis. It has generated a displacement of 5 mm vertically. By actuating any two links, a twisting orientation can be achieved. The work volume is approximated to a triangular prism during the movement of all the links vertically. For the displacement of the robot to 5 mm vertically, a work volume of 1.35 cm^3 .

5.6 Summary

- CuAlNiMn SMA thin film was successfully fabricated on a flexible substrate of different thicknesses using the thermal evaporation technique.
- The thermo mechanical analysis of the SMA bimorph with varying voltage and load has been performed.
- PID controller has been implemented successfully to control the SMA bimorph. The controller gains have been tuned with Zeigler Nichol's method.
- The SMA bimorph control has been investigated for different set points. A SMA bimorph based soft robot has been developed.
- The SMA Bimorph with 75 μm substrate thickness showed a better performance compared to bimorph with lesser substrate thickness.
- A maximum displacement of 9 mm was achieved at 3 V.
- The actuation characteristics with respect to the varying load of 30 mg, 45 mg and 60 mg have been performed. A minimum displacement of 0.6 mm at a maximum load of 60 mg has been achieved.
- PID controller has been implemented successfully to control the SMA bimorph for different set points.
- The results confirmed that the SMA Bimorph can be controlled and extended for dedicated robotic applications such as star fish robot.

Chapter 6

Investigations on SMA wire integrated polymer composite actuator towards soft robotic gripper

6.1 Introduction

In this chapter, SMA wire based PDMS and polyimide soft composites have been developed and explored towards soft gripper and jelly fish robotic systems. The modelling of SMA wire embedded soft composite has been performed to evaluate the temperature generation during actuation. Then the fabrication procedure and performance characteristics of soft composites have been discussed in detail. Finally, the SMA/PDMS based soft robotic gripper and SMA/polyimide based soft jellyfish robot has been developed. The working and performance of these robots have been demonstrated.

6.2 SMA/PDMS soft composite actuator

The actuation behaviour of the SMA wire embedded Polydimethylsiloxane (PDMS) based soft robotic actuator has been investigated. SMA wire embedded PDMS based soft actuator has been developed using customized mold. The fabricated soft robotic actuator has been actuated through Joule heating under varying input current. In order to widen the displacement capabilities of the soft actuator, the SMA wire was pre-strained in the range 1% to 8% before being embedded in the soft matrix. Lifecycle analysis has been carried out. The thermal behaviour of the proposed actuator has been studied using COMSOL Multiphysics software. The proposed actuator can be used in soft robotic devices such as soft gripper, soft robotic manipulator, soft tentacles in biomimetic devices such as jellyfish, starfish etc.

6.3 Modeling of SMA/PDMS soft actuator

COMSOL Multiphysics, a finite element tool was used to simulate the heat distribution and the maximum surface temperature reached by the SMA wire embedded soft actuator during actuation. In order to determine the heat generation and the surface temperature of the SMA wire [94-96] embedded into the soft actuator, prebuilt heat transfer and electric currents module in COMSOL Multiphysics were coupled. The heat generation in the sample during the electricity supply is given by,

$$J = \sigma E \quad (6.1)$$

$$E = -\nabla V \quad (6.2)$$

Where J - Current Density, E - Electric Field, V- Electric potential.

The heat transfer due to conduction and convection is given by,

$$\rho C_p u \cdot \nabla T + \nabla \cdot q = Q \quad (6.3)$$

$$q = -k \nabla T \quad (6.4)$$

$$q = h_c A dT \quad (6.5)$$

Where ρ -density of the sample, C_p -specific heat, u -velocity of flow, k -thermal conductivity, A - exposed surface area and h_c -convective coefficient.

Fig. 6.1 shows the temperature distribution during the various currents 2 A, 4 A, 6 A and 8 A respectively. It clearly shows the increase in temperature with the increase in current.

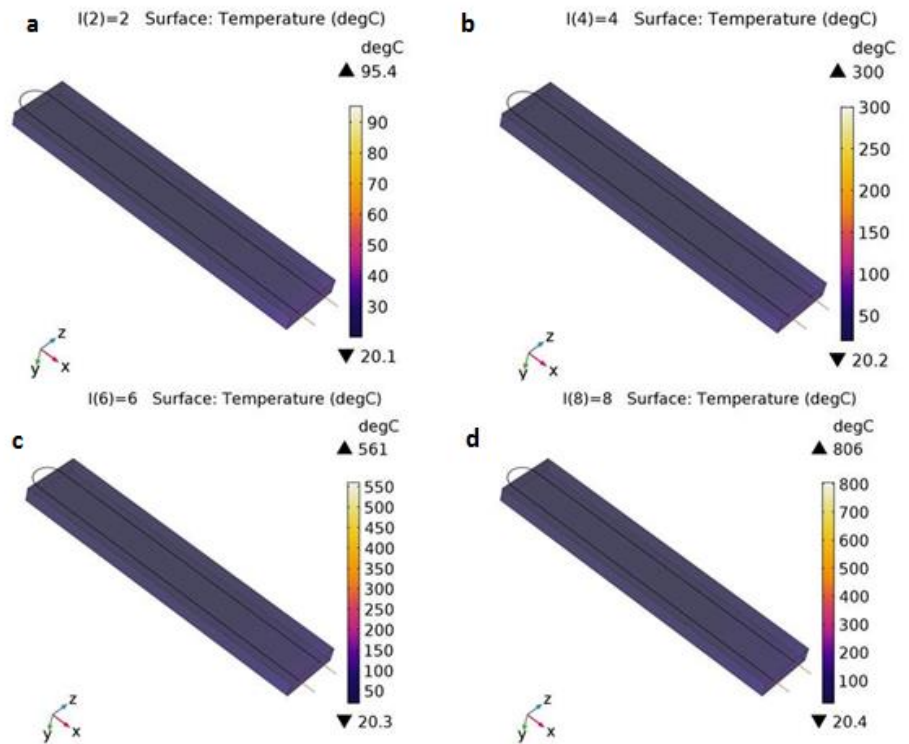


Fig. 6.1: Temperature distribution in the structure at a) 2 A b) 4 A c) 6 A d) 8 A

The surface temperature and average SMA wire temperature of the PDMS structure at different currents is shown in the Fig. 6.2.

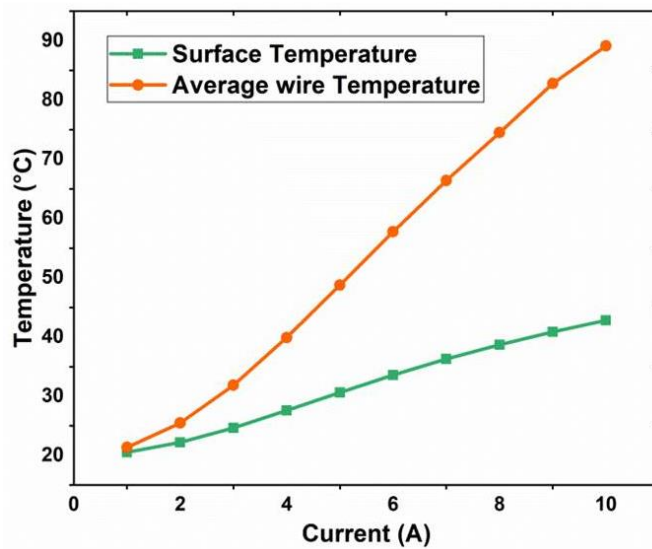


Fig. 6.2: Current vs. Temperature

The results from the simulations have been validated using a thermography camera (FLIR ONE thermal imager) image as shown in

Fig.6.3. During the input of various current, the thermography camera was used to capture the surface temperature of the PDMS soft structure. Table 6.1 shows the comparison of the simulation surface temperature data with the experimental thermography result for the input current. The data are in good agreement with each other.

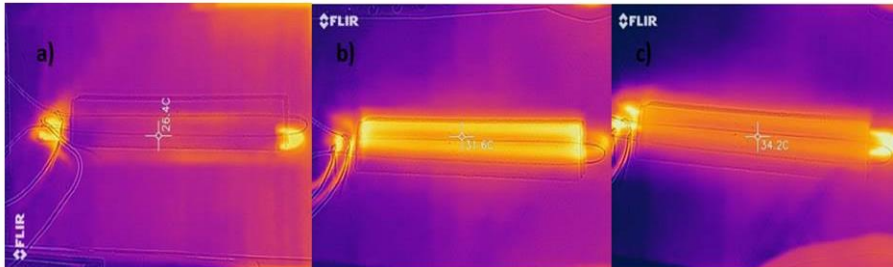


Fig. 6.3: Thermography image for the surface temperature at a) 4A
b) 6A c) 8A

Table.6.1: Validation of simulation with thermography image

S.No	Current (A)	Simulation value (°C)	Thermography value (°C)
1	4	27.59	26.4
2	6	33.58	31.6
3	8	38.68	34.2

6.4 Fabrication of the SMA soft actuator

The fabrication process of the proposed soft actuator is shown in Fig. 6.4. Fig. 6.4a shows the skeletal structure and CAD model of the proposed flat soft actuator in which the SMA wire is arranged. Fig. 6.4b shows the 3D printed mold to create the SMA embedded PDMS actuator. The commercially available Nickel Titanium (NiTi) SMA wire from Dynalloy Inc was used for the study

The property of PDMS and SMA wire is given in Table. 6.2 and 6.3 respectively.

Table.6.2: Properties of PDMS [97]

Parameter	Value
Young's modulus [MPa]	1.84
Tensile Strength [MPa]	6.7
Temperature range [°C]	-45 to 200
Thermal conductivity [W/m.K]	0.27
Cure time at 25°C [h]	48
Cure time at 100°C [m]	35

Table.6.3: Properties of SMA wire

Parameter	Value
Austenite start temperature [°C]	68
Young's modulus, Martensite phase [GPa]	28
Young's modulus, Austenite phase [GPa]	75
Poisson ratio	0.33

The mold is made of Acrylonitrile Butadiene Styrene (ABS). Fig. 6.4c shows the mold with SMA wire fixed in a pattern as shown in the skeletal structure using a custom-made arrangement. Fig. 6.4d shows the chemical structure of PDMS. The PDMS is available in the form of PDMS A and PDMS B (Resin and Hardener). The PDMS A and B are mixed in 10:1 ratio and stirred properly to avoid air bubbles as shown in Fig. 6.4e and f. The mixed PDMS solution is poured into the mould having properly spaced SMA wire. After pouring, the structure is cured at the temperature of 57°C for 8 hours as shown in Fig. 6.4g. After curing, the SMA embedded PDMS soft actuator is removed from the mold. The fabricated SMA embedded PDMS based soft actuator is shown in Fig. 6.4h. Fig. 6.4i shows the real image of the mold with SMA wire and PDMS. Fig. 6.5 shows the as fabricated soft actuator.

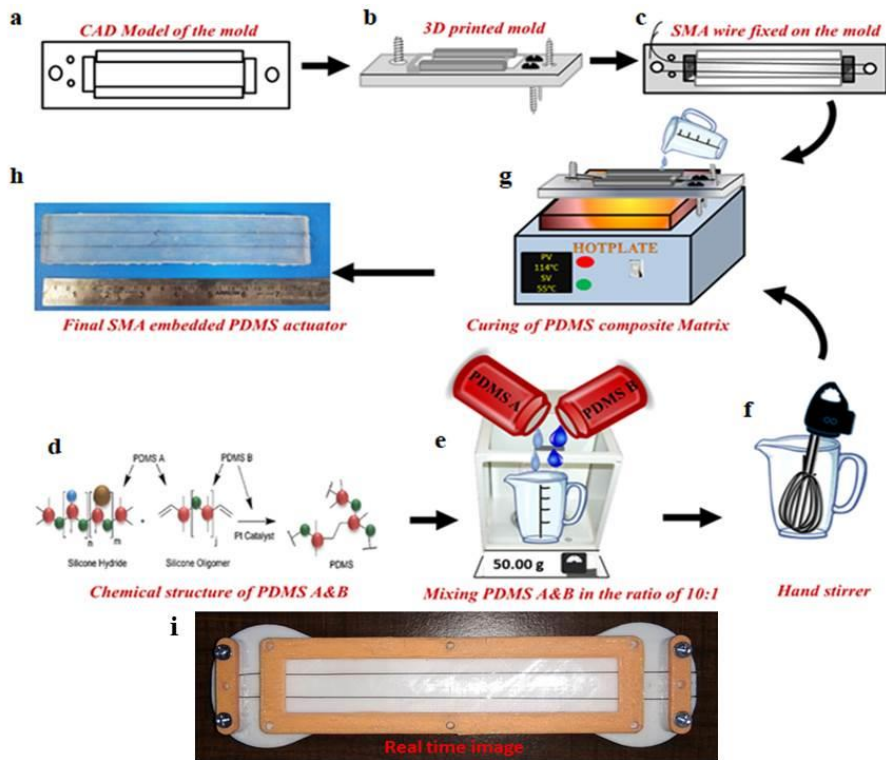


Fig. 6.4: Fabrication process of SMA based soft actuator



Fig. 6.5: Fabricated SMA/PDMS based soft actuator

6.5 Description of the experimental setup

An open loop control is adopted for actuating the SMA embedded PDMS actuator. The schematic diagram of the experimental setup is shown in Fig. 6.6. Joule heating method is adopted to actuate the SMA wire embedded PDMS actuator. The real time experimental setup is shown in Fig. 6.7.

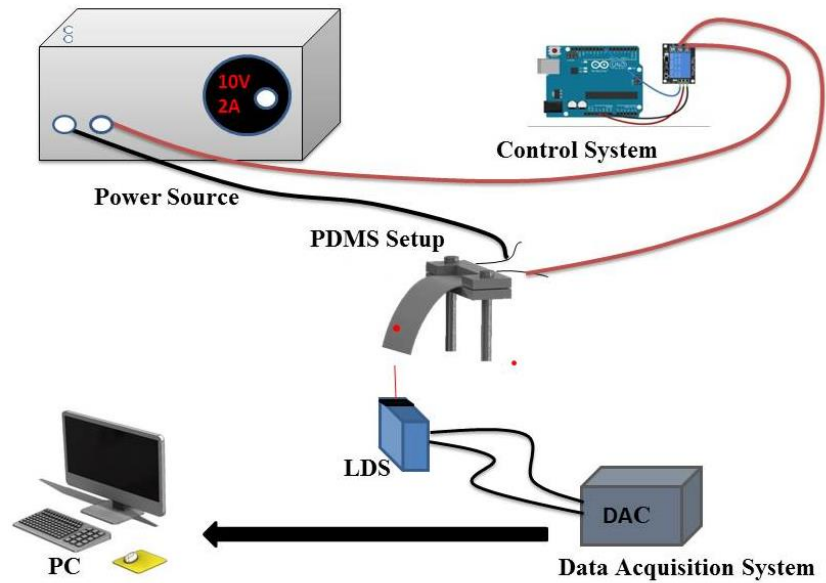


Fig. 6.6: Schematic of the experimental setup

The soft actuator has been fixed in the cantilever configuration. Because of its self-weight, the soft actuator bends at the free end. When the SMA wire has been fed with input current, the soft actuator will lift upwards. Laser displacement sensor (LDS) having $2.5 \mu\text{m}$ resolution was used to measure the displacement of the actuator during actuation. The signal from LDS is processed through a data acquisition system (NI C-DAQ) with LabVIEW setup. An Arduino board with relay circuit board is used to switch between the heating and cooling cycles.

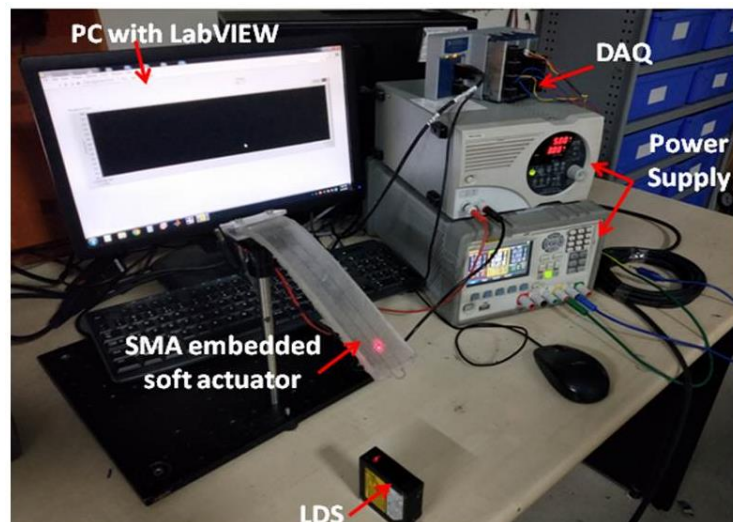


Fig. 6.7: Real time Experimental setup

6.6 Performance Evaluation

The performance of the actuation was experimentally investigated in terms of maximum displacement. In order to improve the displacement of the proposed soft actuator, the concept of pre-straining of the SMA wire was utilized.

6.6.1 Actuation Characteristics of the proposed soft structure

The actuation characteristics of the proposed SMA wire embedded PDMS structure have been investigated through Joule heating. The thermally activated behavior of the SMA wires was initiated by applying current to heat the SMA wires for transforming the phase of the alloy. During heating, the SMA wire reaches the austenite phase and it changes to the martensite phase upon cooling. To observe the displacement through joule heating, the soft structure is attached in cantilever configuration. The end tip displacement was measured at the free end of the actuator. The actuation of the proposed soft actuator is shown in Fig. 6.8. The input current has been varied from 1 A to 6 A and the respective maximum displacement have been measured using LDS. The maximum displacement of 7.5 mm has been observed at 2 A current. The displacement of the actuator is degraded with an increase in the current. This may be due to the accumulated heat in the PDMS matrix whose thermal conductivity is low. At higher input current the soft actuator attained at a permanent deformation as shown in the Fig. 6.9.

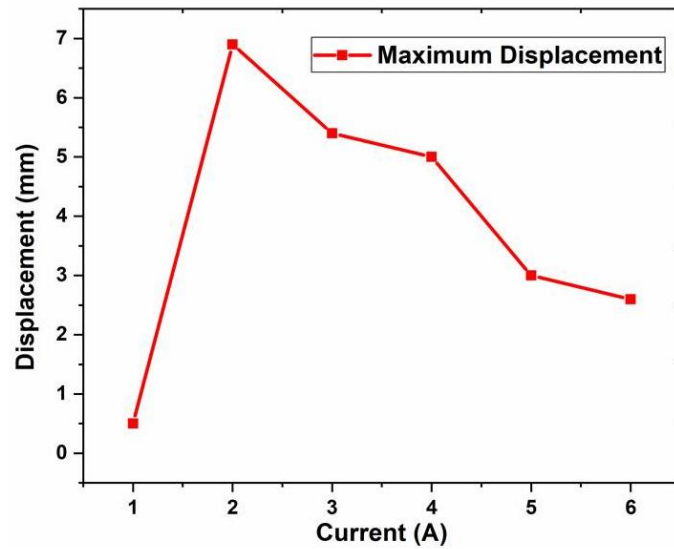


Fig. 6.8: Tip displacement of the soft actuator

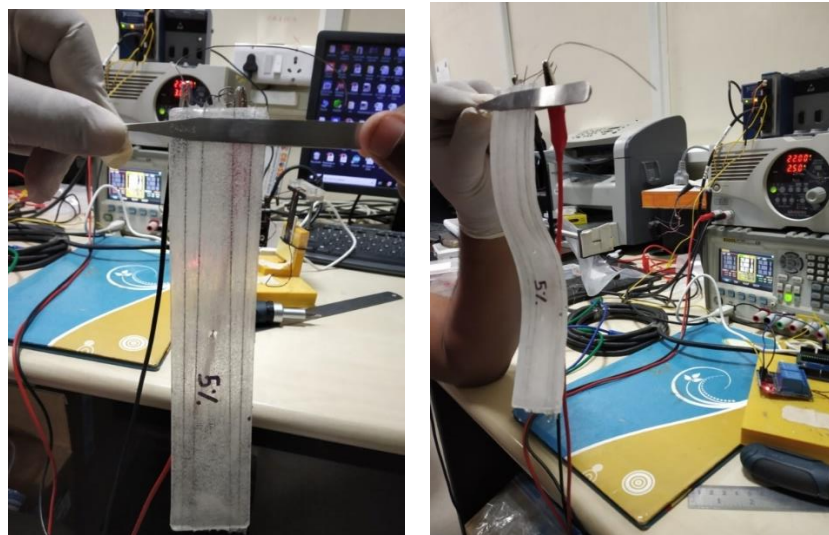


Fig. 6.9: Permanent deformation at higher current

The displacement during the actuation is plotted over the time for 2 A current as shown in Fig. 6.10. Each heating cycle was performed up to saturation of the displacement and followed by the cooling cycle until the soft structure returns to the initial position.

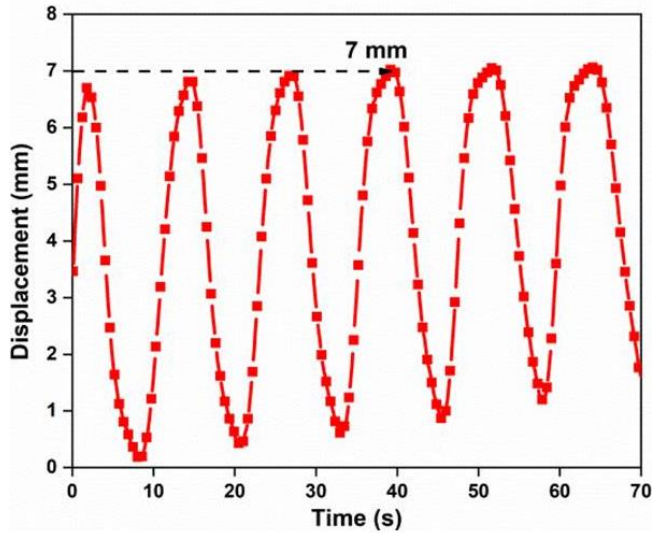


Fig. 6.10: SMA wire pre-straining effect on the soft structure

6.6.2 Effect of pre straining of SMA wire

The effect of pre straining of SMA wire on the proposed soft structure has been investigated. The SMA wire is strained from 1% to 8 % using universal tensile testing machine. The maximum displacement with respect to varying strain percentage has been observed as shown in Fig. 6.11. A maximum displacement of 21 mm has been obtained for 8 % strain. The pre-straining of the SMA wire increases the maximum displacement of the proposed structure than the SMA wire without pre-straining. This is due to the higher recovery required to overcome the induced strain. The SMA wire pre straining has worked quite well in the proposed design of soft actuator.

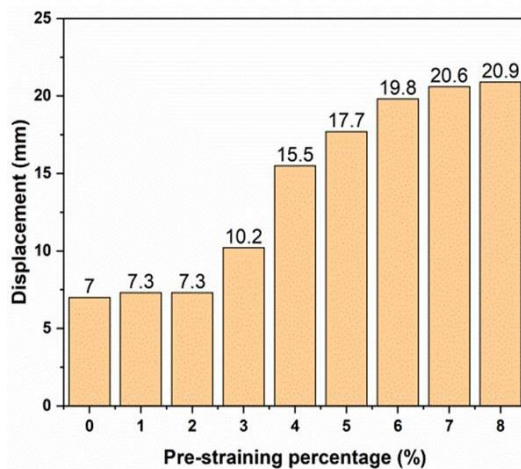


Fig. 6.11: Pre straining effect on displacement

6.6.3 Life cycle Analysis

To investigate the cyclic behavior of the developed soft structures, actuation analysis was performed up to 200 cycles. Based on the experience on SMA, we have found springs to be reliable as wires which lasts for more than million cycles at optimum electrical actuation conditions. The life cycle has been tested for 3 samples and the current of 2 A was selected for the investigations. The soft actuator has maintained an average displacement of 6 mm. Fig. 6.12 shows the displacement graph to analyze the cyclic behavior for 200 cycles. It is evident that the proposed soft structure maintained an average displacement for the entire duration. The maximum displacement of 6mm has been achieved. The plot shows a wavy pattern being generated every 500 seconds i.e. the displacement is not constant throughout the analysis. Since, the actuator is continuously running for more cycles, the PDMS matrix becomes more soften due to an increase in overall temperature. The prolonged exposure of heat generated by the SMA wire reduces the flexural rigidity of the actuator. Due to the reduction in flexural rigidity, the self-weight of the actuator would have induced a difference in sagging. The samples did not show any sign of failure even after 200 cycles.

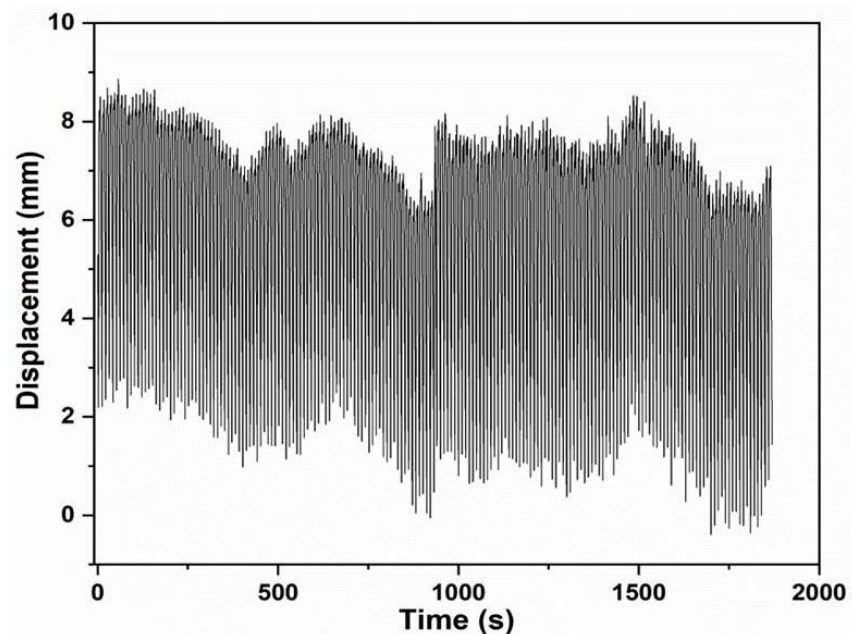


Fig. 6.12: Life cycle analysis of the proposed actuator

6.7 Development of SMA/PDMS based soft robotic gripper

Based on the above study, a soft robotic gripper has been developed and demonstrated. A two finger soft robotic gripper has been fabricated using the developed SMA/PDMS based soft actuator. The actuators are fixed in a holder setup to mimic the gripper mechanism. The complete gripper setup is shown in Fig. 6.13.



Fig. 6.13: SMA/PDMS based soft robotic gripper

The proposed soft gripper can be used as an end effector in the robotic pick and place application. The gripper holds the payload based on the gripping force generated by the soft actuator. When electrical energy is supplied to the soft actuator, the SMA wire produces the necessary gripping force for grasping the objects. Fig. 6.14 shows the falling of objects before the actuation of the gripper.

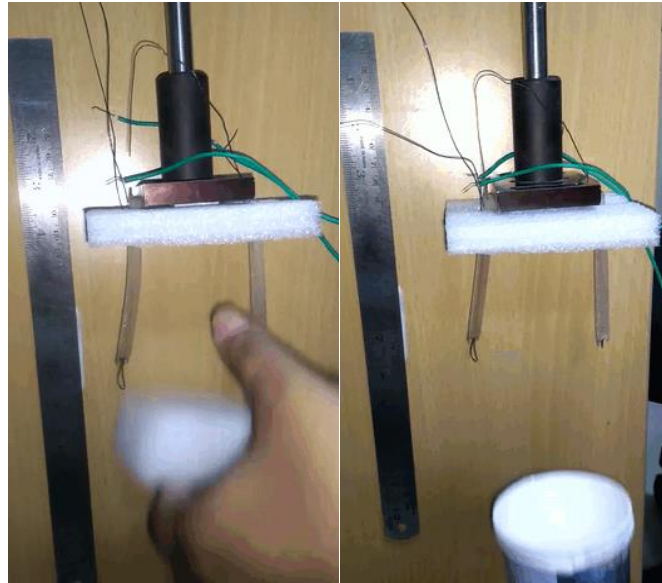


Fig. 6.14: Object falls down before the actuation of SMA/PDMS soft actuator

The gripper has been tested with different geometrical objects having a payload of 2.5 g to 7 g as shown in Fig. 6.15.

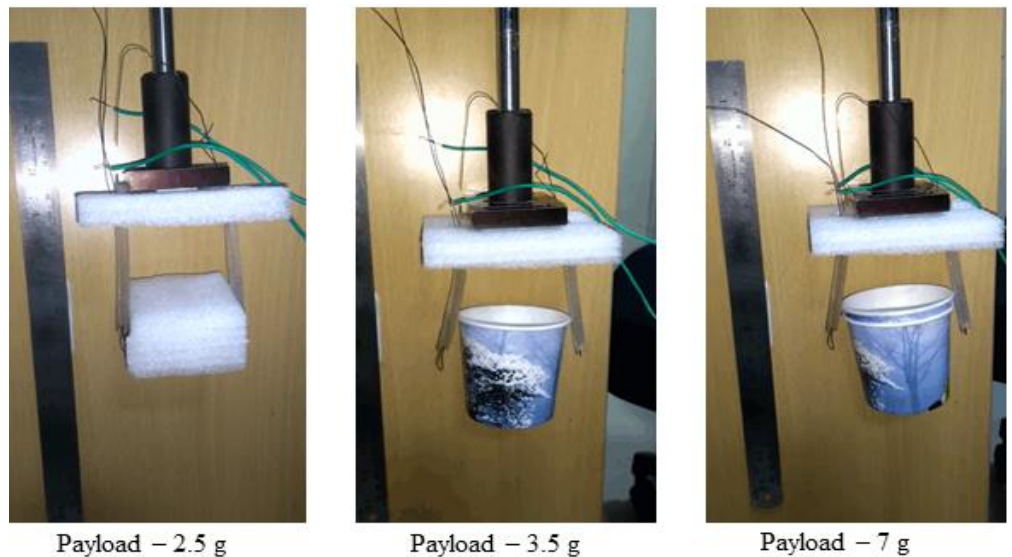


Fig. 6.15: Soft gripper demonstration with varying payload and different geometries

The gripper prototype can be improved by varying configuration (with 3 or 4 fingers) and increasing the volume of the SMA present in the soft gripper (diameter of the wire or number of wire strands can be increased) to increase the payload capacity.

6.8 Summary

A SMA wire embedded PDMS soft actuator has been developed and its thermo mechanical behavior has been investigated. The temperature distribution of the SMA/PDMS based soft actuator has been evaluated using COMSOL. The actuation characteristics with respect to varying input current have been investigated. The influence of pre-straining the SMA wire on the performance of the soft actuator has been explored in detail. The life cycle analysis of the SMA wire embedded PDMS based soft actuator has been demonstrated. Based on the investigations, a SMA/PDMS based soft gripper has been developed.

- A maximum surface temperature of 27.59 °C (Input current - 4 A) has been found through simulation and the same has been validated using thermographic camera.
- Through electrical actuation, the developed soft actuator showed a maximum displacement of 7.5 mm at 2 A current.
- The 8 % pre strained SMA wire embedded PDMS actuator showed a maximum displacement of 21 mm.
- The cyclic behavior analysis shows the average displacement of 6 mm has been maintained even after 200 cycles.
- The SMA/PDMS based soft gripper has demonstrated a payload capacity of 7 g

Chapter 7

Investigations on SMA wire integrated polyimide composite actuator towards soft robotic jellyfish

7.1 Introduction

In this chapter, a novel flexible polyimide based soft jelly fish robot actuated by SMA was fabricated and the pulse and recovery process of the jelly fish has been mimicked. The proposed structure is novel, cost effective and ease of fabrication with very less time consumption compared to conventional mold based methods. The behavior of the proposed jellyfish structure has been investigated with varying SMA wire diameter and frequency. The jellyfish tentacle displacement and velocity during mimicking was measured. The temperature modeling of SMA embedded structure and deflection modeling using beam bending theory has been performed. In addition, preliminary simulation of the jellyfish mimicking has been carried out in Ansys Fluent and the thrust force has been evaluated. The results show that the proposed method can be successfully applied to mimic the jellyfish locomotion and extended to underwater applications. The final prototype has been developed with an on board camera module and sonar sensor for object detection application with water tight PDMS bell structure. The robot has been tested underwater in a laboratory scale tank.

7.2 Modeling of the Polyimide/SMA tentacle

7.2.1 Kinematic modelling

The DH parameters for the proposed fish were obtained from the frame diagram as shown in Fig. 7.1. Table 7.1 shows the DH parameters for the tentacle.

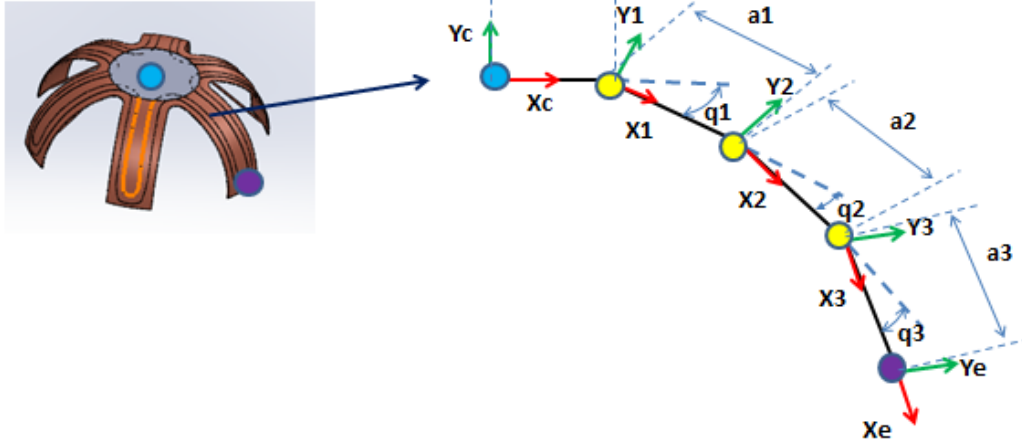


Fig. 7.1: Kinematic configuration of tentacle

The individual homogeneous transformation matrices are obtained from the DH Table. The number of independent kinematic parameters are θ_1 , θ_2 and θ_3 .

Table.7.1: DH parameter table

i	Alpha	A	d	Theta
1	0	a0	0	q1
2	0	a1	0	q2
3	0	a2	0	q3
4	0	a3	0	0

The individual homogeneous matrices were multiplied to get the final homogeneous transformation matrix T.

$$\mathbf{T} = \begin{bmatrix} c(1+2+3) & -s(1+2+3) & 0 & a0 + a2c(1+2) + a1c(1) + a3c(1+2+3) \\ s(1+2+3) & c(1+2+3) & 0 & a2s(1+2) + a1s(1) + a3s(1+2+3) \\ 0 & 0 & 1 & 0 \\ 0 & 0 & 0 & 1 \end{bmatrix} \quad (7.1)$$

The dynamic model for the tentacle has been derived using Newton Euler method and the model has been simulated with the desired trajectory as shown in Fig. 7.2. The desired trajectory is the oscillation of the tentacle during actuation.

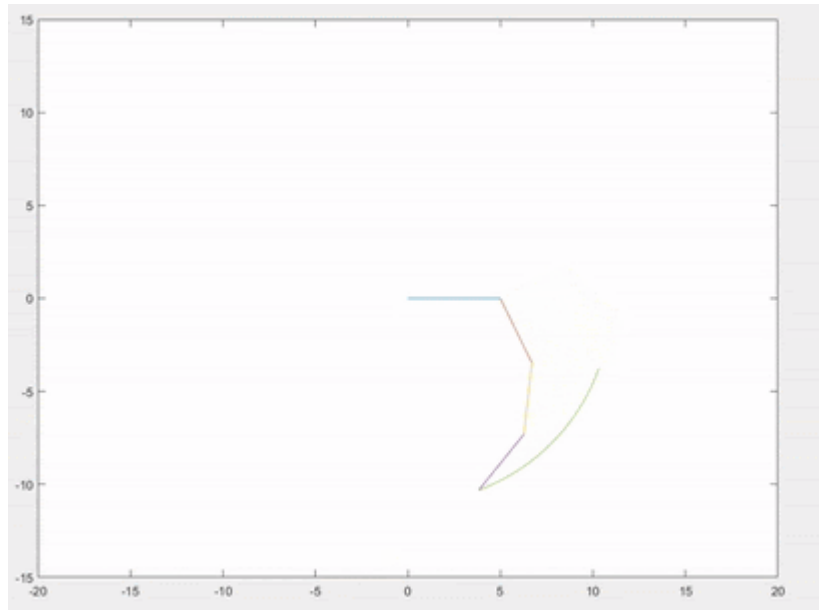


Fig. 7.2: Tentacle dynamic simulation as 3 link manipulator

The tentacle oscillation has been visualized in ADAMS as well as shown in Fig. 7.3. From the ADAMS simulation, the tip displacement and velocity has been observed.

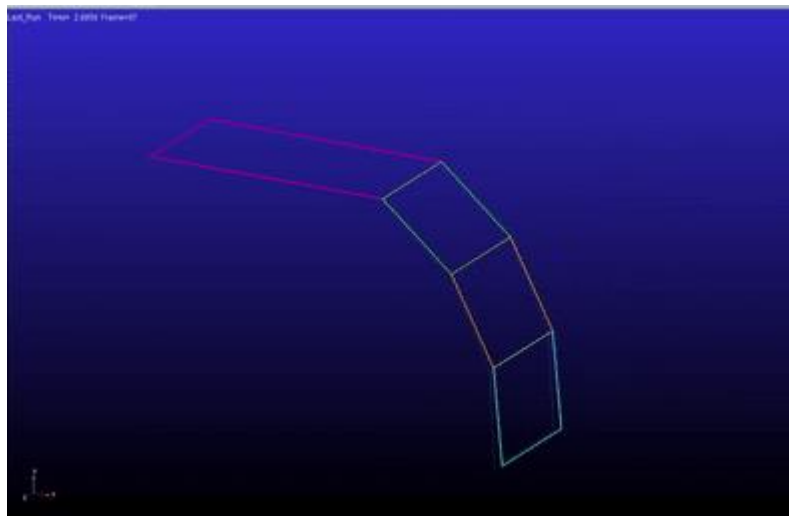


Fig. 7.3: Tentacle dynamic simulation using ADAMS

7.2.2 Modeling of SMA wire temperature in tentacle

In order to understand the temperature induced with SMA wire during heating, it has been modeled and simulated. The shape memory effect is achieved by passing a current through the wires which increases its temperature due to Joule heating. Once the SMA wire reaches the high temperature austenite phase, the wire is allowed to cool under the conduction and convection effect of water. Cyclic current is passed to

achieve the flapping of tentacles. A single tentacle is considered to model the variation of temperature of the wires with time.

The heat balance equation is:

$$\dot{q}_{gen} = \dot{q}_{stored} + \dot{q}_{conv} \quad (7.2)$$

Where q is heat; \dot{q} is rate of heat transfer; \dot{q}_{gen} = rate of heat generation due to Joule heating; \dot{q}_{stored} = rate of heat energy stored in SMA wire; \dot{q}_{conv} = rate of heat transfer to the water due to convection and conduction.

$$\dot{q}_{gen} = I^2 R \quad (7.3)$$

$$\dot{q}_{stored} = mS \frac{dT}{dt} \quad (7.4)$$

$$\dot{q}_{conv} = \frac{hA(T - T_{inf})}{\Delta t} \quad (7.5)$$

T_{inf} = temperature of the water

T = Temperature of the SMA wire

Given the heat balance equation:

$$I^2 R - hA(T - T_{inf}) = mS dT/dt \quad (7.6)$$

By integrating the heating equation:

$$T = (C + T_{inf}) - (C - (T_i - T_{inf})) * e^{-hAt/mS} \quad (7.7)$$

T_i = Initial temperature of the SMA wire. Where

$$C = I^2 R / hA \quad (7.8)$$

For the cooling equation, put $I=0$ in the heat balance equation and integrate:

$$T - T_{inf} = (T_i - T_{inf}) * e^{-hAt/mS} \quad (7.9)$$

The initial temperature of the wires is assumed to be the room temperature (25°C) and the highest temperature up to which the wires are allowed to heat is 65°C (Austenite finish temperature). Wires are cooled due to the convection effect of water till 30°C and the cycle continues. The parameters used for the simulation are given in Table 7.2.

Table.7.2: Parameters used for simulation

Parameter	Description	Value
I	Current passed through the wire	2 A
R	Resistance of the wire	4.67 Ω
M	Mass of the wire	0.507 g
S	Specific heat of the wire	0.3218 J/g°C
H	Convection heat transfer coefficient	460.97 J/m ² K
A	Effective area over which heat transfer is happening	0.00041 m ²
ρ	Density	991 Kg/m ³
M	Dynamic viscosity	6.1 x 10 ⁻⁴ Kg m ⁻¹ s ⁻¹
K	Thermal conductivity of water	0.63
L	Length of tentacle	100 mm

The temperature on the SMA/polyimide structure has been modeled. The variation of temperature with respect to different current input has been simulated and plotted in Fig. 7.4. The temperature increases and the heating time reduces with an increase in current. A maximum of 86.5°C has been observed at an input current of 10 A.

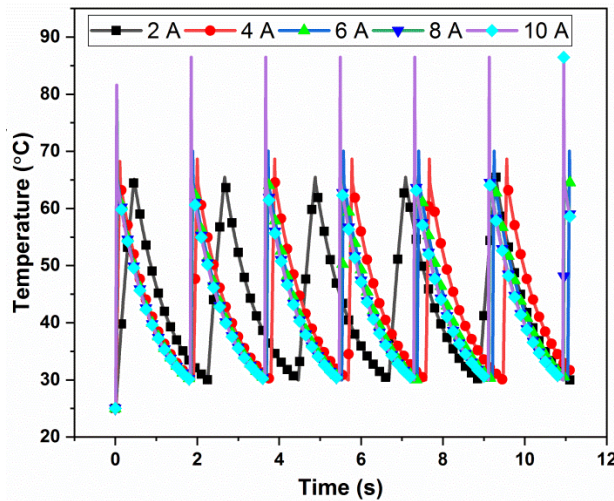


Fig. 7.4: Variation of SMA wire temperature with current

7.2.3 Beam Bending Theory

The individual tentacle with ends fastened with an elastic rubber string is considered as a beam for modeling. Initially, the tentacle is assumed as a straight beam and after fastening with rubber string it swirls due to the bending moment experienced by the beam [28]. Fig. 7.5 shows the schematic of the model. It is clear that the rubber string is under tension as the beam is trying to restore its shape and rubber string is restricting the restoration. Therefore the tensile force (F) being experienced by the rubber string of stiffness (k) is given by

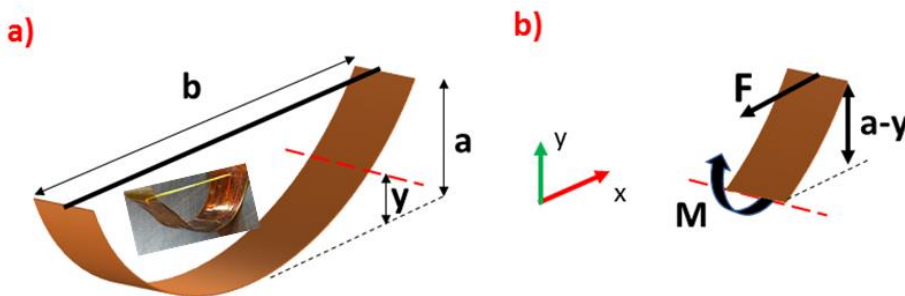


Fig. 7.5: Schematic of the model that extracts the bending moment (inset showing the actual image of the tentacle)

$$F = k * \Delta x \quad (7.10)$$

Where Δx is the extension in the rubber string due to tensile force F , given by

$$\Delta x = b - nl \quad (7.11)$$

b is the length under tension while nl is the length of the rubber string at no load condition. Now substituting the value of Δx in equation (7.10) results in

$$F = k * (b - nl) \quad (7.12)$$

Since the structure is symmetric, the model of one half is considered. Using Euler Bernoulli equation, it is known that curvature of a beam at any point is proportional to bending moment at that point and is given by the relation

$$\frac{M}{E * I} = \frac{1}{r} \quad (7.13)$$

Here $1/r$ is the curvature at that point, M is the bending moment, E is the elasticity modulus and I is the second moment of area of the cross section with respect to a centroidal axis perpendicular to the plane of the couple M . Mathematically for a curve $y=f(x)$ curvature at a point is given by

$$\frac{1}{r} = \frac{\frac{d^2y}{dx^2}}{\left(1 + \left(\frac{dy}{dx}\right)^2\right)^{\frac{3}{2}}} \quad (7.14)$$

Therefore, by combining (7.13) & (7.14) curvature at any point is given by the following expression

$$\frac{M}{E * I} = \frac{\frac{d^2y}{dx^2}}{\left(1 + \left(\frac{dy}{dx}\right)^2\right)^{\frac{3}{2}}} \quad (7.15)$$

In the above equation E & I are known (E is a property of material, I is the property of the cross-section). The only unknown is bending moment M . In order to determine M , a part of the beam is taken by making a partition at an arbitrary point. The free body diagram of the beam section is analyzed. On the upper end, the tension of the rubber string is the only force acting on it. Since the section is in equilibrium,

an equal and opposite force will be acting on the lower end. Also, these two forces have resulted in a couple generating a moment $F*(a-y)$. To maintain equilibrium, this moment will be balanced by internal equivalent opposite moment is given by

$$M = F * (a - y) \quad (7.16)$$

M represent the bending moment being experienced by the beam at any y. Substituting this value in the equation (7.15) will result in the following differential equation

$$\frac{F * (a - y)}{E * I} = \frac{\frac{d^2y}{dx^2}}{\left(1 + \left(\frac{dy}{dx}\right)^2\right)^{\frac{3}{2}}} \quad (7.17)$$

And the value of F can be substituted from the equation, resulting in the following differential equation representing our system

$$\frac{k * (b - nl) * (a - y)}{E * I} = \frac{\frac{d^2y}{dx^2}}{\left(1 + \left(\frac{dy}{dx}\right)^2\right)^{\frac{3}{2}}} \quad (7.18)$$

As the differential equation is of 2nd order, it requires 2 boundary conditions to solve for the solution. The boundary conditions are

$$y(0) = 0 \quad (7.19)$$

$$\frac{dy}{dx} (at x = 0) = 0 \quad (7.20)$$

The 2nd order non-linear differential equation is solved numerically in MATLAB.

The young's modulus is different at high temperature austenite phase and low temperature martensite phase. Based on the modulus variation during phase change, the SMA/polyimide structure deflection varies. This deflection with respect to change in modulus has been modeled and simulated. The deflection plot with respect to modulus is shown in Fig. 7.6. A deflection of 30° angle was observed from the model.

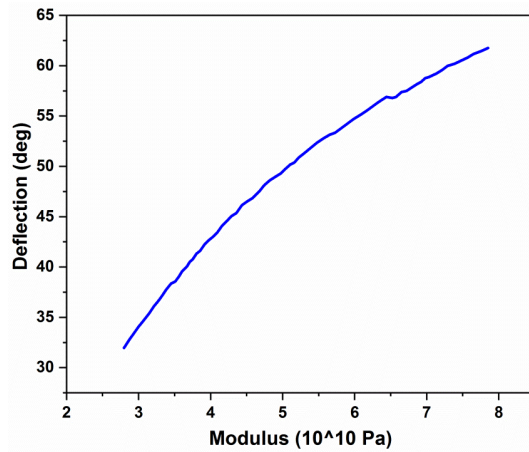


Fig. 7.6: Tentacle deflection

7.2.4 Hydrodynamic Analysis

In order to validate the proposed design, a preliminary hydrodynamic analysis has been performed. ANSYS Fluent coupled with transient structural is used to simulate the actuation of bio-inspired jellyfish in the static flow field.

Fig. 7.7a shows the pressure variation during contraction (more yellow and red color depicts relatively high pressure regions). The creation of high pressure regions on the back provides the required thrust force for the jelly fish to move forward. Fig. 7.7b shows the pressure variation during expansion. The low pressure inside the body provides a backward push to the fish. This should be less than the forward push generated during contraction to have a net forward push. Here, the high pressure region produced during the expansion is not comparably significant and results in a net forward movement.

Vortex formation also plays a major role in the propulsion of fish; Fig. 7.7c depicts the vortex formation and its location in the fluid domain. At the end of tentacles, one face is on high pressure and the other is at low pressure. This led to a flow of fluid particle around the tip and develops into a vortex. The vortex propagates in the opposite direction of fish and higher density streamlines at the back depict the higher

speed of fluid moving out from the end (jet propulsion). Hence, the pressure variation and vortex propulsion helps the developed jellyfish to navigate in the water.

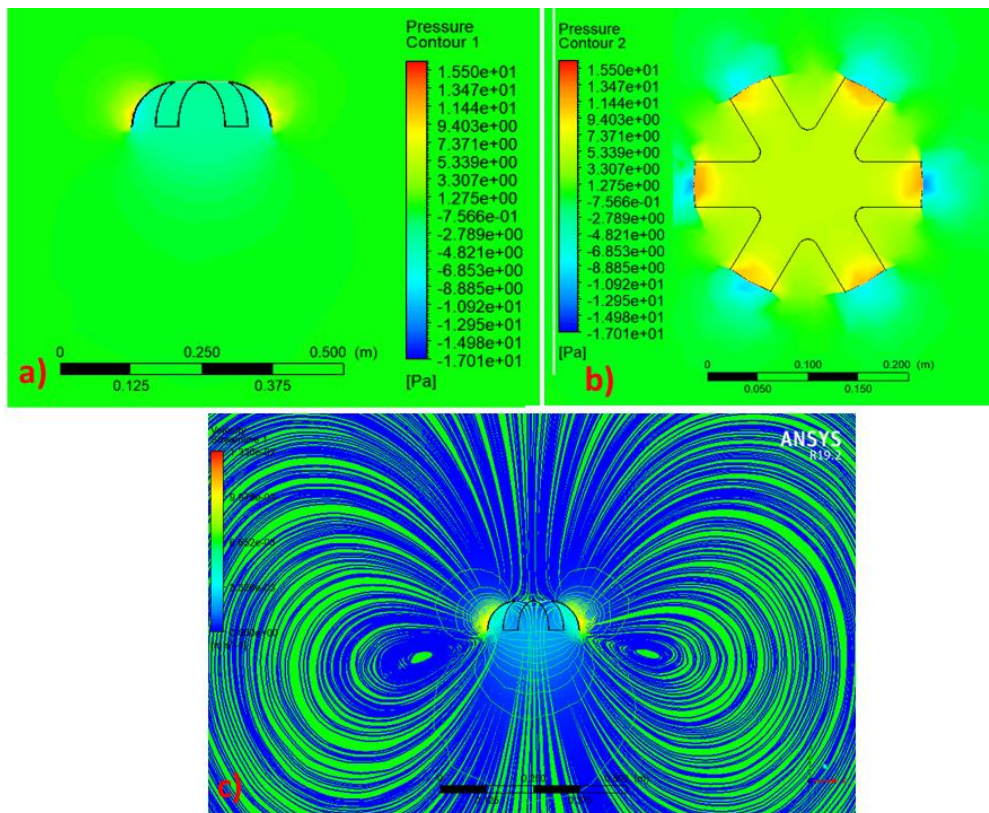


Fig. 7.7: a) Pressure contours during bell contraction, b) Pressure contours during bell expansion and c) vortex formation visualized via streamlines

Initially, when the current is passed, the bell structure will expand against the force of the rubber string and push the water above it. As a reaction force in the opposite direction, it can be seen as negative thrust force values in Fig. 7.8. When current is cut off, it will contract back to its natural position due to the elastic force of the rubber string. During contraction, it will push water inside the bell structure and results in a positive thrust to the fish in the form of reaction force. A negative thrust is going to push the fish in the backward direction and positive thrust is going to move it forward. A maximum thrust force of 0.5 N has been recorded for the movement of jellyfish.

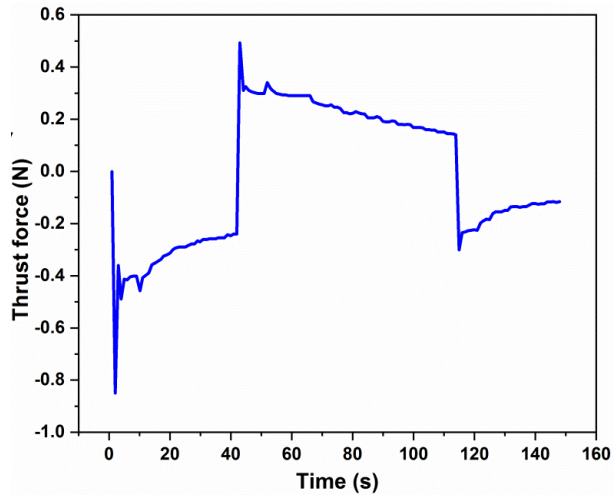


Fig. 7.8: Thrust force

7.3 Fabrication of the robot skeletal structure

Kapton polyimide sheets of 75 μm thickness have been taken and cut into jellyfish like symmetric structure as shown in Fig. 7.9a and b. The diameter of the symmetric structure was 25 cm. The holes were punched in the appropriate positions to hold the SMA wires. Then the nitinol SMA wires were inserted into the polyimide sheets as shown in Fig. 7.9c. The commercially available Nickel Titanium (NiTi) SMA springs from Dynalloy Inc was used for the study. Finally, the Kapton polyimide tape of thickness 30 μm was pasted and thus the SMA wire was affixed in-between the polyimide sheet at the bottom and polyimide tape on the top as shown in Fig. 7.9d. A rubber string was attached between the tentacle ends and centre of the body to achieve the recovery motion. The schematic and actual image of the bell structure with attached rubber strings is shown in Fig.7.9e and f. The weight of the skeletal structure of the fabricated jellyfish was 45 g only. Light weight and thin composite structures of any shape can be easily developed using this fabrication procedure in a short period of time. These structures will be desirable for soft robotic applications due to profound features such as low cost, high flexibility, and repeatability.

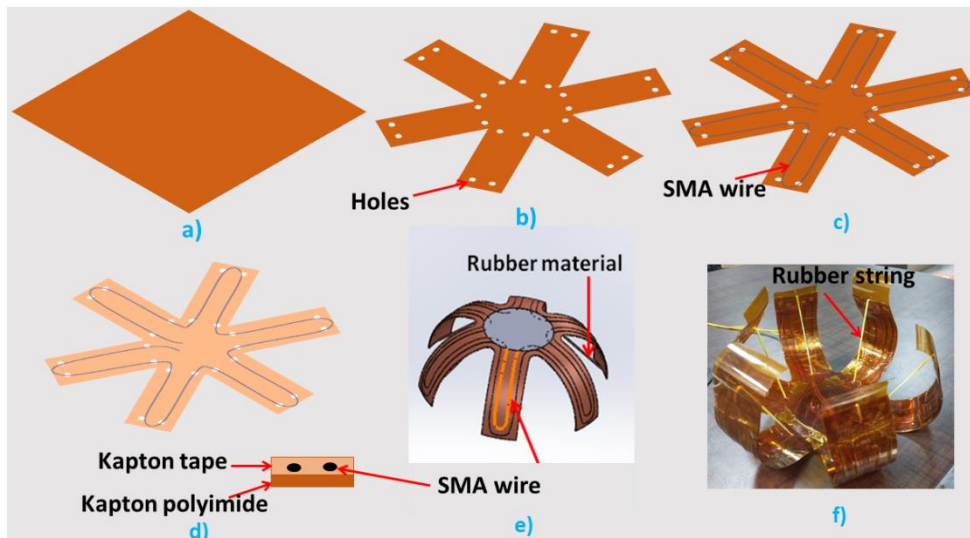


Fig. 7.9: Fabrication process of the proposed soft robotic jellyfish a)

Kapton polyimide sheet, b) carved out jelly fish shape with holes punched in it, c) SMA wires are inserted into the holes, d) Kapton tape is pasted over the SMA wires (inset showing the cross section of the composite structure), e) and f) schematic and actual image of the bell structure with attached rubber strings

7.4 Performance Evaluation

7.4.1 SMA effect on the proposed jellyfish

At rest, the jelly fish remains in the contracted position. When the SMA wire is actuated through Joule heating, the tentacles of the jelly fish expand. During cooling, the jellyfish returns to the contracted shaped structure due to the elasticity of rubber string.

In order to analyse the SMA effect on the proposed structure, the SMA wire diameter has been varied and its effect on tip displacement has been evaluated. The 4 different SMA wire diameters were taken as 0.15 mm, 0.25 mm, 0.3 mm and 0.5 mm. The displacement of the various wire diameter tentacles has been measured through LDS shown in Fig.7.10. Wire diameter having 0.5 mm showed a maximum displacement among others. The 0.5 mm diameter has been chosen for further experimentation of jellyfish.

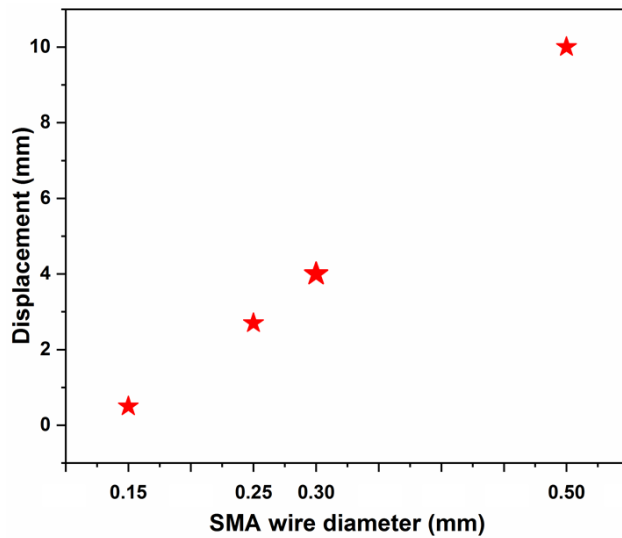


Fig. 7.10: Tentacle displacement with varying SMA wire diameter

The actuation behavior of SMA depends on the ambient conditions (medium and its temperature) due to the change in heating and cooling rates. The water temperature influence the flapping of the jellyfish tentacle. Fig. 7.11 shows the thermal imaging of heat flow in SMA wires recorded using FLIR camera. It has been observed that the SMA wire temperature has increased from 31.2⁰C to 49.9⁰ C and enabled the actuation.

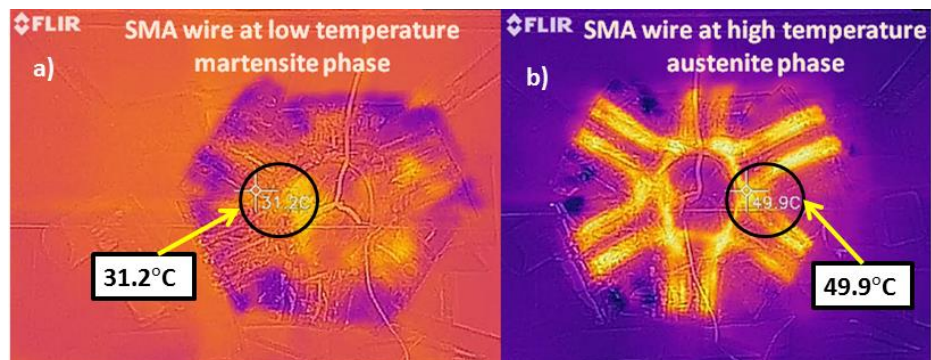


Fig. 7.11: Thermal images of FLIR Camera

7.4.2 Investigations on displacement and bending

The investigation on the tip displacement of the jellyfish tentacle has been observed through LDS. The displacement has been measured at three different frequencies as 0.5 Hz, 1 Hz and 2 Hz (Fig. 7.12). During the investigation, the jellyfish is kept static. A maximum

displacement of 15.3 mm at 0.5 Hz and a minimum displacement of 6 mm at 2 Hz has been recorded. The minor fluctuation in the displacement cycle may be attributed to the hysteresis behavior of the SMA wire.

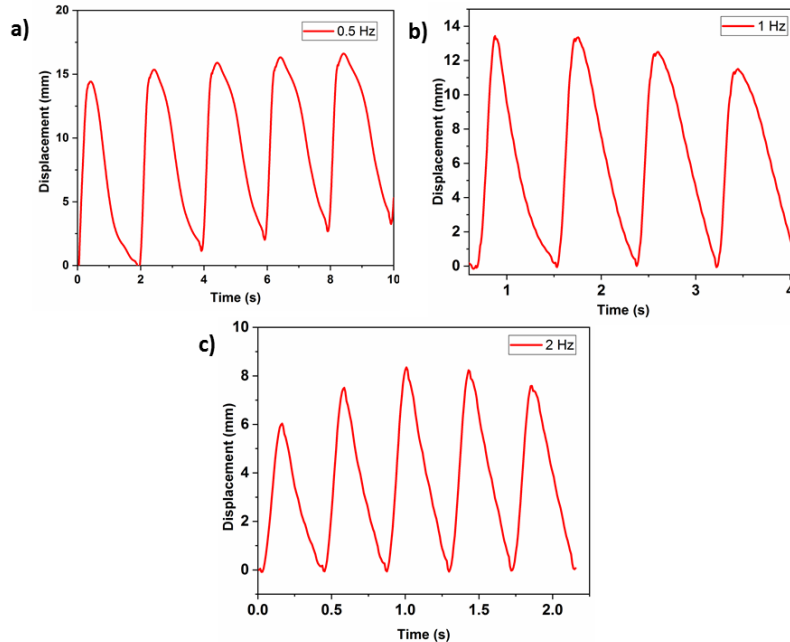


Fig. 7.12: Frequency of tentacle **a)** 0.5 Hz **b)** 1 Hz **c)** 2 Hz

In order to analyse the bending characteristics of the individual tentacle, flex sensor have been attached to it as shown in Fig. 7.13a. Through flex sensor, the individual bending angle of the tentacle was obtained. The corresponding bending angle of the tentacle from its initial position to the expanded position is around 40° . The time vs bending angle has been plotted as shown in Fig. 7.13b. The bending angle has been taken for 2 cycles of the flapping action from an individual tentacle.

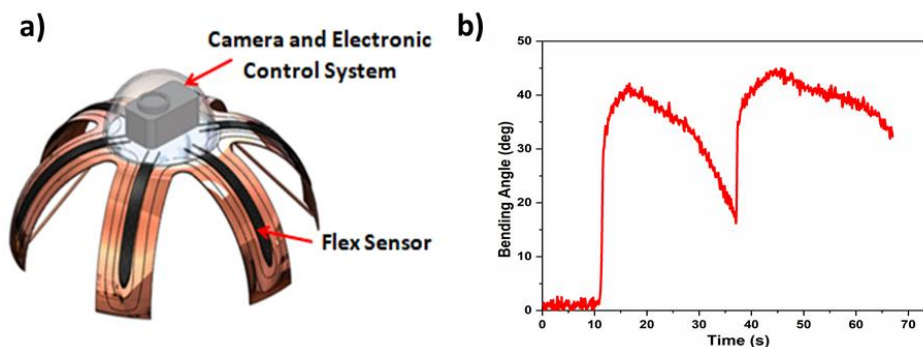


Fig. 7.13 (a) Proposed Jellyfish with Camera, Sensors and Electronic Control System **(b)** Tentacle bending angle

7.4.3 Thrust Measurement

The thrust force is measured in a water tank with a load cell arrangement. A load cell was connected to the top side of the jellyfish robot structure via a rod as shown in Fig. 7.14. During the actuation of the jellyfish, the measured thrust was 0.3 N.

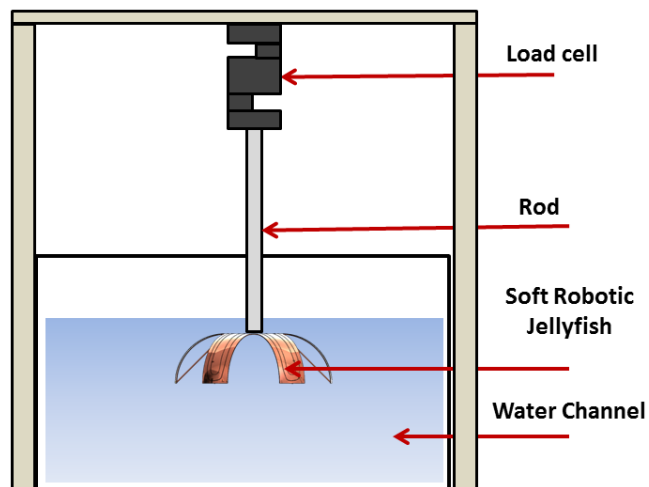


Fig. 7.14: Thrust force measurement setup

7.4.4 Movement of Robotic jellyfish

The jellyfish robot has been tested in a water channel at the laboratory. The dimension of the water tank is 60 cm × 65 cm × 45 cm. The robot has been tested to float at an angle.



Fig. 7.15: Position of jellyfish at different time instances

To enable floating and mimic the movement of jellyfish, the operating current and frequency of the tentacles have been optimized at 8 A and 0.5 Hz respectively. The cyclic heating/cooling of the SMA wire along with the rubber string creates pulse and recovery motion of the tentacles. These actions generate the necessary thrust force to move the jelly fish forward at a velocity of 10 mm/s. Fig. 7.15 shows the still sequence of the jellyfish motion at horizontal orientation. The water temperature during the experimentation was 25⁰ C.

Fig.7.16 shows the still sequence of the jellyfish motion at a vertical orientation. To enable this orientation, a payload of 50 g has been attached to the robot to sink underwater. In this orientation, the jellyfish has moved at a velocity of 0.2 mm/s.

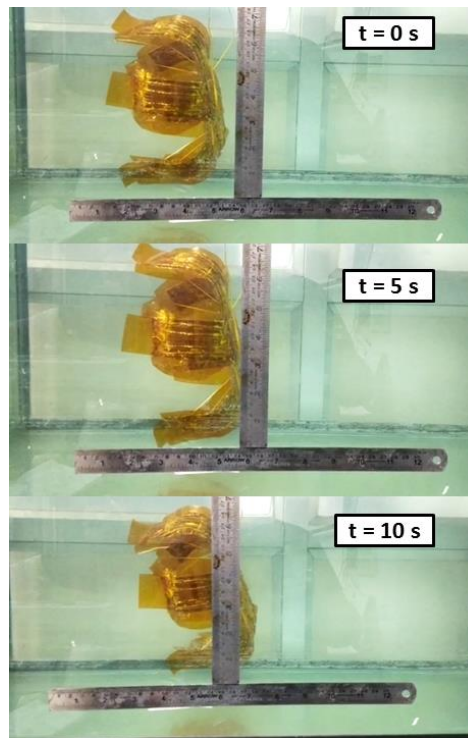


Fig. 7.16: Position of jellyfish at different time instances in vertical orientation

Further, the skeletal structure has been tested with onboard electronics which consists of arduino board, relays and battery. The onboard electronics covered with 3D printed bell structure and tested underwater as shown in Fig. 7.17-7.19. Here, the rubber string which helps in achieving the contraction motion was replaced with appropriate bias loads attached to the end of the tentacle. A maximum frequency of 2 Hz has been achieved for the tentacle motion. For the required frequency of tentacle motion, the weight of the bias loads or the stiffness of the rubber string has to be suitably selected.

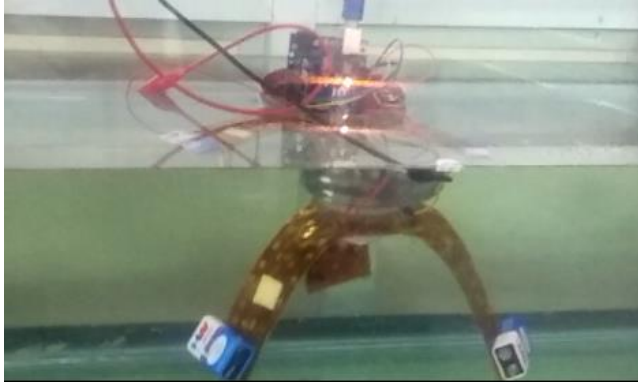


Fig. 7.17: Experimentation of jellyfish robot with bias load

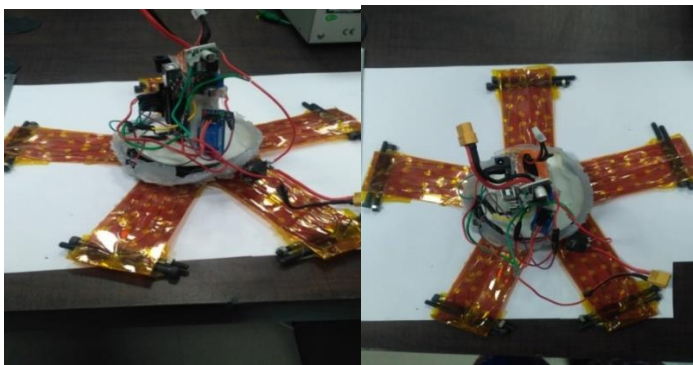


Fig. 7.18: Experimentation of jellyfish robot with bias load and onboard electronics

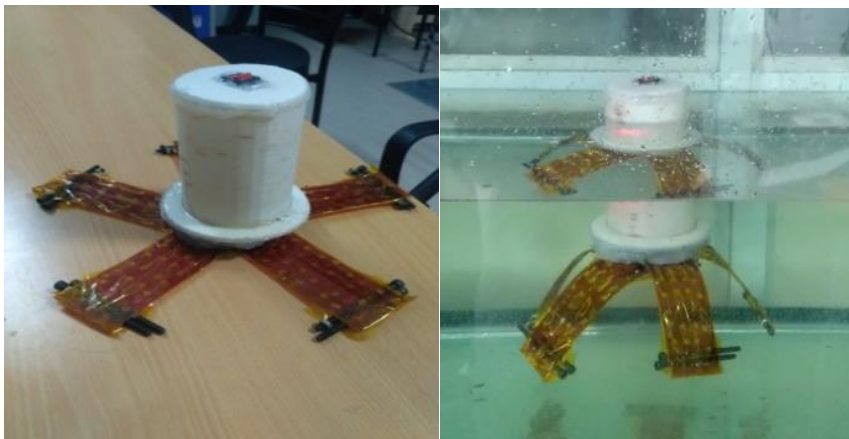


Fig. 7.19: Experimentation of jellyfish robot with bias load with on onboard electronics covered with 3D printed bell structure

In order to reduce the weight of the final robot, the bell structure shaped enclosure was fabricated using PDMS and attached to the top of the polyimide/SMA tentacle structure (Fig. 7.20). The onboard electronics and the camera module have been kept inside the air tight

PDMS bell. On top of the PDMS bell, a sonar sensor is attached which can be rotated.

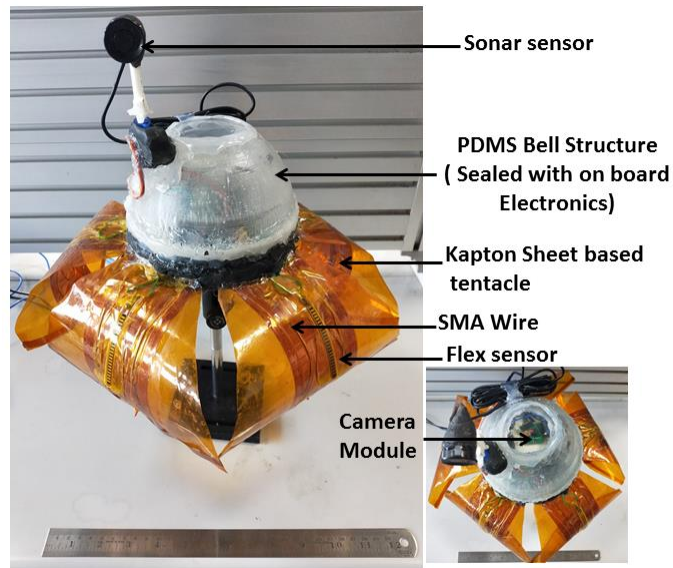


Fig. 7.20: SMA/polyimide based jellyfish prototype for underwater object detection

7.5 Summary

A simple and effective method for fabricating SMA wire based soft robotic actuator has been implemented. The temperature and deflection of the SMA/polyimide tentacle has been modeled and simulated with respect to the various input current. A preliminary hydrodynamic analysis has been performed using ANSYS in the static flow field. In order to analyze the SMA effect on the proposed structure, the SMA wire diameter has been varied and its effect on tip displacement has been evaluated. A bio-inspired polyimide based soft jellyfish robot has been fabricated and actuated with SMA wires for mimicking the locomotion of jellyfish in both horizontal and vertical orientation. A final jellyfish prototype has been developed with onboard electronics and camera module covered with air tight PDMS structure.

- A maximum displacement of 15.3 mm at 0.5 Hz and minimum displacement of 6 mm at 2 Hz has been recorded.
- The maximum temperature of 49.9 °C and a maximum deflection of 42° have been achieved.
- A thrust force of 0.5 N and 0.3 N has been observed in simulation and experiment respectively.
- The robotic jellyfish has moved at a velocity of 10 mm/s and 0.2 mm/s in horizontal and vertical orientation respectively.
- A final jellyfish prototype has been developed with onboard electronics and camera module covered with air tight PDMS structure.

Chapter 8

Conclusions and Future Scope

The results of the work can be summarized as follows

8.1 SMA spring based Bio-inspired soft meshworm

- The thermal simulation SMA spring has recorded a maximum temperature of 113 °C. The spring has taken 20 s to reach the saturation temperature and 80 s to return to normal position.
- In thermo mechanical analysis, at 1.5 N, a maximum displacement of 3.9 mm was observed. The loads 2.5 N and 3.5 N have produced a maximum displacement of 7.54 mm and 9.17 mm respectively.
- Maximum bending angles of 50° to 60° showed maximum recovery of 57%. At 8% duty cycle (4.8 s heating time), the bending has reached almost 55°
- In peristaltic crawling, a bending angle of 57°, 48°, and 48° is achieved in upward, left, and right directions respectively.
- In two anchor crawling, a bending angle of 60° is achieved in the downward direction
- During laser actuation, a minimum and maximum displacement of 10.1 mm and 28.9 mm has been obtained at 20 W and 50 W respectively.

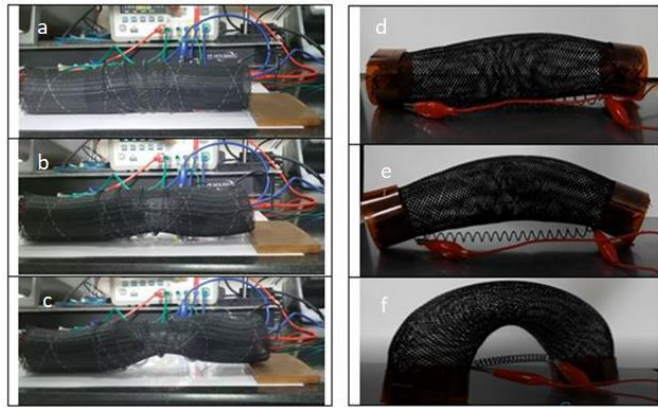


Fig. 8.1: Prototype of SMA spring based soft meshworm

8.2 SMA spring based bio-inspired robotic fish

- ADAMS analysis of the fish fin oscillation was visualized at a frequency of 0.1 and 0.5 Hz. A maximum fin displacement of 35 mm and 20 mm has been observed at 0.1 and 0.5 Hz respectively.
- A maximum displacement of 15 mm during the caudal fin undulation has been recorded experimentally at 0.5 Hz.
- In the air medium, a maximum angle of 51° on the right side and 50° on the left side was achieved. Whereas in the water medium, a maximum angle of 50° on the right side and 49° on the left side was attained.
- Force produced during the fin oscillation is measured and maximum force of 0.39 N at 0.1 Hz is obtained.
- The developed robotic fish achieved a steady swimming at velocity of 24.5 mm/s.

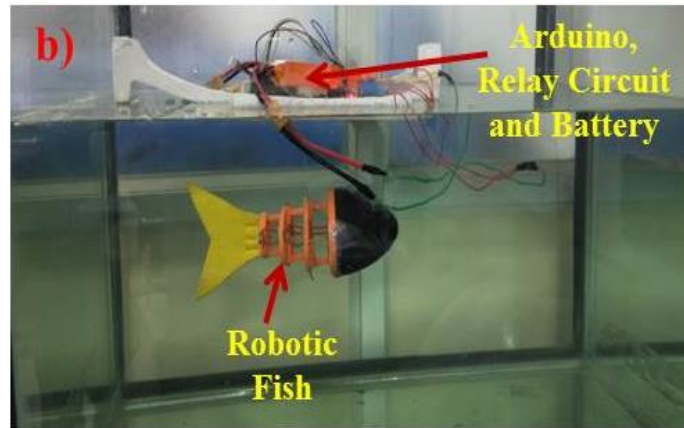
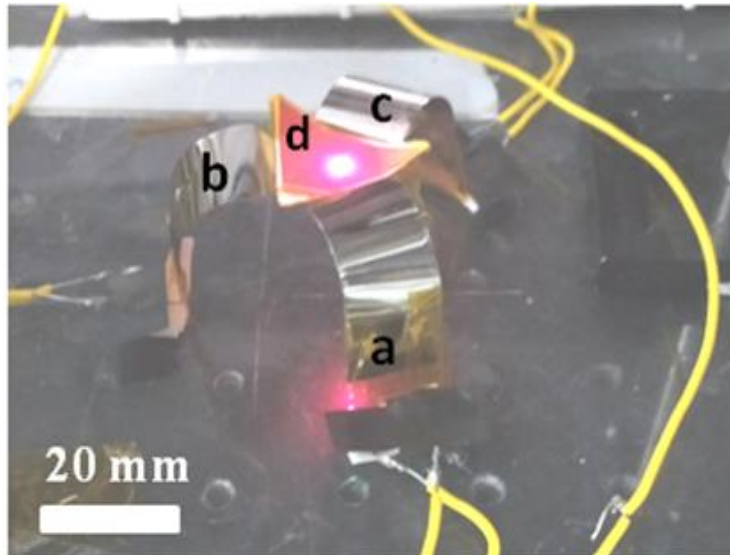


Fig. 8.2: Prototype of SMA spring based robotic fish

8.3 SMA bimorph-based bio-inspired soft robot

- The SMA Bimorph with 75 μm substrate thickness showed a better performance compared to bimorph with lesser substrate thickness.
- A maximum displacement of 9 mm was achieved at 3 V.
- The actuation characteristics with respect to varying load of 30 mg, 45 mg and 60 mg has been performed. A minimum displacement of 0.6 mm at a maximum load of 60 mg has been achieved.
- PID controller has been implemented successfully to control the SMA bimorph for different set points.
- The results confirmed that the SMA Bimorph can be controlled and extended for dedicated robotic applications such as star fish robot.



a) Link 1 b) Link 2 c) Link 3 d) Top plate

Fig. 8.3: Prototype of SMA bimorph based soft robot

8.4 SMA wire based soft robotic gripper

- A maximum surface temperature of 27.59 °C (Input current - 4 A) has been found through simulation and the same has been validated using thermographic camera.
- Through electrical actuation, the developed soft actuator showed a maximum displacement of 7.5 mm at 2 A current.
- The 8 % pre strained SMA wire embedded PDMS actuator showed a maximum displacement of 21 mm.
- The cyclic behavior analysis shows the average displacement of 6 mm has been maintained even after 200 cycles.
- The SMA/PDMS based soft gripper has demonstrated a payload capacity of 7 g



Fig. 8.4: Prototype of SMA wire based soft robotic gripper

8.5 SMA wire based soft robotic jellyfish

- A maximum displacement of 15.3 mm at 0.5 Hz and minimum displacement of 6 mm at 2 Hz has been recorded.
- The maximum temperature of 49.9 °C and a maximum deflection of 42° have been achieved.
- A thrust force of 0.5 N and 0.3 N has been observed in simulation and experiment respectively.
- The robotic jellyfish has moved at a velocity of 10 mm/s and 0.2 mm/s in horizontal and vertical orientation respectively.
- A final jellyfish prototype has been developed with onboard electronics and camera module covered with air tight PDMS structure.

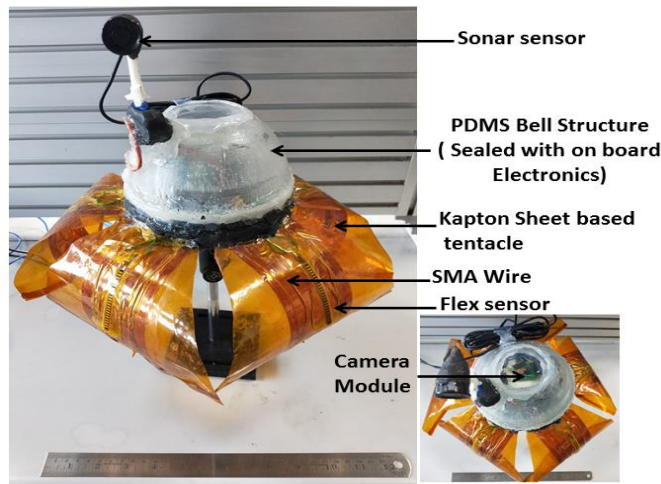


Fig. 8.5: Prototype of SMA wire based soft robotic jellyfish

To extend the lab prototypes into real robotic systems, few important problems have to be addressed. Some of them as follow.

- The power consumption and periodic change requirements of the battery have to be studied.
- The prototype has to be tested in live environments and collect database regarding operation and performance capabilities of the robotic system.
- Robustness and service life of the various components and the robot itself has to be evaluated.
- A detailed reliability analysis need to be done for the developed robots at actual conditions.
- The control studies have to be performed for the developed robots in real time.
- The efficiency of the developed robots can be analyzed in detail
- Autonomous control of Smart material based bio-inspired robots.

References

- [1] Hod Lipson (2014), Challenges and Opportunities for Design, Simulation, and Fabrication of Soft Robots, SOFT ROBOTICS, Volume 1, Number 1
- [2] Carmel Majidi (2014), Soft Robotics: A Perspective—Current Trends and Prospects for the Future, SOFT ROBOTICS, Volume 1, Number 1.
- [3] Stephen Coyle, Carmel Majidi, Philip LeDuc, K. Jimmy Hsia (2018) Bio-inspired soft robotics: Material selection, actuation, and design. *Extreme Mechanics Letters*. 22. 51–59.
- [4] Hugo Rodrigue, Wei Wang, Min-Woo Han, Thomas J.Y. Kim, and Sung-Hoon Ahn (2017), An Overview of Shape Memory Alloy-Coupled Actuators and Robots, SOFT ROBOTICS, Volume 00, Number 00
- [5] D. Ross, M. P. Nemitz, and A. A. Stokes, “Controlling and Simulating Soft Robotic Systems : Insights from a Thermodynamic Perspective,” vol. 3, no. 4, pp. 170–176, 2017.
- [6] M. Runciman, A. Darzi, and G. P. Mylonas, “Soft Robotics in Minimally Invasive Surgery 1,” vol. 00, no. 00, 2019.
- [7] S. Kim, C. Laschi, and B. Trimmer, “Soft robotics : a bioinspired evolution in robotics,” *Trends Biotechnol.*, vol. 31, no. 5, pp. 287–294, 2013.
- [8] T. Arnold and M. Scheutz, “The Tactile Ethics of Soft Robotics : Designing Wisely for Human – Robot Interaction,” vol. 4, no. 2, pp. 81–87, 2017.
- [9] E. J. Park and P. Polygerinos, “The Soft Robotics Toolkit : Shared Resources for Research and Design,” vol. 1, no. 3, pp. 224–230, 2014.
- [10] J. C. Case, E. L. White, and R. K. Kramer, “Soft Material Characterization for Robotic Applications,” vol. 2, no. 2, pp. 80–87, 2015.

- [11] Cheng, N. et al. (2012) Design and analysis of a robust, low-cost, highly articulated manipulator enabled by jamming of granular media. In IEEE International Conference on Robotics and Automation. pp. 4328–4333
- [12] Laschi, C. et al. (2012) A soft robot arm inspired by the octopus. *Adv. Robot.* 26, 709–727
- [13] Lin, H.T. et al. (2011) GoQBot: a caterpillar-inspired soft-bodied rolling robot. *Bioinspir. Biomim.* 6, 026007
- [14] Shepherd, R.F. et al. (2011) Multigait soft robot. *Proc. Natl. Acad. Sci. U.S.A.* 108, 20400–20403
- [15] Thin film shape memory alloys: Fundamentals and device applications. Cambridge university press; 2009.
- [16] Lagoudas DC, editor. Shape memory alloys: modelling and engineering applications. Springer; 2008.
- [17] Mohd Jani J, Leary M, Subic A, Gibson MA. A review of shape memory alloy research, applications and opportunities. *Mater Des* 2014;56:1078–113.
- [18] Barbarino S, Flores EIS, Ajaj RM, Dayyani I, Friswell MI. A review on shape memory alloys with applications to morphing aircraft. *Smart Mater Struct* 2014;23:063001---. doi:10.1088/0964-1726/23/6/063001.
- [19] Sun L, Huang WM, Ding Z, Zhao Y, Wang CC, Purnawali H, et al. Stimulus-responsive shape memory materials: A review. *Mater Des* 2012;33:577–640. doi:10.1016/j.matdes.2011.04.065.
- [20] Yamauchi K, Ohkata I, Tsuchiya K, Miyazaki S. Shape Memory and Superelastic Alloys: Applications and Technologies. Woodland publishing limited; 2011
- [21] FLEXINOL® and Muscle Wires® are Registered Trademarks of DYNALLOY, Inc.
- [22] Hugo Rodrigue, Design and Manufacturing of Twisting Soft Composite Actuators with Shape Memory Alloy Wires, 2015

- [23] Akash, K.; Jain, A.K.; Karmarkar, G.; Jadhav, A.; Narayane , D.C.; Patra, N. & Palani, I.A. Investigations on actuation characteristics and life cycle behaviour of CuAlNiMn shape memory alloy bimorph towards flappers for aerial robots. *Materials and Design.*, 2018, 144, 64–71. <https://doi.org/10.1016/j.matdes.2018.02.013>
- [24] A. Ishida and M. Sato, “Ti – Ni – Cu shape-memory alloy thin film formed on polyimide substrate,” vol. 516, pp. 7836–7839, 2008.
- [25] W. Chu *et al.*, “Review of Biomimetic Underwater Robots Using Smart Actuators,” vol. 13, no. 7, pp. 1281–1292, 2012.
- [26] W. Wang, J. Lee, H. Rodrigue, S. Song, W. Chu, and S. Ahn, “Locomotion of inchworm-inspired robot made of smart soft composite (SSC),” vol. 046006.
- [27] M.S. Kim, W. Chu, J. Lee, Y. Kim, and S. Ahn, “Manufacturing of Inchworm Robot Using Shape Memory Alloy (SMA) Embedded Composite Structure,” vol. 12, no. 3, pp. 565–568, 2011.
- [28] J. Kim, J. Lee, K. Lee, H. Kim, and S. Ahn, “Fabrication of 3D soft morphing structure using shape memory alloy (SMA) wire / polymer skeleton composite †,” vol. 27, no. 10, pp. 3123–3129, 2013.
- [29] S. Seok, C. D. Onal, K. Cho, R. J. Wood, D. Rus, and S. Kim, “Meshworm : A Peristaltic Soft Robot With Antagonistic Nickel Titanium Coil Actuators,” vol. 18, no. 5, pp. 1485–1497, 2013.
- [30] T. Umedachi, V. Vikas, and B. A. Trimmer, “Softworms : the design and control of non-pneumatic , 3D-printed , deformable robots,” *Bioinspir. Biomim.*, vol. 11, no. 2, p. 0.
- [31] A. Villanueva, C. Smith, and S. Priya, “A biomimetic robotic jellyfish (Robojelly) actuated by shape memory alloy composite actuators,” *Bioinspiration and Biomimetics*, 2011.

- [32] Y. Ko, S. Na, Y. Lee, and K. Cha, "A jellyfish-like swimming mini-robot actuated by an electromagnetic actuation system," vol. 057001, 2012.
- [33] S. Yeom, J. Jeon, H. Kim, B. Youn, and I. Oh, "Bio-inspired Jellyfish Robots based on Ionic-type Artificial Muscles," pp. 69–72.
- [34] J. Xiao, J. Duan, and J. Yu, "Design and Implementation of A Novel Biomimetic Robotic Jellyfish," 2013 IEEE Int. Conf. Robot. Biomimetics, no. December, pp. 988–993, 2013.
- [35] X. Li and J. Yu, "Development of a Novel Robotic Jellyfish Based on Mechanical Structure Drive and Barycenter Adjustment," 2015 IEEE Int. Conf. Robot. Biomimetics, pp. 261–266, 2015.
- [36] H. Godaba, J. Li, Y. Wang, and J. Zhu, "A Soft Jellyfish Robot Driven by a Dielectric Elastomer Actuator," IEEE Robot. Autom. Lett., vol. 1, no. 2, pp. 624–631, 2016.
- [37] J. Frame, N. Lopez, O. Curet, and E. D. Engeberg, "Thrust force characterization of free-swimming soft robotic jellyfish," 2018.
- [38] Y. Tadesse, A. Villanueva, C. Haines, D. Novitski, R. Baughman, and S. Priya, "Hydrogen-fuel-powered bell segments of biomimetic jellyfish," vol. 045013, 2012.
- [39] K. J. Cho, E. Hawkes, C. Quinn, and R. J. Wood, "Design, fabrication and analysis of a body-caudal fin propulsion system for a microrobotic fish," in Proceedings - IEEE International Conference on Robotics and Automation, 2008.
- [40] Z. Wang, Y. Wang, J. Li, and G. Hang, "A micro biomimetic manta ray robot fisactuated by SMA," in 2009 IEEE International Conference on Robotics and Biomimetics, ROBIO 2009, 2009.

- [41] A. Ravalli, C. Rossi, and G. Marrazza, "Bio-inspired fish robot based on chemical sensors," *Sensors Actuators, B Chem.*, 2017.
- [42] Z. Wang, G. Hang, J. Li, Y. Wang, and K. Xiao, "A micro-robot fish with embedded SMA wire actuated flexible biomimetic fin," *Sensors Actuators, A Phys.*, 2008.
- [43] S. Guo, T. Fukuda, and K. Asaka, "Fish-like Underwater Microrobot with 3 DOF," 2002.
- [44] S. T. McGovern et al., "Evaluation of thrust force generated for a robotic fish propelled with polypyrrole actuators," *Polym. Int.*, 2010.
- [45] C. Rossi, J. Colorado, W. Coral, and A. Barrientos, "Bending continuous structures with SMAs: a novel robotic fish design," vol. 6, 2011.
- [46] E. Actuators, J. Shintake, V. Cacucciolo, and H. Shea, "Soft Biomimetic Fish Robot Made of Dielectric," vol. 5, no. 4, pp. 466–474, 2018.
- [47] S. Zhang, B. Liu, L. Wang, Q. Yan, K. H. Low, and J. Yang, "Design and implementation of a lightweight bioinspired pectoral fin driven by SMA," *IEEE/ASME Trans. Mechatronics*, 2014.
- [48] Meng, Q. & Hu, J. A review of shape memory polymer composites and blends. *Compos.A: Appl.Sci.Manuf.*, 2009, 40, 1661–1672. <https://doi.org/10.1016/j.compositesa.2009.08.011>.
- [49] Tsoi, K.A.; Stalmans, R.; Schrooten, J.; Wevers, M. & Mai, Y.W. Impact damage behavior of shape memory alloy composites. *Mater. Sci. Eng. A.*, 2003, 342, 207–215. [https://doi.org/10.1016/S0921-5093\(02\)00317-9](https://doi.org/10.1016/S0921-5093(02)00317-9).
- [50] Schrooten, J.; Michaud, V. & Parthenios, J. Progress on composites with embedded shape memory alloy wires. *Mater.*

- Trans., 2002, 43, 961–973.
<https://doi.org/10.2320/matertrans.43.961>
- [51] Zardetto, V.; Brown, T.M.; Reale, A. & Di Carlo, A. Substrates for flexible electronics: a practical investigation on the electrical, film flexibility, optical, temperature, and solvent resistance properties. *J. Polym. Sci. B Polym. Phys.*, 2001, 49, 638–648. <https://doi.org/10.1002/polb.22227>.
- [52] Tsoi, K.A.; Schrooten, J. & Stalmans, R. Part I. Thermomechanical characteristics of shape memory alloys. *Mater. Sci. Eng. A.*, 2004, 368, 286–298. <https://doi.org/10.1016/j.msea.2003.11.006>.
- [53] Saunders, W.R.; Robertshaw, H.H. & Rogers, C.A. Structural acoustic control of a shape memory alloy composite beam. *J. Intell. Mater. Syst. Struct.*, 1991, 2, 508–527. <https://doi.org/10.1177/1045389X9100200406>
- [54] Lester, B.T.; Baxevanis, T.; Chemisky, Y. & Lagoudas, D.C. Review and perspectives: shape memory alloy composite systems. *Acta Mech.*, 2015, 226, 3907–3960. <https://doi.org/10.1007/s00707-015-1433-0>.
- [55] Kamalakannan, G.M.; Giresk Kumar Singh. & Ananda, C.M. A Multi-segment Morphing System for a Micro Air Vehicle using Shape Memory Alloy Actuators. *Defence Science Journal.*, 2020, Vol. 70, No. 1, pp. 3-9. DOI : 10.14429/dsj.70.14145
- [56] Yamauchi K, Ohkata I, Tsuchiya K, Miyazaki S. *ShapeMemory and Superelastic Alloys Technologies and Applications*. Woodhead Publishing, 2011. 232p.
- [57] Dimitris C. Lagoudas. *Shape Memory Alloys: Modeling and Engineering Applications*. Springer US, 2008. 436. <https://doi.org/10.1007/978-0-387-47685-8>.

- [58] Yang, S.; Zhang, F.; Wu, J.; Lu, Y.; Shi, Z.; Wang, C. & Liu, X. Superelasticity and shape memory effect in Cu–Al–Mn–V shape memory alloys. *Mater. Des.*, 2017, 115, 17–25. <https://doi.org/10.1016/j.matdes.2016.11.035>.
- [59] Oliveira, J.P.; Zeng, Z.; Andrei, C.; Braz Fernandes, F.M.; Miranda, R.M.; Ramirez, A.J.; Omori, T. & Zhou, N. Dissimilar laser welding of superelastic NiTi and CuAlMn shape memory alloys. *Mater. Des.*, 2017, 128, 166–175. <https://doi.org/10.1016/j.matdes.2017.05.011>.
- [60] Shariat, B.S.; Meng, Q.; Mahmud, A.S.; Wu, Z.; Bakhtiari, R.; Zhang, J.; Motazedian, F.; Yang, H.; Rio, G.; Nam, T.H. & Liu, Y. Functionally graded shape memory alloys: design, fabrication and experimental evaluation. *Mater. Des.*, 2017, 124, 225–237. <https://doi.org/10.1016/j.matdes.2017.03.069>.
- [61] Kim, M.S.; Chu, W.S.; Lee, J.H.; Kim, Y.M. & Ahn, S.H. Manufacturing of Inchworm Robot Using Shape Memory Alloy (SMA) Embedded Composite Structure. *International Journal of Precision Engineering and Manufacturing.*, 2011, Vol. 12, No. 3, pp. 565-568. <https://doi.org/10.1007/s12541-011-0071-2>
- [62] Liu, T.; Zhou, T.; Yao, Y.; Zhang, F.; Liu, L.; Liu, Y. & Leng, J. Stimulus methods of multifunctional shape memory polymer nanocomposites: a review. *Compos. A: Appl. Sci. Manuf.*, 2017, 100, 20–30. <https://doi.org/10.1016/j.compositesa.2017.04.022>.
- [63] Kim, Y. & Do, D. Shape memory characteristics of highly porous Ti-rich TiNi alloys. *Mater. Lett.*, 2016, 162, 1–4. <https://doi.org/10.1016/j.matlet.2015.09.101>.
- [64] Gugel, H.; Schuermann, A. & Theisen, W. Laser welding of NiTi wires. *Mater. Sci. Eng. A.*, 2008, 481–482, 668–671. <https://doi.org/10.1016/j.msea.2006.11.179>.

- [65] Huang, X. & Liu, Y. Surface morphology of sputtered NiTi-based shape memory alloy thin films. *Surf. Coat. Technol.*, 2005, 190, 400–405. <https://doi.org/10.1016/j.surfcoat.2004.02.029>.
- [66] Gill, J.J.; Chang, D.T.; Momoda, L.A. & Carman, G.P. Manufacturing issues of thin film NiTi micro wrapper. *Sens. Actuators A Phys.*, 2001, 93, 148–156. [https://doi.org/10.1016/S0924-4247\(01\)00646-X](https://doi.org/10.1016/S0924-4247(01)00646-X).
- [67] Shin, D.D.; Lee, D.G.; Mohanchandra, K.P. & Carman, G.P. Thin film NiTi microthermostat array. *Sens. Actuators A Phys.*, 2006, 130–131, 37–41. <https://doi.org/10.1016/j.sna.2005.10.010>
- [68] Sassa, F.; Al-Zain, Y.; Ginoza, T.; Miyazaki, S. & Suzuki, H. Miniaturized shape memory alloy pumps for stepping microfluidic transport. *Sens. Actuators B Chem.*, 2012, 165, 157–163. <https://doi.org/10.1016/j.snb.2011.12.085>
- [69] Shin, D.D.; Mohanchandra, K.P. & Carman, G.P. High frequency actuation of thin film NiTi. *Sens. Actuators A Phys.*, 2004, 111, 166–171. <https://doi.org/10.1016/j.sna.2003.09.026>
- [70] Choudhary, N. & Kaur, D. Shape memory alloy thin films and heterostructures for MEMS applications: a review. *Sens. Actuators A Phys.*, 2016, 242, 162–181. <https://doi.org/10.1016/j.sna.2016.02.026>
- [71] Fu, Y.Q.; Luo, J.K.; Flewitt, A.J.; Huang, W.M.; Zhang, S.; Du, H.J. & Milne, W.I. Thin film shape memory alloys and micro actuators. *Int. J. Computational Materials Science and Surface Engineering.*, 2009, Vol. 2, Nos. 3/4. <https://doi.org/10.1504/IJCMSSE.2009.027483>
- [72] Huang, X.; San Juan, J. & Ramirez, A.G. Evolution of phase transformation behavior and mechanical properties with

- crystallization in NiTi thin films. *Scripta Materialia.*, 2010, 63, 16–19. <https://doi.org/10.1016/j.scriptamat.2010.02.037>
- [73] Kotnur, V.G. & Janssen, G.C.A.M. In situ stress measurements and mechanical properties of a composition range of NiTi thin films deposited at elevated temperature. *Surface & Coatings Technology.*, 2012, 211, 167–171. <https://doi.org/10.1016/j.surfcoat.2011.10.047>
- [74] Sanjabi, S. & Barber, Z.H. The effect of film composition on the structure and mechanical properties of NiTi shape memory thin films. *Surface & Coatings Technology.*, 2010, 204, 1299–1304. <https://doi.org/10.1016/j.surfcoat.2009.10.013>
- [75] Wang, X. & Joost J. Vlassak. Thickness and film stress effects on the martensitic transformation temperature in equi-atomic NiTi thin films. *Mechanics of Materials.*, 2015, 88, 50–60. <https://doi.org/10.1016/j.mechmat.2015.05.001>
- [76] Tillmann, W. & Momeni, S. Tribological performance of near equiatomic and Ti-rich NiTi shape memory alloy thin films. *Acta Materialia.*, 2015, 92, 189–196. <https://doi.org/10.1016/j.actamat.2015.04.006>
- [77] Ishida, A. Ti–Ni–Cu/polyimide composite-film actuator and simulation tool. *Sens. Actuators A Phys.*, 2015, 222, 228–236. doi:10.1016/j.sna.2014.12.012.
- [78] Ishida, A. & Sato, M. Ti-Ni-Cu shape-memory alloy thin film formed 356 on polyimide substrate. *Thin Solid Films.*, 2008, 516, 7836–7839. doi:10.1016/j.tsf.2008.04.091.
- [79] Ishida, A. & Sato, M. Development of Polyimide/SMA Thin-Film Actuator. *Mater. Sci. Forum.*, 2010, 654–656, 2075–2078. doi:10.4028/www.scientific.net/MSF.654-656.2075.
- [80] Ishida, A. & Martynov, V. Sputter-Deposited Alloy Thin Films: Properties and Applications. *MRS Bull.*, 2002, vol. 27, issue. 2, 111–114. <https://doi.org/10.1557/mrs2002.46>

- [81] Kotnur, V.G.; Tichelaar, F.D.; Fu, W.T.; De Hosson, J.T.M. & Janssen, G.C.A.M. Shape memory NiTi thin films deposited at low temperature. *Surf. Coatings Technol.*, 2014, 258, 1145–1151. doi:10.1016/S0921-5093(99)00403-7.
- [82] Kotnur, V.G.; Tichelaar, F.D. & Janssen, G.C.A.M. Sputter deposited Ni-Ti thin films on polyimide substrate, *Surf. Coatings Technol.*, 2013, 222, 44–47. doi:10.1016/j.surfcoat.2013.01.058.
- [83] Akash, K.; Jain, A.K.; Karmarkar, G.; Jadhav, A.; Narayane, D.C.; Patra, N. & Palani, I.A. Investigations on actuation characteristics and life cycle behaviour of CuAlNiMn shape memory alloy bimorph towards flappers for aerial robots. *Materials and Design.*, 2018, 144, 64–71. <https://doi.org/10.1016/j.matdes.2018.02.013>
- [84] Akash, K.; Mani Prabu, S.S.; Shukla, A.K.; Nath, T.; Karthick, S. & Palani, I.A. Investigations on the life cycle behavior of Cu-Al-Ni/polyimide shape memory alloy bi-morph at varying substrate thickness and actuation conditions. *Sensors and Actuators A.*, 2017, 254, 28–35. <https://doi.org/10.1016/j.sna.2016.12.008>
- [85] Akash, K.; Shukla, A.K.; Mani Prabu, S.S.; Narayane, D.C.; Kanmanisubbu, S. & Palani, I.A. Parametric investigations to enhance the thermomechanical properties of CuAlNi shape memory alloy Bi-morph. *Journal of Alloys and Compounds.*, 2017, 720, 264-271. <https://doi.org/10.1016/j.jallcom.2017.05.255>
- [86] Akash, K.; Mani Prabu, S.S.; Gustmann, T.; Jayachandran, S.; Pauly, S. & Palani, I.A. Enhancing the Life Cycle Behaviour of Cu-Al-Ni Shape Memory Alloy bimorph by Mn Addition. *Materials Letters.*, 2018, 226, 55-58. <https://doi.org/10.1016/j.matlet.2018.05.008>.
- [87] Jayachandran, S.; Akash, K.; Mani Prabu, S.S.; Manikandan, M.; Muralidharan, M.; Brolin, A. & Palani, I.A. Investigations on performance viability of NiTi, NiTiCu, CuAlNi

- and CuAlNiMn shape memory alloy/Kapton composite thin film for actuator application. *Composites Part B: Engineering.*, 2019, 176, 107182. <https://doi.org/10.1016/j.compositesb.2019.107182>
- [88] Jayachandran, S.; Mani Prabu, S.S.; Manikandan, M.; Muralidharan, M.; Harivishanth, M.; Akash, K. & Palani, I.A. Exploring the functional capabilities of NiTi shape memory alloy thin films deposited using electron beam evaporation technique. *Vacuum.*, 2019, 168, 108826. <https://doi.org/10.1016/j.vacuum.2019.108826>
- [89] A. Abuzaiter, M. Nafea, M. Sultan, and M. Ali, “Mechatronics Development of a shape-memory-alloy micromanipulator based on integrated bimorph microactuators,” *Mechatronics*, vol. 38, pp. 16–28, 2016.
- [90] Huang WM, Gao XY, Loo BK, He LM, Ngoi BKA. Micro-gripper using two-way NiTi shape-memory alloy thin sheet. *Shape memory materials and its applications*, vol. 394–3; 2002. 87–90.
- [91] Zhenlong Wang, Guanrong Hang, Jian Li, Yangwei Wang, Kai Xiao (2008), A micro-robot fish with embedded SMA wire actuated flexible biomimetic fin, *Sensors and Actuators A: Physical*, 144, 354–360 <https://doi.org/10.1016/j.sna.2008.02.013>
- [92] Tao Tao , Yuan Chang Liang, Minoru Taya (2006), Bio-inspired Actuating System for Swimming Using Shape Memory Alloy Composites, *International Journal of Automation and Computing*, 4, 366-373.
- [93] Ziegler, J.G. & Nichols, N.B. Optimum settings for automatic controllers, *Transactions of the ASME*, 1942, 64, 759-768.
- [94] W. Huang, “On the selection of shape memory alloys for actuators,” *Mater. Des.*, 2002, vol. 23, no. 1, pp. 11–19.
- [95] K. Otsuka and C. M. Wayman, “Shape Memory Materials,” Cambridge University Press, 1999, vol. 16, no. 1. pp. 1–162.

- [96] T. W. Duerig and A. R. Pelton, "Ti-Ni Shape Memory Alloys," *Mater. Prop. Handb. Titan. Alloy.*, pp. 1–14.
- [97] Hugo Rodrigue, Wei Wang, Binayak Bhandari, Min-Woo Han, Sung-Hoon Ahn, SMA-based smart soft composite structure capable of multiple modes of actuation, *Composites Part B: Engineering*, Volume 82, 1 December 2015, Pages 152-158